Doctoral Dissertation
Doctoral Program in Bioengineering and Surgical-Medical Sciences (33^{rd} cycle)

Wall Shear Stress Topological Skeleton Analysis in Cardiovascular Flows: Methods and Applications

Valentina Mazzi

* * * * *

Supervisors
Prof. Umberto Morbiducci, Supervisor
Prof. Diego Gallo, Co-supervisor

Doctoral Examination Committee:
Prof. Alessandro Veneziani, Referee, Emory University, Atlanta, USA
Prof. Salvatore Pasta, Referee, University of Palermo, Italy

Politecnico di Torino
May, 2021

I hereby declare that, the contents and organisation of this dissertation constitute my own original work and does not compromise in any way the rights of third parties, including those relating to the security of personal data.

.....

Valentina Mazzi

Turin, May, 2021

Summary

Vascular pathologies are abnormal conditions of the blood vessel and represent the dominant component of cardiovascular diseases, the leading cause of death globally. The pathogenesis of vascular diseases is modulated by a complex interplay between several systemic risk and local factors. Among them, it has long been recognized that hemodynamic factors regulate several aspects of vascular pathophysiology, leading the thorough understanding of hemodynamics in human vessels to be of great interest. In this context, the Wall Shear Stress (WSS), the frictional force exerted by the streaming blood flow on the vascular luminal surface, has been recognized as a major hemodynamic factor involved in vascular homeostasis. Due to this, peculiar WSS phenotypes have been identified over the years as potential indicators of flow disturbances, associated with aggravating biological events.

Despite the growing research interest in studying hemodynamics, the mechanistic link between WSS and vascular disease is still not completely clarified. Improving the current understanding of the association between local altered hemodynamics and clinical observations is one of the important challenges in hemodynamics research. Recent studies suggest that the WSS vector field topological skeleton of cardiovascular flows could be a promising tool for this challenging task. Based on dynamical system theory, the WSS topological skeleton is composed by a collection of fixed points, focal points where WSS locally vanishes, and unstable/stable manifolds, consisting in contraction/expansion regions linking fixed points. The interest in WSS topological skeleton analysis is supported by circumstantial evidence about the capability of WSS topological features to reflect cardiovascular complexity, with direct links to flow features like flow stagnation, separation and recirculation, which are known to be associated with adverse vascular biological events. Besides, WSS topological skeleton features affect biotransport processes, with important implications in many cardiovascular processes, including the initiation of atherosclerosis, and thrombogenesis.

Lagrangian-based techniques have been recently proposed to analyse WSS topological skeleton in cardiovascular flows. Although Lagrangian approaches are typically preferred to detect time-dependent topological structures in complex flows, their application might have some practical limitations, such as the high computational effort and the poor control over the flow region of interest. Stimulated from this scenario, the main objective of this work is to propose a fast and simple Eulerian-based method for identifying the topological skeleton of the WSS vector field in complex vascular geometries. We introduce a novel application of the Volume Contraction theory in cardiovascular flows, demonstrating that the divergence of the WSS gives practical information about the associated dynamical system. The presented methodology aims at speeding up studies on the physiological significance of WSS topological skeleton features in cardiovascular flows to investigate on the still-poorly-explored mechanisms by which such peculiar WSS features influence vascular biology.

The second objective of this work concerns the exploration of the possible involvement of WSS topological skeleton features in processes leading to vascular dysfunction and the identification of direct links between WSS topological skeleton and markers of vascular disease from real-world clinical longitudinal data. To do that, we apply the proposed Eulerian approach on personalized computational hemodynamics models of human aorta, intracranial aneurysm, carotid bifurcations, ascending thoracic aortic aneurysm, stented coronary arteries, and pig-specific computational hemodynamics model of coronary arteries. Furthermore, clinical follow-up data of carotid intima-media thickness, personalized *in vivo* estimates of the local aortic stiffness and pig follow-up data of coronary artery wall thickness are used as markers of vascular disease from real-world data aiming at relating WSS features to vascular remodelling.

The presented Eulerian-based method for WSS topological skeleton analysis and the findings related to its application to cardiovascular flows might help in clarifying the role played by local hemodynamics in vascular pathophysiology.

Acknowledgements

First and foremost, I wish to thank Professor Umberto Morbiducci for giving me the opportunity to do this work, for his efforts in encouraging my work, for his patience, motivation, and knowledge.

I am thankful to Professor Diego Gallo and Dr. Claudio Chiastra for their invaluable advice, suggestions and ideas provided during these three years.

I am also grateful to Professor David Steinman for giving me the opportunity to spend five months at the University of Toronto in his research group at Biomedical Simulation Laboratory.

I wish to express my sincere thanks to my colleagues (and friends) in the Solid & Fluid Biomechanics Group at Politecnico di Torino for the stimulating discussions, for their continuous support, for a cherished time spent together, and in social settings.

Thanks to my friends for providing me unfailing support.

I heartily wish to thank Gianpaolo, for his profound belief in my abilities.

Finally, thanks to my parents and to my brother for the encouragement and support all through my studies.

Alla mia famiglia

Il matematico gioca un gioco in cui egli stesso inventa le regole. Il fisico gioca un gioco in cui le regole sono fornite dalla Natura. Ma, con il passare del tempo, diventa sempre più evidente che le regole che il matematico trova interessanti sono quelle che la Natura ha scelto.

Paul Adrien Maurice Dirac (1902-1984)

Contents

List of Tables

List of Figures

Chapter 1

Introduction

1.1 Clinical Motivations

The cardiovascular system is a closed, internal flow loop with branches where the blood circulates. The normal blood flow inside arteries is mainly laminar, with secondary flows generated in correspondence of branches and curves. The responses of arteries to local altered hemodynamic conditions can cause an abnormal biological response, leading to pathological disease. Systemic and local factors are responsible for modulating the pathogenesis of the disease, among them, it is well recognized that local hemodynamics plays an important key role in the development, diagnosis and treatment of vascular disease, leading the thorough understanding of hemodynamics in human vessels to be of great interest.

Recent advances in medical imaging, modelling, and Computational Fluid Dynamics (CFD) has allowed to model local blood flow patterns in realistic, personalized cardiovascular models aiming at (1) improving the current understanding of the role played by the local hemodynamics in vascular pathophysiology, and in a wider perspective (2) demonstrating how some clinical information can be derived from computational simulations. In this regard, the coupling of medical imaging and CFD is employed in this work to obtain highly resolved in space and in time 4D blood flow patterns in personalized cardiovascular models. The objectives of this work concern the exploration of peculiar near-wall flow features in healthy and disease cardiovascular districts. In the near-wall region, blood flow interacts directly with the vessel wall and imparts mechanical shear stress on the endothelium, which in turn regulates important developmental, homeostatic and adaptive mechanisms

in arteries [1].Markers of vascular disease from real-world clinical longitudinal data are used in this work aiming at improving the current understanding of the link between disturbed flows and clinical observations. The underlying clinical motivation is to provide specific hemodynamic descriptors that could be adopted as biomarkers of vascular disease for diagnostic and prognostic purposes within a clinical context.

1.2 Anatomy and Pathologies of cardiovascular districts

1.2.1 Blood and Vessels

Blood is a fluid tissue that transports nutrients, oxygen and metabolic wastes. The main blood components are: plasma, Red Blood Cells (RBCs), White Blood Cells (WBCs) or leukocytes and platelets. The plasma is a complex solution, composed by water, proteins, salts, hormones and lipids, in which RBCs, WBCs, and platelets are suspended and it performs several functions, such as regulating the body water and salts, irrigating tissues, providing a protection against infections and coagulating blood. RBs are small, flexible and oval biconcave disks without nucleus that carry oxygen throughout the body. WBCs are involved in protecting the body against infections. Platelets are cells without nucleus smaller than RBs and WBCs that play a role in blood coagulation, by initiating blood clots formation. Blood flows through the vessels, which are biologically active organs maintaining their own integrity and homeostasis through mechanisms regulated within the vessel wall. The structure of an arterial blood vessel is composed of three layers. The tunica adventitia is the outer layer, mainly composed of collagen that anchors the vessel to nearby organs. The tunica media is the middle layer, composed of elastic tissue and smooth muscle cells. The tunica intima is the inner layer, composed of a monolayer of the Endothelial Cells (ECs), known as endothelium, which provides a barrier to keep plasma and blood cells in the lumen. ECs are directly in contact with the blood flow, acting as a lining inside the arteries. The ECs, sitting at the interface between vessel and flowing blood, regulate exchanges between the blood flow and the surrounding tissues and are the biosensors of biochemical and fluid dynamic stimuli induced by flowing blood flow.

The cardiovascular districts considered in this thesis are the carotid artery bifurcation, the thoracic aorta and the coronary artery (Figure 1.1).

The carotid artery bifurcations are located along the right and left sides of the neck and they bring oxygenated blood from the heart to each side of the head (Figure 1.1A). The right and left Common Carotid Arteries (CCA) originate in the neck from the brachiocephalic trunk and in the aortic arch in the thorax, respectively, and follow symmetrical courses. At the level of the third or fourth cervical vertebra, the CCA bifurcates into an Internal Carotid Artery (ICA), which supplies the brain, and an External Carotid Artery (ECA), which supplies the face and neck. The carotid sinus is a dilated area at the base of the ICA and the artery wall in the sinus region would experience flow disturbance in the near-wall velocity. It is known from clinical practice that the region of the carotid artery bifurcation more sensitive to the arteriosclerotic plaques onset and progression is the carotid sinus in the ICA.

The aorta is the largest blood vessel in the body and it delivers the oxygenated blood to the whole body through systemic circulation (Figure 1.1B). The aorta can be divided into four sections: the ascending aorta, the aortic arch, the thoracic descending aorta and the abdominal aorta. The ascending aorta arises from the left ventricle, it travels with the pulmonary trunk in the pericardial sheath and it passes obliquely upward, forward, and to the right, in the direction of the heart's axis, describing a soft curve in its course. The only branches of the ascending aorta are the two coronary arteries which supply the heart. The aortic arch links the ascending aorta with the descending aorta and there are three branches arising from it: the Brachiocephalic Artery (BCA), which divides into the right common carotid and right subclavian arteries, the Left Common Carotid Artery (LCCA) and the Left Subclavian Artery (LSA). These three branches are responsible to supply with oxygenated blood head, neck and arms. The thoracic descending aorta is located in the thorax. It begins at the level of the fourth thoracic vertebra and it ends in front of the lower border of the twelfth thoracic vertebra, in the diaphragm. The abdominal aorta is a continuation of the thoracic descending aorta, it travels down the posterior wall of the abdomen, anterior to the vertebral column and terminates by bifurcating into the right and left common iliac arteries that supply the lower body.

The coronary arteries are the arterial vessels responsible for transporting oxygenated blood to the heart muscle, wrapping the entire heart (Figure 1.1C). The

coronary arteries are composed of the left main coronary artery and Right Coronary Artery (RCA). The left main coronary divides into two branches: Left Anterior Descending Artery (LAD) and Left Circumflex Artery (LCX). The LAD passes behind the pulmonary artery and reaches the anterior interventricular sulcus, supplying the anterolateral myocardium, apex, and interventricular septum. The LCX follows the left part of the coronary sulcus and reaches nearly as far as the posterior longitudinal sulcus, supplying the posterolateral left ventricle and the anterolateral papillary muscle. The RCA passes through the right coronary sulcus, towards the crux of the heart, supplying oxygenated blood to the right atrium, the right ventricle, and the posterior third and inferior end of the interventricular septum.

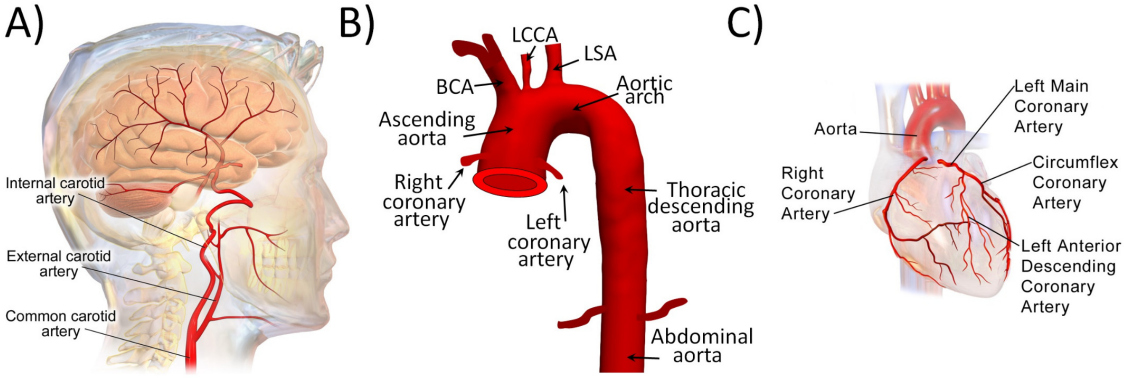

Figure 1.1: A) Schematic of the carotid artery bifurcation. B) Schematic of aorta. BCA=Brachiocephalic Artery; LCCA= Left Common Carotid Artery; LSA=Left Subclavian Artery. C) Schematic of coronary arteries

1.2.2 Vascular Pathology

Atherosclerosis is a chronic inflammatory disease of the arterial system characterized by a progressive lipid accumulation (i.e., atherosclerotic plaques) in the intima layer of the arterial walls. The atherosclerotic plaques cause stenosis, i.e., abnormal narrowing in a blood vessel, and their rupture can occlude an artery downstream to the plaque causing, e.g., myocardial infarction or stroke.
Hyperlipidemic states, diabetes mellitus, cigarette smoking, hypertension and obesity are some of the well-identified risk factors involved in the pathogenesis of atherosclerosis. The exact mechanisms involved in the onset and progression of atherosclerosis are still not completely understood. It is established that atherosclerosis begins with damage to the inner lining of the artery, i.e., the endothelium [2],

leading WBCs to gather at the site of injury. ECs product adhesion molecules, leading monocytes, i.e., the largest type of WBCs playing a fundamental role in the inflammatory process, to roll, adhere and traverse the endothelium. After that, the monocytes become engorged with oxidized lipids and form foam cells, causing an inflammatory immune response that provokes further arterial wall damage. Toxic Low-Density Lipoprotein (LDL) cholesterol molecules can then penetrate into the wall and they become oxidized, because of the presence of free radicals, produced as a product of the immune response. Oxidized LDL aggravate the injury by releasing toxins into the wall. This results in recruiting more WBCs, which in turn further harm the arterial wall, causing more LDL to penetrate the wall. LDL molecules, toxins and WBCs form a lipid foam, the building block of atherosclerotic plaques deposits. This process is considered to be the first step of atherosclerotic plaques formation, and afterward, the disease slowly progresses.

Cerebral Aneurysm is the second vascular pathology considered in this thesis. A cerebral aneurysm is an abnormal dilatation of an artery in the brain, formed when the artery wall becomes thin and weakens. The cerebral aneurysm can (1) exert excessive pressure on the nerves or brain tissue, (2) burst or rupture, causing hemorrhage by spilling blood into the surrounding tissue. The rupture of an aneurysm in the brain can cause serious health problems, such as hemorrhagic stroke, brain damage, coma, and even death. The main risk factors that contribute to aneurysm formation are: hypertension, cigarette smoking, genetic predisposition, infection, and injury or trauma to blood vessels. Although the exact pathogenesis of cerebral aneurysms development and growth is still not completely understood, extracellular matrix defects and degeneration, hemodynamic forces, and inflammatory responses have been suggested playing a key role in process leading to structural fragility in the arterial wall.

The Ascending Thoracic Aortic Aneurysm (ATAA) is another vascular pathology considered in this thesis. The ATAA is a chronic degenerative pathology consisting of an unphysiological localized dilatation of the aorta at the ascending segment. Typically, the ATAA grows in a silent manner and most of them remain undetected unless incidentally discovered. The main catastrophic risks for patients with an ATAA are dissections and improvised rupture. Ascending thoracic aortic dissection occurs when the inner layer of the aorta becomes compromised and treats. This results in a new layer formed between the intima and the media, filled with blood. Ascending aortic dissection represents a surgical emergency, because

if the false lumen ruptures through the outside aortic wall, aortic dissection could be fatal. Rupture of an ATAA occurs because of a weakness of the wall inside the pericardial sac or in the thoracic cavity, producing intense chest pain, hypotension, shock, and sudden death. As opposed to other aortic aneurysms that are associated with atherosclerotic plaques formation, ATAA is mostly associated with connective tissue diseases, e.g., Marfan syndrome, and cystic medial degeneration. The latter process affects the middle layer of the aorta by varying degrees of elastic fibre fragmentation. Consequently, the aortic wall loses its normal strength and elasticity.

1.3 Hemodynamic factors in vascular disease

In studying cardiovascular flows, it is well established that the vessel geometry, the mechanical property of the wall of the vessel, pressure gradients, and blood properties contribute to dictate the blood flow dynamics within the vessel. It is widely documented in the literature that flow features like flow stagnation, separation, reattachment, recirculation, stasis, jet-like flow and turbulence represent flow features linked to aggravating biological events relevant in the context of vascular pathophysiology [3]. Blood flow characterized by such flow features is often referred to as "disturbed" flow, describing a near-wall flow changing direction substantially during the cardiac cycle and commonly exposing the wall to relatively low friction forces induced by the blood. Contrarily, the expression "undisturbed" flow is used to described unidirectional and minimally reversing blood flow.

1.3.1 Effect of shear stress on endothelial cells

The velocity of the blood flow in the vessels decreases from the centre to the wall, generating a shearing effect between adjacent layers of the flowing fluid and between the fluid and the vessel wall. The tangential force per unit area exerted by the flowing fluid on the endothelial cells lining the intimal surface of the vessel is referred to as the Wall Shear Stress (WSS). The magnitude of WSS depends on how fast the blood velocity increases when moving from the vessel wall toward the centre of the vessel.
It is well established that WSS plays an essential role in maintaining the normal functionality of vascular system, since arteries tend to adapt to long-term WSS

variations. Arteries attempt to re-establish a physiological level of WSS by remodelling to a larger/smaller diameter in the presence of increased/decreased WSS, respectively [4].
When ECs are subjected to WSS action, their activities, functions and phenotype could be altered [5]. The response of ECs to the action of WSS differs according to the magnitude, directionality and temporal variation of WSS. In particular, WSS action can change the morphology and orientation of the endothelial cell layer. *In vivo* [6] and *in vitro* [7] studies have demonstrated that ECs exposed to a laminar flow with high WSS values tend to elongate and align in the direction of flow and high uniform shear stress exerts protective effects. By contrast, in areas characterized by disturbed flow, ECs remain more rounded without a clear orientation, with a lack of organization of the cytoskeleton and intercellular junctional proteins [8] and low and/or oscillatory WSS promotes inflammatory activation and apoptosis of ECs. Besides, WSS plays a fundamental role in proliferation and migration processes of ECs. Evidence suggests that high and unidirectional WSS increases EC migration [9] and low and/or oscillatory WSS causes cell loss and migration of ECs away from areas with large WSS gradients [10]. Furthermore, the shear stress forces exerted by the streaming blood flow on ECs affect the permeability of endothelium, thus facilitating the transport of biochemicals into the subendothelial layer [11].

1.3.2 Hemodynamic wall parameters

Over the years, an arsenal of WSS-based descriptors of the near-wall hemodynamics has been proposed as potential indicators of flow disturbances associated with aggravating biological events. Hemodynamic wall parameters take into account WSS magnitude and direction, spatial and temporal WSS gradient e variation of WSS vector with respect to its cycle-average o nominal direction. Among all proposed WSS-based descriptors, the most widely employed parameters are reported:

- Time Average WSS (TAWSS):

$$\text{TAWSS} = \frac{1}{T}\int_0^T |\boldsymbol{\tau}| dt, \tag{1.1}$$

  where $\boldsymbol{\tau}$ is the WSS vector field and T the cardiac cycle duration. Low

values of TAWSS are associated with intima-media complex thickening and stimulate a proatherogenic endothelial phenotype [1], physiological values of TAWSS appear to induce endothelial quiescence, and high TAWSS values lead to endothelial trauma.

- Oscillatory Shear Index (OSI):

$$\mathrm{OSI} = 0.5\left(1 - \frac{|\int_0^T \boldsymbol{\tau} dt|}{\int_0^T |\boldsymbol{\tau}| dt}\right). \tag{1.2}$$

OSI identifies regions on the luminal surface of an artery characterized by highly oscillating WSS along the cardiac cycle. According to eq. (1.2), OSI ranges from 0, i.e., when instantaneous WSS is collinear with cycle-average WSS vector along the cardiac cycle, to 0.5, i.e., when the instantaneous WSS vector deviates from the main flow direction in a large fraction of cardiac cycle. Regions on the luminal surface of an artery exposed by low values of OSI are characterized by minimal flow disruption, whereas regions exposed by high values of OSI are associated with bifurcating flows, vortex formation and local flow reversal, known to be promoting factors for vascular diseases [12]. However, it has been demonstrated using histological data that only the simultaneously presence of low and oscillating WSS, usually correlated with vortexes formation [13, 14]. In addition, Himburg et al. [15] stated that it seems unlikely that endothelial cells sense OSI per se, suggesting that OSI descriptors might be better used in combination with other WSS-based descriptors, rather than as a stand-alone index of the disturbed flow.

- Relative Residence Time (RRT):

$$\mathrm{RRT} = \frac{1}{\mathrm{TAWSS}(1 - 2\mathrm{OSI})} = \frac{T}{|\int_0^T \boldsymbol{\tau} dt|}. \tag{1.3}$$

RRT descriptor is a combination of TAWSS and OSI parameters, inversely proportional to the magnitude of the cycle-average WSS vector field.

Additionally, we report an emerging descriptor of multidirectional shear:

- Transversal WSS (transWSS):

$$\mathrm{transWSS} = \frac{1}{T}\int_0^T |\boldsymbol{\tau} \cdot (\boldsymbol{n} \times \frac{\int_0^T \boldsymbol{\tau} dt}{|\int_0^T \boldsymbol{\tau} dt|})| dt, \tag{1.4}$$

where $\boldsymbol{n}$ is the unit vector normal to the arterial surface. TransWSS is a recent descriptor of WSS multidirectionality, defined as the average WSS component acting orthogonal to the cycle-averaged WSS vector direction [16].

The WSS-based descriptors are summarized in Table 1.1.

Table 1.1: Definition of WSS-based hemodynamic descriptors of "disturbed flow".

WSS-based hemodynamic descriptors	
Time Average WSS (TAWSS)	$\text{TAWSS}=\frac{1}{T}\int_0^T \lvert\boldsymbol{\tau}\rvert dt$
Oscillatory Shear Index (OSI)	$\text{OSI}=0.5(1-\frac{\lvert\int_0^T \boldsymbol{\tau} dt\rvert}{\int_0^T \lvert\boldsymbol{\tau}\rvert dt})$
Relative Residence Time (RRT)	$\text{RRT}=\frac{1}{\text{TAWSS}(1-2\text{OSI})}=\frac{T}{\lvert\int_0^T \boldsymbol{\tau} dt\rvert}$
Transversal WSS (transWSS)	$\text{transWSS}=\frac{1}{T}\int_0^T \lvert\boldsymbol{\tau}\cdot(\boldsymbol{n}\times\frac{\int_0^T \boldsymbol{\tau} dt}{\lvert\int_0^T \boldsymbol{\tau} dt\rvert})\rvert dt$

1.3.3 Wall shear stress topological skeleton

It has been recently highlighted that the complex hemodynamic milieu endothelial cells are exposed to can by only partially described by low and oscillatory WSS paradigm [17, 18], as confirmed by a large body of literature reporting from poor-to-moderate associations between low and oscillatory WSS and vascular disease [17, 18, 19]. These evidence suggest that an in-depth analysis aiming at closing the gap of knowledge currently limiting the use of WSS-based descriptors as biomarkers for diagnostic and prognostic purposes is needed [20]. In order to improve the current understanding of the link between local altered hemodynamics and clinical outcomes, the topological skeleton of WSS vector field at the luminal surface of a vessel is receiving increasing interest [21, 22, 23]. Briefly, the WSS topological skeleton is composed of a collection of fixed points and unstable/stable manifolds that connect them. A fixed point is a focal point where the vector locally vanishes and unstable/stable manifolds identify contraction/expansion regions linking the fixed points. The link between WSS topological skeleton features and vascular cell biology lies in (1) their ability to quantify the complex and highly dynamic features of the WSS field, (2) their strong link with flow features like flow stagnation, separation, and recirculation, known to be promoting factors for vascular disease. In addition, it has been recently demonstrated that WSS topological skeleton governs

the near-wall biochemical transport in arteries [23, 22, 24, 25], a process linked to e.g., endothelium-mediated vasoregulation, thrombosis, and atherosclerosis [26].

State of the Art

In studying hemodynamics, several studies have analysed the WSS fixed points in the context of cardiovascular flows. Fixed points were considered in idealized computational hemodynamic models of coronary bypass grafts to study flow separation [27], in personalized computational models of cerebral aneurysm [28, 29, 30, 31], and to study the impact of cerebral aneurysm coiling [32]. WSS fixed points were also identified in computational hemodynamic models of aortic coarctation [33]. A co-localization between WSS fixed points and wall thinning in cerebral aneurysm domes was reported [34, 35]. Moreover, Ge and Sotiropulos [36] hypothesized a link between WSS fixed points observed on the aortic side of the aortic valve leaflet and the focal distribution of calcification lesions in the valve. Interestingly, previous investigations have demonstrated how focal pathological vascular responses might be triggered by WSS fixed points[21].

Concerning WSS manifolds analysis in the context of cardiovascular flows, it has been demonstrated that WSS manifolds are linked to near-wall mass transport [23, 22, 21], with implications in atherosclerosis initiation and in general in vascular dysfunction [11]. As will be extensively clarified in the following, previous studies addressing the WSS manifolds in the context of cardiovascular flows are mostly based on Lagrangian approaches [37, 22, 23, 21, 25]. In general, Lagrangian-based approaches start from the processing of Eulerian data, which represent the typical output of current *in vivo* (e.g., Phase-Contrast Magnetic Resonance Imaging (PC MRI)), *in vitro* (e.g., particle image velocimetry), and computational methods used for the investigation of cardiovascular flows. Lagrangian approaches are effective and useful to reveal the global organization of time-dependent vector field and characterize its evolution along time, making the relevant features easy to detect by visual inspection as they offer effective three-dimensional (or even four-dimensional, i.e., including time) visualizations. On the other hand, Lagrangian-based approaches might face some practical limitations. In particular, Lagrangian

techniques are based on integrated particle trajectory information, requiring sufficiently resolved data in both time and space, thus making such methods computationally expensive and time-consuming in principle [38]. Moreover, adopting a Lagrangian approach may result in a poor control over the zone of investigation, which is determined by particle motion and accumulation. For this reason, it can also be difficult to get a complete picture of the flow at specific time instants. Furthermore, the influence of particle distributions and of particle seeding schemes on quantities of interest is poorly investigated.

1.4 Aim of the study

Stimulated from (1) the recent interest on the role of the WSS topological skeleton in vascular dysfunction, and (2) the consideration that Eulerian-based approaches usually simplify the data analysis workflow and are characterized by a reduced computational cost, the aims of the present thesis can be summarized as follows:

- to propose a Eulerian-based method for identifying the topological skeleton of the WSS on the luminal surface of 3D vessels, aiming at simplifying and at speeding up studies on the physiological significance of WSS topological skeleton in cardiovascular flows;
- to test the robustness of the proposed Eulerian-based method and to verify its ability to correctly identify WSS topological features;
- to identify direct associations between WSS topological skeleton and markers of vascular disease from real-world clinical longitudinal data, aiming at investigating on the still-poorly-explored mechanisms by which WSS topological skeleton features influence vascular pathophysiology.

This thesis is structured as follows:

Chapter 2: Theoretical concepts

In this chapter, a theoretical background is reported for a better understanding of the mathematical theory supporting the proposed method. Moreover, an overview of the Lagrangian-based methods for WSS topological skeleton analysis currently adopted in the literature is presented and discussed.

Chapter 3: Eulerian-based Method for Wall Shear Stress Topological Skeleton Identification

In this chapter, the steps of the proposed Eulerian-based method to identify WSS topological skeleton on the luminal surface of an artery are described and detailed.

Chapter 4: Benchmarking

This chapter focuses on verifying the ability of the proposed Eulerian-based approach to correctly identify WSS topological features, by considering an analytical two-dimensional vector field and the WSS vector field defined on the luminal surface of a three-dimensional complex geometry.

Chapter 5: Wall Shear Stress Divergence as a Template of Near-Wall Mass Transport in Aortic Flow

Personalized computational hemodynamics is a promising tool to clarify and predict the association between low density lipoproteins (LDL) transport in aorta, disturbed shear stress and atherogenesis. However, properly modelling mass transfer to the wall requires the use of high-resolution grids, which increase the computational costs associated to this approach. Recent studies have demonstrated that Lagrangian Wall Shear Stress (WSS) structures are able to provide a template for near-wall transport. In this chapter, the proposed Eulerian-based method is applied to compute WSS topological skeleton in a patient-specific computational model of human aorta, and its ability to properly describe LDL wall transfer is tested.

Chapter 6: Analysis of the Unsteady Nature of Wall Shear Stress Topological Skeleton Features

In this chapter, the proposed method is applied to personalized computational hemodynamics models of one carotid bifurcation and one intracranial aneurysm aiming at providing an in-depth analysis of the time dependence of the WSS topological skeleton along the cardiac cycle, enriching the information obtained from cycle-average WSS.

Chapter 7: Wall Shear Stress Topological Skeleton Predicts long-term Restenosis Risk after Surgery in the Carotid Bifurcation

The aim of this chapter is to identify direct associations between WSS topological skeleton features and markers of vascular disease from real-world clinical longitudinal data of long-term restenosis after carotid endarterectomy (CEA), a process deemed to present similarities with primary atherosclerotic lesion formation. To do that, the Eulerian-based analysis of the topological skeleton of the WSS vector field was carried out on personalized computational hemodynamics models of a cohort of 12 asymptomatic patients who underwent 13 CEA interventions (i.e., one patient with bilateral CEA), and its ability in predicting post-intervention restenosis was explored using clinical follow-up data of intima-media thickness (IMT) at 60 months after CEA.

Chapter 8: Deciphering Ascending Thoracic Aortic Aneurysm Hemodynamics in Relation to Biomechanical Properties

The degeneration of the arterial wall at the basis of the Ascending Thoracic Aortic Aneurysm (ATAA) is a complex multifactorial process, which may lead to clinical complications and, ultimately, death. In this chapter, the disruption of the hemodynamic environment in the ATAA is investigated by integrating patient-specific computational hemodynamics, CT-based *in vivo* estimation of local aortic stiffness and Eulerian-based WSS topological skeleton analysis. The final aim is investigate the links between arterial wall degeneration and hemodynamic insult.

Chapter 9: Wall Shear Stress Topological Skeleton Features in Image-Based Stented Coronary Bifurcation Models

This chapter focuses on the exploration of the WSS topological skeleton features in image-based computational fluid dynamics stented coronary artery models, aiming at investigating the possible role of WSS topological features in the process leading to sent failure, e.g., in-stent-restenosis.

Chapter 10: The Variability of the Shear Stress Contraction/Expansion Action Contributes to Wall Thickness Change in Coronary Arteries

The aim of this chapter is to investigate the significance of WSS topological skeleton in the onset and progression of atherosclerotic plaques in coronary arteries. To do that, the proposed Eulerian approach to analyze WSS topological skeleton features is applied to pig-specific computational hemodynamics models of 9 coronary arteries. In particular, the ability of WSS topological skeleton and related quantities to predict temporal changes in coronary artery Wall Thickness (WT), a hallmark of atherosclerotic plaque progression, is investigated.

Chapter 11: Conclusions and Future Works

In this chapter, concluding remarks of each chapter are reported and suggestions for future research and ongoing applications are provided.

Chapter 2

Theoretical concepts

In this chapter, we report the theoretical and methodological basis supporting the Lagrangian-based methods currently applied in literature for the analysis of the WSS topological skeleton. Moreover, this chapter provides theoretical background for a better understanding of the theory behind the proposed method, with particular emphasis on the Volume Contraction Theory. For a broader overview of this topic, we refer to [39].

2.1 Topological Skeleton of a vector field

Topological features of a vector field have been largely studied in the context of dynamical systems theory. A dynamical system is defined as a set of n differential equations:

$$\dot{\boldsymbol{x}} = \boldsymbol{u}(\boldsymbol{x}, t), \tag{2.1}$$

where $t \in \mathbb{R}^+$ is the time and and $\boldsymbol{x_0} \in \mathbb{R}^n$ the initial position at time point t_0, i.e., $\boldsymbol{x_0} = \boldsymbol{x}(t_0)$. Given the initial condition $\boldsymbol{x_0} \in \mathbb{R}^n$, a unique solution of eq. (2.1) exists, called trajectory, given by:

$$\boldsymbol{x}(t) = \boldsymbol{x_0} + \int_{t_0}^{t} \boldsymbol{u}(\boldsymbol{x}(s), s)ds, \tag{2.2}$$

Associated with the dynamical system defined in eq. (2.1), the so-called flow map can be defined as follows::

$$\Phi_{t_0}^{t} : \boldsymbol{x_0} \rightarrow \boldsymbol{x}(t), \tag{2.3}$$

providing the expression of all the system trajectories at time t. In general, the topological skeleton of the vector field $\boldsymbol{u}$ is recognized to provide the organizing structures of the system itself.
In steady-state conditions (i.e., when vector field $\boldsymbol{u}(\boldsymbol{x}, t)$ in eq. (2.1) does not explicitly depend on time), the topological skeleton of a vector field consists of a collection of fixed points (Figure 2.1A) and the associated stable and unstable manifolds connecting them (Figure 2.1B). A fixed point is a point $\boldsymbol{x}_{fp} \in \mathbb{R}^n$ where the vector field locally vanishes. The nature of fixed points can be stable or unstable. A stable fixed point is characterized by a sink configuration and it attracts the nearby trajectories, while an unstable fixed point is characterized by a source configuration and it repels the nearby trajectories (Figure 2.1A). A fixed point can be classified as a saddle point, node or focus (Figure 2.1A): (1) a saddle point is a point attracting and repelling nearby trajectories along different directions (i.e., where the streamlines of the vector field intersect themselves); (2) a stable/unstable node is characterized by converging/diverging streamlines; (3) a focus is characterized by spiraling trajectories and it can be attracting or repelling.

Technically, the exact location of fixed points in a domain of interest can be identified by computing the Poincaré index [40], a topological invariant index quantifying how many times a vector field rotates in the neighbourhood of a point. For the sake of simplicity, we consider the dynamical system in eq. (2.1) under steady-state conditions and lying in a 2D space, i.e., $\boldsymbol{u}(\boldsymbol{x}) = (X(\boldsymbol{x}(t), Y(\boldsymbol{x}(t))$, with $\boldsymbol{x} \in \mathbb{R}^2$. An explanatory example of how to calculate the Poincaré index can be then provided. Let $\boldsymbol{x}_{fp} \in \mathbb{R}^2$ be an isolated fixed point of $\boldsymbol{u}$ with a neighbourhood N such that there are no other fixed points in N that $\boldsymbol{x}_{fp}$, and let γ be a closed curve inscribing N. Then, the Poincaré index $\mathcal{I}(\gamma, \boldsymbol{u})$ of the curve γ relative to $\boldsymbol{u}$ is the number of the positive field rotations while travelling along γ in positive direction:

$$\mathcal{I}(\gamma, \boldsymbol{u}) = \frac{1}{2\pi} \int_{\Gamma} d\theta = \frac{1}{2\pi} d \arctan \frac{Y}{X}, \tag{2.4}$$

where θ is the vector field angular variation. The Poincaré index is equal to -1 at saddle point locations (Figure 2.1A), 1 at node or focus locations (Figure 2.1A) and 0 otherwise. The Poincaré index allows to identify fixed points locations, but it does not provide information about the fixed points nature. Therefore, a criterion to distinguish between a node or a focus and between the attractive or repelling nature of a fixed point is needed. In light of this, the vector field $\boldsymbol{u}$ around the

fixed point $\boldsymbol{x}_{fp}$ can be expressed by linearization as:

$$\boldsymbol{u}(\boldsymbol{x}) = \boldsymbol{u}(\boldsymbol{x}_{fp}) + J(\boldsymbol{x}_{fp})(\boldsymbol{x} - \boldsymbol{x}_{fp}), \tag{2.5}$$

where J is the Jacobian matrix of $\boldsymbol{u}$. The fixed point classification can be thus performed by computing the eigenvalues of the Jacobian matrix J, as summarized in Table 2.1. In detail, two real eigenvalues with different signs identify a saddle point. Two real eigenvalues with the same sign identify a node, whose nature is characterized as attracting or repelling (i.e., stable or unstable, respectively) according to their sign (negative or positive, respectively). Complex conjugate eigenvalues identify a stable or unstable focus, according to the sign of the real part (negative or positive, respectively).

Table 2.1: Classification of fixed points based on the eigenvalues of the Jacobian matrix.

$\boldsymbol{\lambda}$	**Fixed point**	**Poincaré index**
$\lambda_1 < 0 < \lambda_2$	Saddle point	-1
$\lambda_1, \lambda_2 > 0$	Unstable node	1
$\lambda_1, \lambda_2 < 0$	Stable node	1
$\lambda_{1,2} = \alpha \pm \beta i$	Unstable focus	1
$\lambda_{1,2} = -\alpha \pm \beta$	Stable focus	1

The stable and unstable manifolds associated with a fixed point $\boldsymbol{x}_{fp}$ are composed by all initial conditions $\boldsymbol{x_0} \in \mathbb{R}^n$ such that the trajectories initiated at these points $\boldsymbol{x_0}$ approach the fixed point $\boldsymbol{x}_{fp}$ asymptotically. By construction, stable and unstable manifolds act as separatrices of the vector field, portioning regions of different behavior and dynamics. In particular an unstable manifold attracts nearby trajectories, as opposed to the stable manifold, which repels nearby trajectories (Figure 2.1B). In mathematical terms, an unstable manifold $\boldsymbol{W^u}$ associated with the generic fixed point $\boldsymbol{x}_{fp}$ is defined as follows:

$$\boldsymbol{W^u}(\boldsymbol{x}_{fp}) = \{\boldsymbol{x}_0 \in \mathbb{R}^n : \Phi(\boldsymbol{x}_0, t) \to \boldsymbol{x}_{fp} \text{ as } t \to +\infty\}, \tag{2.6}$$

while a stable manifold $\boldsymbol{W^u}$ can be expressed as:

$$\boldsymbol{W^s}(\boldsymbol{x}_{fp}) = \{\boldsymbol{x}_0 \in \mathbb{R}^n : \Phi(\boldsymbol{x}_0, t) \to \boldsymbol{x}_{fp} \text{ as } t \to -\infty\}. \tag{2.7}$$

When the vector field $\boldsymbol{u}(\boldsymbol{x}, t)$ in eq. (2.1) is time-dependent, solutions can be complex and chaotic, making difficult (or even misleading) the interpretation of the topological skeleton made of $\boldsymbol{W^u}$,$\boldsymbol{W^u}$ and $\boldsymbol{x}_{fp}$. In general, two different perspectives have been proposed to identify manifolds of a vector field. The Lagrangian perspective considers individual particles, tracking their motion along their paths as they are advected by the flow field. By contrast, the Eulerian perspective considers the properties of the vector field under-analysis at each fixed location in space and time. In the following sections, a brief theoretical background is reported for a better understanding of the theory supporting the Lagrangian and Eulerian approaches to analyse vector field topology, with particular emphasis on the application to cardiovascular flows.

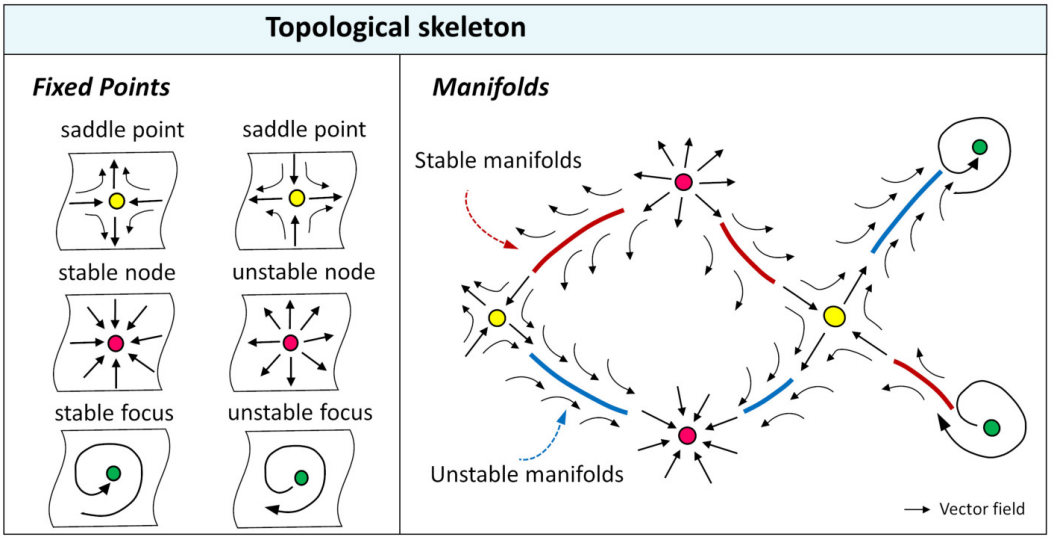

Figure 2.1: A) Classification of fixed points in a vector field. B) Stable and unstable manifolds associated with fixed points of a vector field connecting fixed points, denoted as W^s and W^u, respectively.

2.2 Lagrangian approach

2.2.1 Lagrangian Coherent Structures

The need to robustly define intrinsic structures governing fluid/mass transport under unsteady-state conditions has led to the development of the concept of Coherent Structures (CS). Technically, CS are defined as emergent patterns

influencing the transport of tracers/mass in time-dependent flows [41]. In this context, *Lagrangian Coherent Structures* are coherent structures identified by applying methods based on a Lagrangian approach. The theory supporting the concept of LCS is based on methods inspired by non-linear dynamics, chaos theory and fluid dynamics.
From a mathematical perspective and in relation to fluid mechanics, LCS can be defined as material surfaces in the flow field which are dominant in attracting or repelling neighbouring fluid elements over a defined time interval [42, 43]. These material surfaces are able to localize where the flow field experiences the largest and the smallest stretching [38]. In detail, material surfaces in the flow field attracting trajectories more strongly than any other nearby material surface are referred to as *attracting LCS*. On the contrary, material surfaces repelling trajectories more strongly than any other nearby material surface are referred to as *repelling LCS*. The detection and visualization of LCS is usually performed by applying two different Lagrangian-based approaches. Both approaches are based on particle paths information derived from post-processing velocity data obtained by CFD simulations, or by in vivo (e.g., Phase-Contrast Magnetic Resonance Imaging (PC MRI)) and in vitro (e.g., particle image velocimetry) measurements. The workflow of the Lagrangian-based approaches to visualize LCS is sketched in Figure 2.2.

The first approach to characterize unsteady flows and to understand transport topology is the *Lagrangian particles tracking*, performed by seeding with tracer particles the domain of interest and by visualizing their motion (Figure 2.2). The aim is to reveal coherent features revealing how the flow under analysis is organized. From a mathematical perspective, the position of a tracer particle is governed by the differential equation reported in eq. (2.1). To obtain the position of such particle at a desired time t, eq. (2.1) is numerically integrated from t_0 to t. The direct integration of tracer particles allows for an in-depth understanding of how tracers are transported through the domain of interest. In detail, attracting LCS will be generally distinguishable since tracer particles are attracted to and along these surfaces (Figure 2.3). Analogously, repelling LCS will be distinguishable from advection of tracer particles by reversing time (Figure 2.3). Attracting LCS are traced out with forward time integration of particles, while repelling LCS are traced out with backward time integration of particles.

Lagrangian particle tracking represents a Lagrangian-based technique aiming at overcoming issues related to standard approaches used for topological skeleton

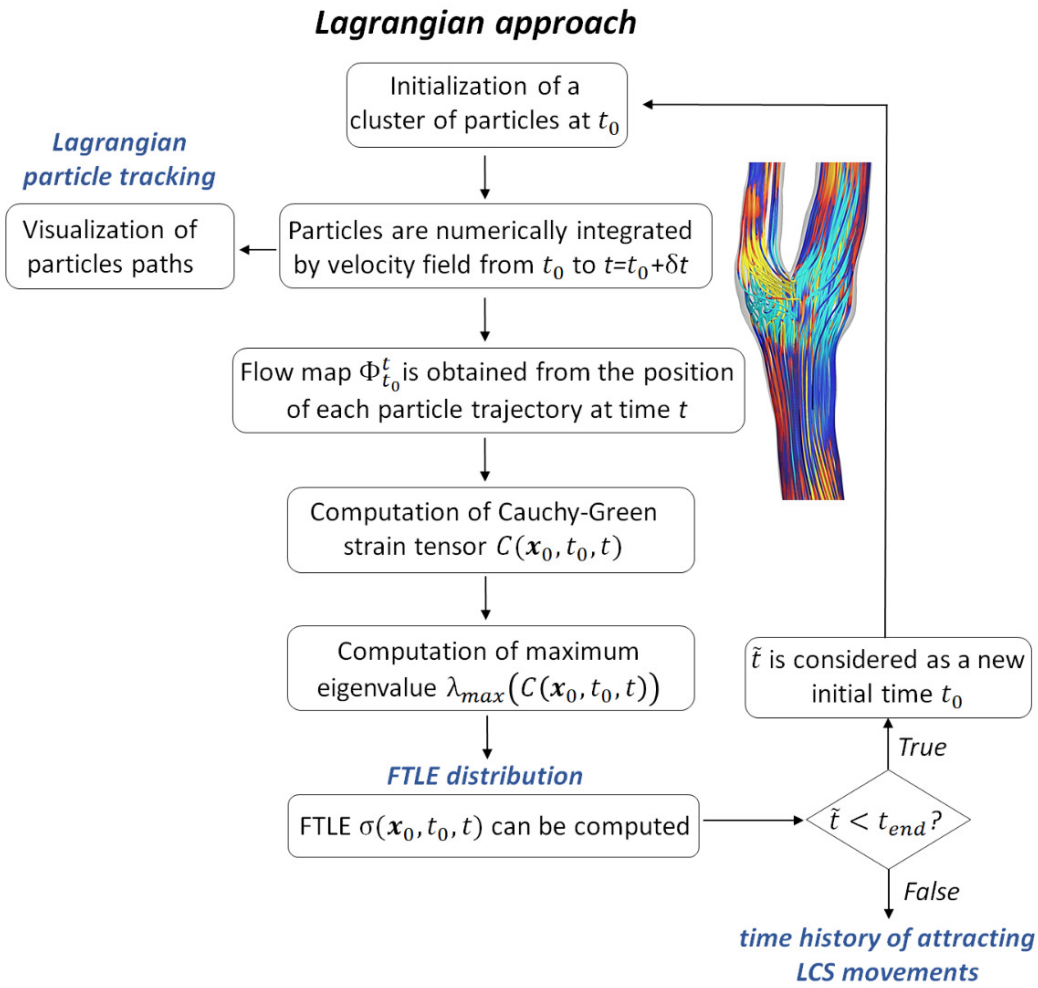

Figure 2.2: Workflow of the Lagrangian-based approaches to visualize attracting LCS starting from a cluster of particles at time t_0 over the domain of interest. The same procedure applies for repelling LCS by considering reversing time. FTLE: finite time Lyapunov exponent.

extraction of vector field with unsteady-state conditions. However, the resulting tracer particles motion complexity could obscure the interpretation of vector field topology.

For this motivation, the second approach consists in the computation of the finite time Lyapunov exponent (FTLE) (Figure 2.2). Based on theory, a LCS can be defined as the material surface that locally maximizes the FTLE [42, 44], being the Lyapunov exponent a measure of the sensitivity to initial position of a dynamical system. Technically, the finite time Lyapunov exponent $\sigma(\boldsymbol{x_0}, t_0, t)$ [42, 43, 45, 46,

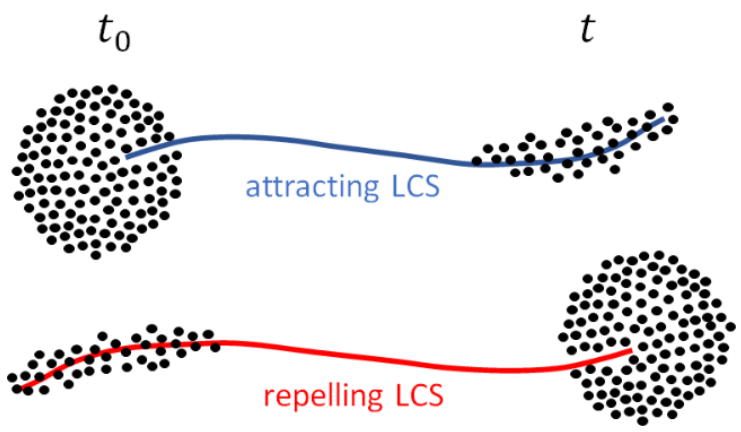

Figure 2.3: Explanatory sketch of attracting and repelling LCS over time interval $[t_0, t]$. A sphere of tracer particles released at time t_0 will spread out along the attracting LCS at time t. The opposite occurs for the repelling LCS, considering reversing time.

47, 48] is defined as:

$$\sigma(\boldsymbol{x_0}, t_0, t) = \frac{1}{|t - t_0|} \ln \sqrt{\lambda_{max}(C(\boldsymbol{x_0}, t_0, t))}, \tag{2.8}$$

where λ_{max} is the maximum eigenvalue of the right Cauchy-Green strain tensor $C(\boldsymbol{x_0}, t_0, t)$:

$$C(\boldsymbol{x_0}, t_0, t) = \nabla \Phi_{t_0}^t(\boldsymbol{x}_0)^T \nabla \Phi_{t_0}^t(\boldsymbol{x}_0), \tag{2.9}$$

where $\nabla \Phi_{t_0}^t(\boldsymbol{x}_0)^T$ denotes the transpose of the gradient of the flow map in eq. (2.3). By a physical point of view, $C(\boldsymbol{x_0}, t_0, t)$, in eq.(2.9) represents the material deformation of infinitesimal volume elements and it is a symmetric and positive-definite matrix. Roughly speaking, the FTLE σ defined in eq. (2.8) measures the rate of separation of initially close vector field trajectories. Let δ_0 be a small distance between two materials points at time t_0, as depicted in Figure 2.4, then it can be demonstrated [41] that the separation δ_t after the time interval $|t - t_0|$ satisfies the inequality:

$$||\delta_t|| \leq e^{\sigma(\boldsymbol{x_0}, t_0, t)|t - t_0|} ||\delta_0||, \tag{2.10}$$

where equality holds if the initial distance δ_0 is aligned with the eigenvector of $C(\boldsymbol{x_0}, t_0, t)$ associated with λ_{max}.

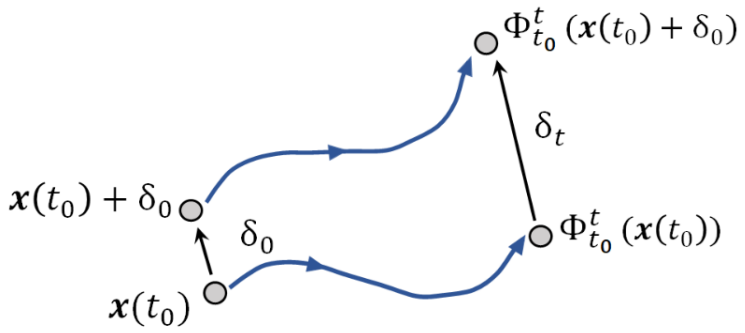

Figure 2.4: Explanatory sketch of separation of nearby particles, released at the same time t_0 due to the flow map $\Phi_{t_0}^{t}$, during time interval $|t-t_0|$.

The algorithm for LCS identification based on FTLE computation starts with the initialization of a cluster of massless elemental particles at time t_0 over the domain of interest (Figure 2.2). Then, particles are numerically integrated by the velocity field in eq. (2.1) from t_0 to t and their trajectories are calculated. The flow map $\Phi_{t_0}^{t}$ (eq. (2.3)) is obtained from the final position of each particle trajectory at time t in the domain and subsequently its gradient $\nabla\Phi_{t_0}^{t}(\boldsymbol{x_0})$ can be computed. For a structured grid, $\nabla\Phi_{t_0}^{t}(\boldsymbol{x_0})$ can be calculated by finite differencing, e.g., using central differencing as follows:

$$\nabla\Phi_{t_0}^{t}(\boldsymbol{x}_0) \approx \begin{bmatrix} \frac{x_{(i+1)jk}(t)-x_{(i-1)jk}(t)}{x_{(i+1)jk}(t_0)-x_{(i-1)jk}(t_0)} & \frac{x_{i(j+1)k}(t)-x_{i(j-1)k}(t)}{y_{i(j+1)k}(t_0)-y_{i(j-1)k}(t_0)} & \frac{x_{ij(k+1)}(t)-x_{ij(k-1)}(t)}{z_{ij(k+1)}(t_0)-z_{ij(k-1)}(t_0)} \\ \frac{y_{(i+1)jk}(t)-y_{(i-1)jk}(t)}{x_{(i+1)jk}(t_0)-x_{(i-1)jk}(t_0)} & \frac{y_{i(j+1)k}(t)-y_{i(j-1)k}(t)}{y_{i(j+1)k}(t_0)-y_{i(j-1)k}(t_0)} & \frac{y_{ij(k+1)}(t)-y_{ij(k-1)}(t)}{z_{ij(k+1)}(t_0)-z_{ij(k-1)}(t_0)} \\ \frac{z_{(i+1)jk}(t)-z_{(i-1)jk}(t)}{x_{(i+1)jk}(t_0)-x_{(i-1)jk}(t_0)} & \frac{z_{i(j+1)k}(t)-z_{i(j-1)k}(t)}{y_{i(j+1)k}(t_0)-y_{i(j-1)k}(t_0)} & \frac{z_{ij(k+1)}(t)-z_{ij(k-1)}(t)}{z_{ij(k+1)}(t_0)-z_{ij(k-1)}(t_0)} \end{bmatrix} \tag{2.11}$$

Once the flow map gradient is obtained, Cauchy-Green strain tensor $C(\boldsymbol{x_0}, t_0, t)$ can be computed according to eq. (2.9).

Finally, the maximum eigenvalue $\lambda_{max}(C(\boldsymbol{x}_0, t_0, t))$, and the FTLE $\sigma(\boldsymbol{x}_0, t_0, t)$ as well, can be computed according to eq. (2.8) (Figure 2.2). The obtained $\sigma(\boldsymbol{x}_0, t_0, t)$ value for each particle is assigned to the particle position at time t_0. This procedure is repeated varying the timet_0 (e.g., within the cardiac cycle in cardiovascular applications) aiming at providing the time series of FTLE values and ultimately the time history of LCS movements (Figure 2.2). Positive integration times reveal repelling LCS in the FTLE field and negative integration times reveal attracting LCS in the FTLE field.

In general, the computation of the spatial variation of FTLE filed requires the velocity field to be interpolated in both time and space and high-order integration and interpolation schemes are needed to ensure accuracy of results. Furthermore, the mesh used to compute FTLE distribution over the domain of interest is more resolved than the velocity mesh, aiming at correctly detecting LCS.

2.2.2 LCS application to intravascular flows

Lagrangian-based approaches have been largely applied to identify LCS in intravascular flows. Indeed, Lagrangian particle tracking has been massively applied to explore the complexity of intravascular flows, e.g., to provide a measure of stasis in idealized computational bifurcation models [49], or to study vortices generation and their potential role in thrombogenesis in idealized aneurysm models [50, 51]. Several studies have applied particle tracking to identify flow disturbances in e.g., carotid bifurcation models, contributing to provide a deeper understanding of the hemodynamics-driven processes underlying atherosclerosis onset/progression [52, 53, 54, 55]. Moreover, particle tracking has been used to study the hepatic perfusion in the Fontan circulation [56, 57], identify the optimal left ventricular assist device cannula outflow configurations [58], obtain a deeper understanding of the dynamics of embolic particles within arteries [59], and identify peculiar intravascular helical flow patterns in the aorta from in vivo 4D flow MRI data [60, 61]. As regards the FTLE-based analysis of the flow field, its extension to intravascular flows is relatively recent, motivated by the fact that LCS are determined by blood flow structures associated to adverse vascular events including flow stagnation, separation and recirculation. Among the main contributions, here we mention that Shadden and Taylor [46] used LCS to quantify the extent of flow stagnation, to determine where flow separates and to understand how flow is partitioned to downstream vasculature in computational hemodynamic models of large vessels. LCS have been proposed as a powerful method to capture vortex transport in blood flow. In this regard, Arzani and Shadden [62] used LCS to characterize the hemodynamics in Abdominal Aortic An-eurysm (AAA) models, suggesting the AAA intravascular flow topology is dictated by the systolic vortex propagation through the abnormal vessel. Arzani *et al.* [63] computed FTLE fields and associated LCS to capture a large coherent vortex in AAA computational models. Furthermore, LCS have been applied to identify left ventricle (LV) blood flow features during heart

filling. In detail, Gharib *et al.* [64] used LCS to demonstrate the existence of a link between the vortex ring formation inside the LV and ejection fraction. Charonko *et al.* [65] quantified the vortex ring volume by computing LCS from in vivo LV phase contrast magnetic resonance imaging data of healthy and diseased patients. Töger *et al.* [66] extracted LCS from in vivo LV phase contrast magnetic resonance imaging data to measure the vortex ring volume during rapid filling of the LV. The identification of attracting and repelling LCS from LV Doppler-echocardiography data was adopted as a criterion to discriminate between healthy and diseased patients [67]. Other studies applied LCS to characterize the flow field through heart valves. In particular, LCS were extracted to delineate the boundaries of the outflow jet downstream of aortic valves, used as a measure of the severity of valve's stenosis [68, 69]. In a very recent study [70], FTLE-based LCS detection on computational hemodynamics models of aortic bicuspid and mechanical heart valves was used to study those mass transport processes that might be related to valve disease. The analysis of the fluid dynamics in the neighborhood of blood clots was another effective application of LCS to hemodynamics which allowed to highlight how blood is transported close to a clot [71]. In addition, FTLE-based analysis was adopted to highlight the hemodynamic impact of flow diverter stents in the treatment of intracranial aneurysms [72, 73]. We refer the interested reader to the ref. [45] for a broader, detailed overview of Lagrangian methods used in post-processing velocity data in cardiovascular flows.

2.2.3 LCS application to near-wall flow features

Recently, in studying cardiovascular flows the concept of LCS has been extended to analyze the near-wall flow topology, i.e., the topology of the flow field close to the luminal surface of arteries. The rationale is in the well-established involvement of WSS and near-wall mass transport in most of the processes concurring to determine vascular pathophysiology [74]: in the near-wall region, blood flow regulates the local bio-transport processes and imparts mechanical shear stress on the endothelium, which in turn regulate important developmental, homeostatic and adaptive mechanisms in arteries, as well as susceptibility to and progression of atherosclerosis [75]. Based on theory, it has been demonstrated [76] that the WSS vector field can be scaled to provide a first-order approximation for the near-wall blood flow velocity vector field $\boldsymbol{u}_\pi \in \mathbb{R}^3$ as follows:

$$\boldsymbol{u}_\pi \simeq \frac{\boldsymbol{\tau}\delta n}{\mu} + O(\delta n^2), \tag{2.12}$$

where $\boldsymbol{\tau} \in \mathbb{R}^3$ represents the WSS vector field, μ is the dynamic viscosity and δn is the distance from the wall where the velocity is evaluated. From a mathematical perspective, the WSS vector $\boldsymbol{\tau}$ can be defined as:

$$\boldsymbol{\tau} = \mu(\nabla u + \nabla^T u) \cdot \boldsymbol{n} - (\mu(\nabla u + \nabla^T u) \cdot \boldsymbol{n}) \cdot \boldsymbol{n}, \tag{2.13}$$

where $\boldsymbol{n}$ is the outward unit vector.

As demonstrated elsewhere [76], the near-wall velocity $\boldsymbol{u}_\pi$ in eq. (2.12) is predominantly tangential to the wall (the additional component of the velocity normal to the wall being second order in δn, can be considered to have less a lesser degree of importance in the analysis).

By construction, the vector field in eq. (2.12) is defined on the luminal surface of the vessel and it represents the near-wall velocity, as the velocity is zero on the surface itself due to the no-slip condition. The LCS underlying theory described in Section 2.2.1 can be extended to analyse the near-wall flow topology, by using the expression of near-wall velocity $\boldsymbol{u}_\pi$ (given by eq. (2.12)) in eq. (2.1). Such near-wall Lagrangian structures, computed from WSS vector field, are referred to as WSS LCS [23].

Computationally, WSS LCS can be identified on the luminal surface of the vessel by numerically integrating a high number of luminal surface tracer particles, applying the procedure described in the first part of Section 2.2.1. In particular, attracting and repelling WSS LCS can be traced out with forward and backward time integration of surface tracer particles based on the near-wall blood flow velocity (eq. (2.12)), respectively.

The recent interest in WSS LCS by the cardiovascular fluid mechanics research community was driven by their ability to highlight blood flow features associated with vascular disease initiation and progression like flow stagnation, separation, and recirculation, flow impingement, the interaction of vortex structures with the vascular wall, which are usually classified as “aggravating flow events” [12, 21]. An example of attracting WSS LCS on the luminal surface of a patient-specific computational hemodynamic model of human carotid bifurcation model [20, 77, 19, 78] is presented in Figure 2.5. In this specific case, luminal surface tracer particles (Figure 2.5A) are numerically integrated in forward time. The resulting LCS is located

at the carotid bulb, a region characterized by flow disturbances (slow, recirculating blood flow) promoting atherosclerosis [12, 79]. In detail, the attracting WSS LCS provides the boundary at the luminal surface of the slow vortex structure formed inside the carotid bulb (Figure 2.5C, where the recirculation region is highlighted visualizing the streamlines of the cycle-average velocity vector field).

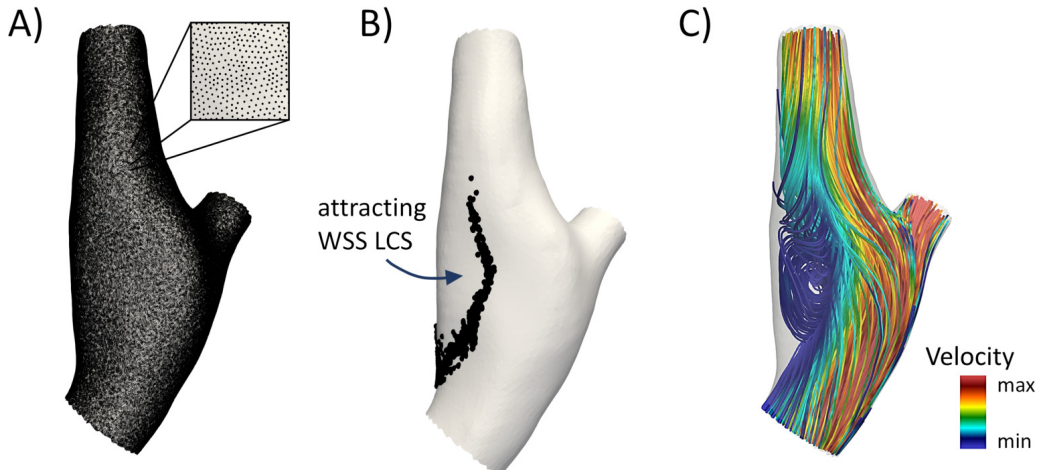

Figure 2.5: A) Initial tracer particles position on the luminal surface of a carotid bifurcation model. B) Attracting WSS LCS traced out from forward time integration of WSS trajectories. C) Streamlines of the cycle-average velocity vector field, coloured by cycle-average velocity magnitude.

In addition, the shear forces exerted by the streaming blood flow in the near-wall region on the endothelium affect biotransport processes, i.e., the transport of biochemicals through the subendothelial layer [11]. Biotransport is of paramount importance in many cardiovascular processes, including the initiation of atherosclerosis, endothelial cell vasoregulation, and thrombogenesis [26]. In general, cardiovascular mass transport is investigated in silico by coupling the governing equations of motion, the Navier-Stokes equations, with the advection-diffusion equation, given by:

$$\frac{dC}{dt} + \boldsymbol{u} \cdot \nabla - D\nabla^2 C = 0, \tag{2.14}$$

where C is a non-dimensional concentration,$\boldsymbol{u}$ is the fluid velocity vector, and D is the mass diffusion coefficient of the species transported in the fluid domain. However, high computational cost are associated with the class of numerical simulations used to accurately solve the near-wall transport and blood-wall transfer [80, 81], making such approach prohibitively expensive in hemodynamics applications. To

overcome this limitation, and based on the well-established role that WSS plays in conditioning the permeability of the endothelium and the near-wall mass transport process as well, recent studies [23, 22] have brilliantly demonstrated that WSS LCS can be used as a template of near-wall mass transport, thus reducing the computational effort needed to solve the full transport problem represented by eq. (2.14) [23]. In particular, it has been demonstrated that attracting WSS LCS attract biochemicals, leading to high near-wall concentration in their neighbourhood, whereas repelling WSS LCS have been shown to act as near-wall transport barriers [23, 22, 21].

In the context of cardiovascular flows, it has been recently demonstrated that attracting/repelling WSS LCS on the luminal surface of an artery match the unstable/stable manifolds of the steady cycle-average WSS vector field [23, 22], defined as:

$$\bar{\boldsymbol{\tau}} = \frac{1}{T}\int_0^T \boldsymbol{\tau}(\boldsymbol{x}, t)dt, \tag{2.15}$$

where $\boldsymbol{\tau}$ is the instantaneous local WSS value and T is the time duration of the cardiac cycle. Technically, the first steps in the topological analysis of cycle-average WSS at the luminal surface of a vessel is the identification of WSS fixed points. The extract position of WSS fixed points can be identified by computing, e.g., the Poincaré index, as explained in Section 2.1. Then, the cycle-average WSS field around a fixed point $\boldsymbol{x}_{fp}$, according to eq. (2.5), by linearization can be expressed as:

$$\bar{\boldsymbol{\tau}}(\boldsymbol{x}) = \bar{\boldsymbol{\tau}}(\boldsymbol{x}_{fp}) + J(\boldsymbol{x}_{fp})(\boldsymbol{x} - \boldsymbol{x}_{fp}), \tag{2.16}$$

where J is the Jacobian matrix of $\bar{\boldsymbol{\tau}}$. The identified WSS fixed points can be classified according to their nature (saddle, node or focus, Figure 2.1A) by analyzing the eigenvalues of the Jacobian matrix J of $\bar{\boldsymbol{\tau}}$ (Table 2.1), as described in Section 2.1. Note that WSS vector field is embedded in a three-dimensional space, even if it lies in a two-dimensional space (the luminal surface of a vessel). To perform a two-dimensional analysis, two strategies are possible. In the first strategy, a projection of the vector field into two orthogonal directions (hence, in a two-dimensional space) is needed. In the second one, avoiding the projection of the vector field (and thus reducing the computational steps), a three-dimensional analysis can be performed, thus obtaining three eigenvalues of the Jacobian matrix, with one of them having value close to zero. Then, the eigenvalue-based analysis for the WSS fixed

points classification can be performed by considering the two eigenvalues different from zero. Saddle-type fixed points are of particular interest since typically a stable or unstable manifold starts from a saddle point and varnishes into a source or sink, respectively, as depicted in Figure 2.1B. Saddle point locations (where Poincaré index is -1 and the eigenvalues are real with different sign) are perturbed along the positive eigenvector of J in two opposite directions obtaining two initial conditions [22, 31]. Unstable manifolds can be traced out by numerically integrating $\bar{\boldsymbol{\tau}}$ from these initial conditions in forward time until trajectories reach a stable fixed point (sink configuration) or leave the domain. Similarly, stable manifolds are delineated by integrating $\bar{\boldsymbol{\tau}}$ in backward time starting from the perturbation of saddle point location along the negative eigenvector of J until trajectories reach an unstable fixed point (source configuration) or leave the domain.
An example of unstable manifolds of cycle-average WSS on the luminal surface of a patient-specific computational hemodynamic model of human carotid bifurcation model [20, 77, 19, 78] is presented in Figure 2.6. WSS fixed points were identified by computing Poincaré index (Figure 2.6A) and subsequently unstable manifolds were traced out by applying *Runge Kutta 4-5* numerical integration scheme (Figure 2.6B). By visual inspection of Figure 2.6C it can be appreciated that cycle-average WSS unstable manifolds co-localize with attracting WSS LCS, confirming the capability of the latter to identify critical lines of the WSS field.

The analysis of cycle average WSS fixed points and manifolds has been applied to analyze cardiovascular flows. Arzani *et al.* [22] computed WSS LCS from stable and unstable manifolds of cycle-average WSS on patient-specific computational hemodynamics models of AAAs, carotid arteries, cerebral aneurysms and coronary aneurysm to characterize near-wall flow topology and biochemicals transport. Farghadan *et al.* [24] used WSS topology and magnitude analysis to predict surface concentration patterns in cardiovascular transport problems by computing WSS LCS from manifolds of cycle-average WSS in image-based coronary and carotid artery models. Mahmoudi *et al.* [25] studied the near-wall transport of some of the prominent biochemicals contributing to the initiation and progression of atherosclerosis in computational hemodynamics models of coronary artery, highlighting the strength of cycle-average WSS LCS as a template of luminal surface concentration and flux patterns of biochemicals transported with blood.
Summarizing, the Lagrangian approach for identifying near-wall topological features is summarized in Figure 2.7, where the link between attracting/repelling WSS

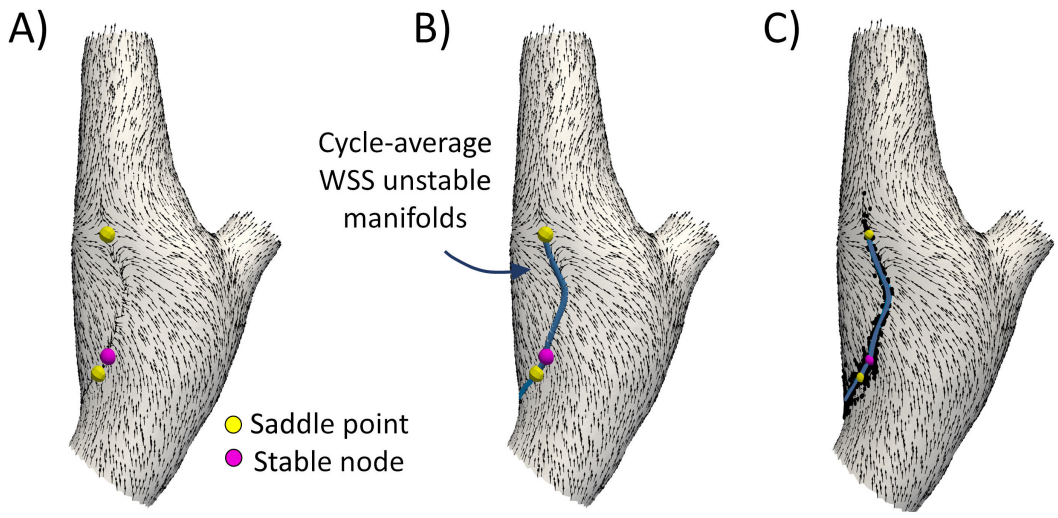

Figure 2.6: A) Cycle-average WSS fixed points on the luminal surface of a carotid bifurcation model. B) Unstable manifolds of cycle-average WSS (blue lines) traced out by integrating cycle-average WSS vector starting from saddle point positions. C) Cycle-average WSS unstable manifolds superimposed on the attracting WSS LCS. Vectors are normalized for visualization.

LCS with unstable/stable cycle-average WSS manifolds, respectively, is highlighted. In addition, Figure 2.7 presents a briefly summary of the link between Lagrangian-based near-wall flow topology and mass transport. For a more in-depth analysis, the interested reader could refer to recent literature [23, 21, 22, 25]where the link between WSS LCS, cycle-average WSS manifolds and biochemical transport in cardiovascular flows is unambiguously documented.

2.3 Eulerian approach

2.3.1 Volume Contraction Theory

The Volume Contraction theory provides a simple alternative way to analyse the behaviour of a dynamical system from a Eulerian perspective. Contrarily to Lagrangian-based approaches, the Eulerian perspective considers vector field properties at each point in space and time. The presented Volume Contraction theory, based on fluid mechanics and differential geometry, is focused on the temporal change of an elemental volume (of fluid, for the case of interest) in the phase space

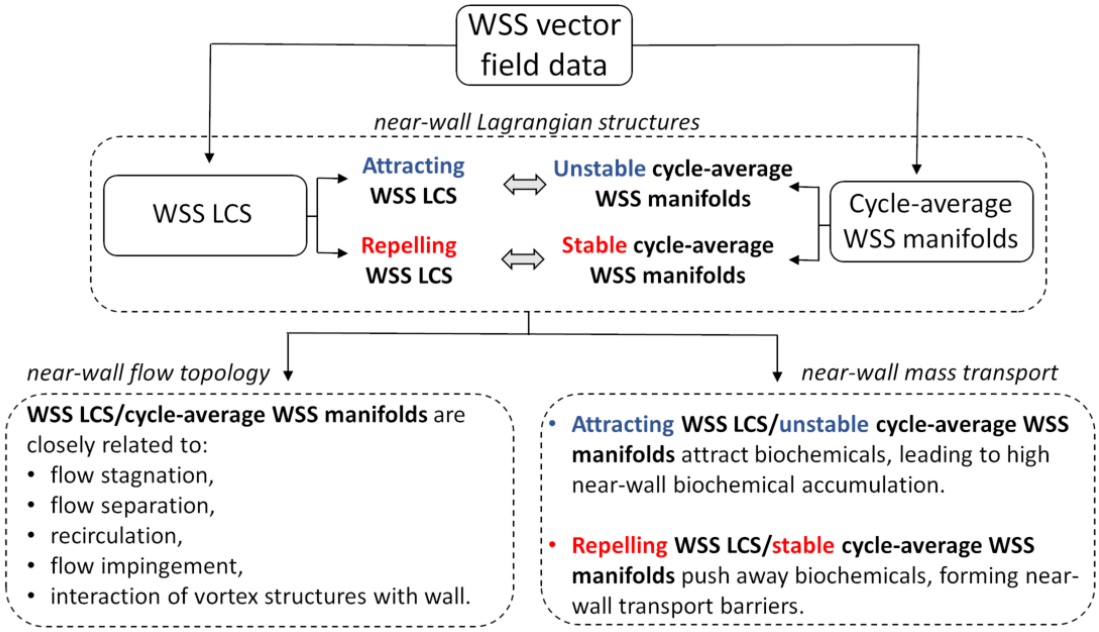

Figure 2.7: Workflow for the near-wall Lagrangian structures identification. The link between WSS LCS and cy-cle-average WSS manifolds and their role in near-wall flow topology and near wall mass transport is highlighted.

of a dynamical system (fluid flow, for the case of interest). Let $V(t)$ be an arbitrary volume in the phase space of the dynamical system defined in eq. (2.1). Let $S(t)$ be a closed surface enclosing the volume $V(t)$, i.e., such that $S(t) = \delta V(t)$. $S(t)$ evolves during the time interval dt resulting in an expansion or contraction of the volume, as depicted in Figure 2.8. The rate of volume variation, that we will call volume contraction rate from now, as a consequence of the application of the Gauss theorem can be expressed as follows:

$$\frac{dV(t)}{dt} = \int\int_S \boldsymbol{u} \cdot \boldsymbol{n} dS = \int\int\int_V \nabla \cdot \boldsymbol{u} dV, \tag{2.17}$$

where $\boldsymbol{u}$ is the vector field defined in eq. (2.1) and $\boldsymbol{n}$ is the unit normal to the surface S (Figure 2.8).

Shrinking the near-wall volume V to zero, it can be written:

$$\lim_{V\to 0} \frac{1}{V}\frac{dV(t)}{dt} = \lim_{V\to 0} \frac{1}{V} \int\int\int_V \nabla \cdot \boldsymbol{u}\, dV = (\nabla \cdot \boldsymbol{u}), \tag{2.18}$$

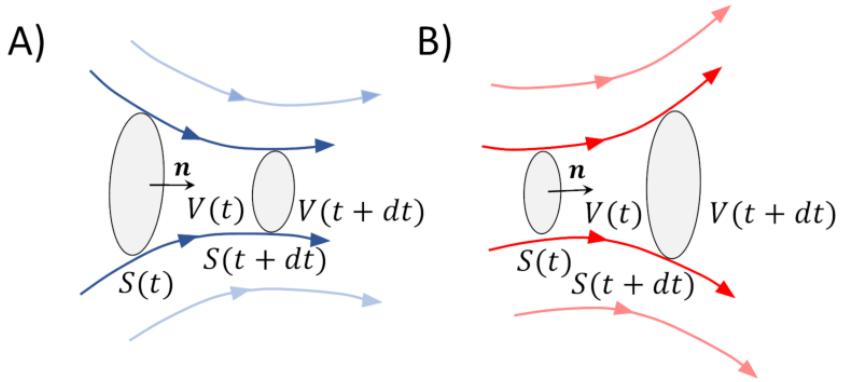

Figure 2.8: Explanatory sketch of A) volume contraction and B) volume expansion in the phase space of a dynamical system.

Eq. (2.18) clearly shows that in the limit as V approaches zero, the local value of vector $\boldsymbol{u}$ divergence is equal to its total flux per unit volume.
In general, in non-conservative dynamical systems the volume of phase space is not preserved as it can contract or expand. Thus, trajectories tend to a lower-dimensional subset of phase space. From eq. (2.18), the volume contraction rate $\Gamma(\boldsymbol{x}, t)$ of a n-dimensional system, representing the rate of separation of infinitesimal close trajectories, can be obtained as:

$$\Lambda(\mathbf{x}, t) = \nabla \cdot \boldsymbol{u}(\boldsymbol{x}, t) = trJ(\boldsymbol{u}) = \sum_{i=1}^{n} \lambda_i, \tag{2.19}$$

where $trJ(\boldsymbol{u})$ is the trace of Jacobian matrix and λ_i are its eigenvalues. In terms of physics, the Jacobian matrix describes how a small change at a starting point $\boldsymbol{x}_0$ propagates to the final point of the flow map $\Phi_{t_0}^{t}(\boldsymbol{x}_0)$ in eq. (2.3), which is like to say that eq. (2.19) is the same as the sum of Lyapunov exponents in eq. (2.8).

2.3.2 Volume Contraction Theory in cardiovascular flows

Here we demonstrate that the application of the Volume Contraction theory to cardiovascular flows allows to easily analyse the WSS topological skeleton on the luminal surface of a vessel through the direct calculation of the WSS divergence.
Let $\Omega \subset \mathbb{R}^3$ be a bounded domain representing the lumen of a vessel. For each $\boldsymbol{x} \in \Omega$ abd time t, we denote by $\boldsymbol{u}_\pi(\boldsymbol{x}, t)$ the tangential component of the velocity close to the luminal surface. Let $V_\pi(t)$ be an elemental volume near the wall, as

depicted in Figure 2.9. Let $\tilde{\boldsymbol{x}}_w + \delta n \in \Omega$ be a point inside the volume $V_\pi(t)$ and let $\tilde{\boldsymbol{x}}_w$ be a point on the luminal surface such that the distance in the normal to the wall direction between the two points is δn (Figure 2.9).

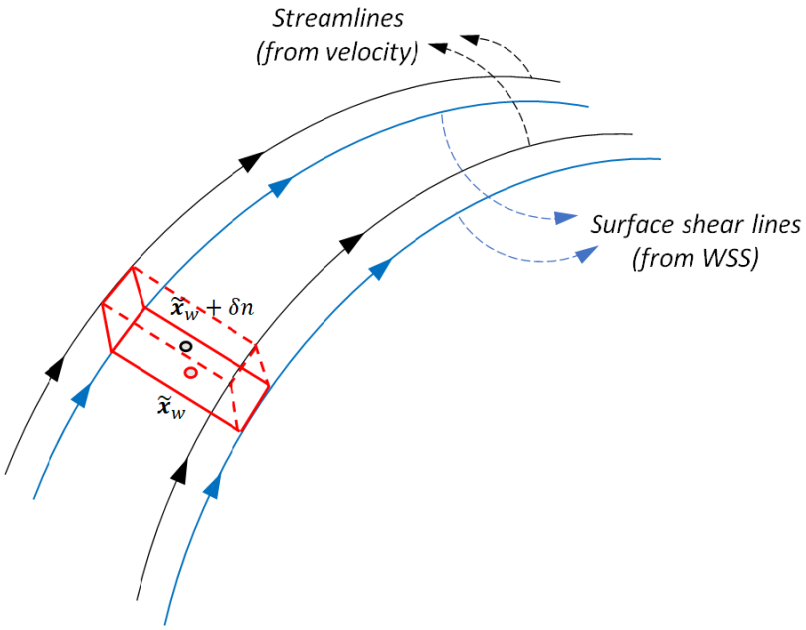

Figure 2.9: Explanatory sketch of an elemental volume $V_\pi(t)$ near the wall. $\tilde{\boldsymbol{x}}_w + \delta n$ is a point inside the volume and $\tilde{\boldsymbol{x}}_w$ is a point on the wall.

Shrinking the near-wall volume V_π to zero, we obtain:

$$\lim_{V_\pi \to 0} \frac{1}{V_\pi} \frac{dV_\pi(t)}{dt} = \lim_{V_\pi \to 0} \frac{1}{V_\pi} \int\int\int_{V_\pi} \nabla \cdot \boldsymbol{u}_\pi dV_\pi = (\nabla \cdot \boldsymbol{u}_\pi)|_{\tilde{\boldsymbol{x}}_w + \delta n}. \tag{2.20}$$

Using eq. (2.12) in eq. (2.20) and assuming Newtonian behaviour for the fluid, it follows that:

$$(\nabla \cdot \boldsymbol{u}_\pi)|_{\tilde{\boldsymbol{x}}_w + \delta n} \simeq (\nabla \cdot \frac{\delta n}{\mu} \boldsymbol{\tau})|_{\tilde{\boldsymbol{x}}_w} \simeq \frac{\delta n}{\mu} (\nabla \cdot \boldsymbol{\tau})|_{\tilde{\boldsymbol{x}}_w}, \tag{2.21}$$

meaning the WSS divergence gives practical information about the near-wall velocity dynamics and can be adopted to analyse WSS topological skeleton. Note that in general the WSS vector field defined at the luminal surface of a vessel is not conservative, even in the case of incompressible flows.

In general, the application of the volume contraction theory to the analysis of a dynamical system faces one limitation in cases where the distance between two

neighbouring trajectories increases/decreases in spite of a negative/positive value of divergence, respectively. As WSS divergence depends by construction upon the algebraic summation of the magnitude of the single gradients of WSS vector components, in some cases, it might fail to properly identify WSS expansion/contraction configuration patterns, giving rise to situations as the ones depicted in the schematics in Figure 2.10. In fact, these regions describe specific directional arrangements of the vectors, but both variations in magnitude and in direction are accounted for in the divergence. To overcome this limitation, which could markedly affect the application of the Eulerian-based approach to study WSS manifolds in cardiovascular flows, the use of the divergence of the normalized WSS vector field has been considered:

$$DIV_W = \nabla \cdot (\boldsymbol{\tau_u}) = \nabla \cdot (\frac{\boldsymbol{\tau}}{\| \boldsymbol{\tau} \|_2}), \tag{2.22}$$

where $\boldsymbol{\tau_u}$ is the WSS unit vector. DIV_W, neglecting the vector field magnitude variation, allows the unambiguous identification of vector field direction variation only (Figure 2.10). Then, luminal surface regions characterized by negative values of DIV_W are referred to as contraction regions and approximate unstable manifolds. Similarly, regions at the luminal surface characterized by positive values of DIV_W are referred to as expansion regions and approximate stable manifolds. In summary, the divergence of normalized WSS can be used to localize the WSS spatial contraction/expansion configuration patterns at the luminal surface of a vessel, and thus it can be used to approximate WSS unstable/stable manifolds.

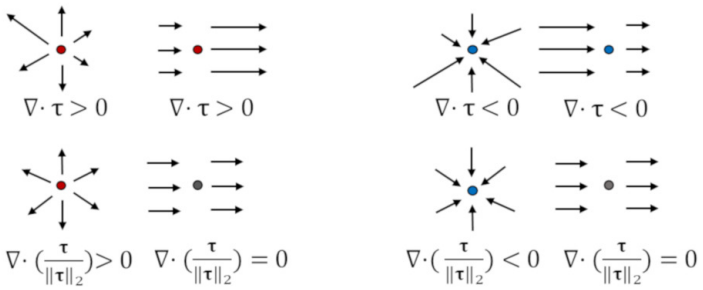

Figure 2.10: Comparison between the divergence of different vector field configuration (top) and divergence of different normalized vector field configuration (bottom).

Non-Newtonian models

Note that in eq. (2.21), Newtonian behaviour for the fluid has been assumed (i.e., constant viscosity μ). Considering the blood as a non-Newtonian fluid, the dynamic viscosity is dependent on the shear rate $\dot{\gamma}$, defined as:

$$\dot{\gamma} = \sqrt{2\boldsymbol{D}(\boldsymbol{u}) : \boldsymbol{D}(\boldsymbol{u})} = \sqrt{2tr(\boldsymbol{D}(\boldsymbol{u})^2)}, \tag{2.23}$$

where $\boldsymbol{D}(\boldsymbol{u}) = \frac{\nabla \boldsymbol{u} + \nabla \boldsymbol{u}^T}{2}$ is the rate of deformation tensor and (:) indicates the double dot product.
Using a Taylor series expansion in space of the the near-wall tangential velocity, we obtain:

$$\boldsymbol{u}_\pi(\tilde{\boldsymbol{x}}_w + \delta n, t) \simeq \boldsymbol{u}_\pi(\tilde{\boldsymbol{x}}_w, t) + (\tilde{\boldsymbol{x}}_w + \delta n - \tilde{\boldsymbol{x}}_w)\frac{\delta \boldsymbol{u}_\pi}{\delta n}|_{\tilde{\boldsymbol{x}}_w} + O(\delta n^2), \tag{2.24}$$

where $\boldsymbol{u}_\pi(\tilde{\boldsymbol{x}}_w, t)$ is equal to zero due to the non-slip condition.
Now considering the definition of the WSS:

$$\boldsymbol{\tau} = \mu(\dot{\gamma})\frac{\delta \boldsymbol{u}_\pi}{\delta n}|_{n=0} \tag{2.25}$$

we obtain:

$$\frac{\delta \boldsymbol{u}_\pi}{\delta n}|_{\tilde{\boldsymbol{x}}_w} = \frac{\boldsymbol{\tau}}{\mu(\dot{\gamma})}|_{\tilde{\boldsymbol{x}}_w}. \tag{2.26}$$

Substituting eq. (2.26) into eq. (2.24), it follows that:

$$\boldsymbol{u}_\pi(\tilde{\boldsymbol{x}}_w + \delta n, t) \simeq \delta n \frac{\boldsymbol{\tau}}{\mu(\dot{\gamma})}|_{\tilde{\boldsymbol{x}}_w} + O(\delta n^2), \tag{2.27}$$

Now eq. (2.21) can be modified as follows :

$$(\nabla \cdot \boldsymbol{u}_\pi)|_{\tilde{\boldsymbol{x}}_w + \delta n} \simeq (\nabla \cdot \frac{\delta n}{\mu(\dot{\gamma})}\boldsymbol{\tau})|_{\tilde{\boldsymbol{x}}_w} \simeq \delta n(\nabla \cdot \frac{\boldsymbol{\tau}}{\mu(\dot{\gamma})})|_{\tilde{\boldsymbol{x}}_w}. \tag{2.28}$$

However, it is trivial to show that:

$$\nabla \cdot (\frac{\frac{\boldsymbol{\tau}}{\mu(\dot{\gamma})}}{\| \frac{\boldsymbol{\tau}}{\mu(\dot{\gamma})} \|_2}) = \nabla \cdot (\frac{\boldsymbol{\tau}}{\| \boldsymbol{\tau} \|_2}) = DIV_W, \tag{2.29}$$

meaning that the quantity used to identify WSS contraction/expansion regions (eq. (2.22)) can be used assuming the blood as a non-Newtonian fluid too, maintaining

the same physical significance.

Remark. *In order to ensure regularity properties of the WSS divergence, we assume the velocity* $\boldsymbol{u}(\boldsymbol{x}, t)$ *to be in the Sobolev space* $H^s(\Omega)$*, which is the space of square integrable functions (i.e., of functions in* $L^2(\Omega)$ *such that all partial derivatives of order up to* s *belong to* $L^2(\Omega)$ *as well.*
The WSS vector is computed from the trace of velocity gradients ($\in H^{s-1/2}(\Omega)$*) and the divergence operator of this vector belongs to* $H^{s-3/2}(\Omega)$*, leading to consider* $s \geq 3/2$*.*
We refer the interest readers to references [82, 83] for a detailed overview of the functional setting of the governing equations of fluid motion (the Navier-Stokes equations).

Chapter 3

Eulerian-based Method for Wall Shear Stress Topological Skeleton Identification

The workflow of the proposed Eulerian-based approach for the WSS topological skeleton identification is provided in Figure 3.1. Briefly, the WSS manifolds are approximated through the divergence of the normalized WSS and WSS fixed points are identified and classified by the Poincaré index and Jacobian matrix analysis, respectively. The single steps of the method are described and detailed in the following sections.

3.1 Wall Shear Stress manifolds identification: Wall Shear Stress divergence

The here proposed Eulerian-based approach to identify WSS topological skeleton requires the computation of the divergence of the WSS data defined on the triangle mesh (i.e., the surface of the tetrahedral volume mesh) obtained from CFD simulations. It is known that polygonal meshes are piecewise linear surfaces and thus the differential operators cannot be directly applied. In this regard, the aim of the Discrete Differential Geometry Theory is to provide robust algorithms to compute approximations of differential operators directly from the mesh data [84]. In particular, based on Discrete Differential Geometry Theory, the gradient of a vertex-based representation of a vector field defined on a triangle mesh embedded

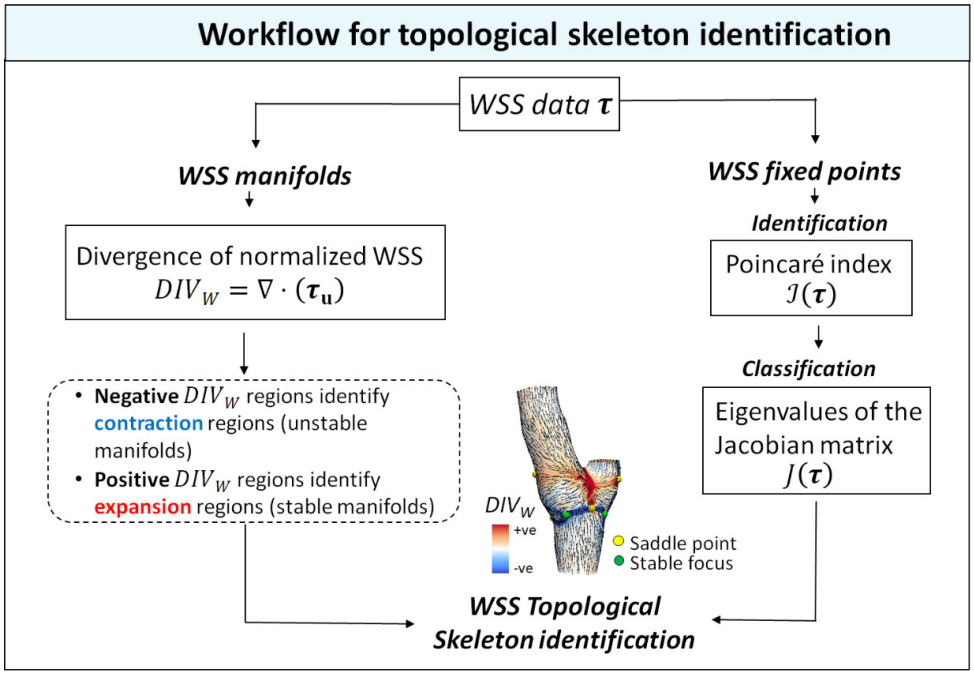

Figure 3.1: Workflow of the proposed Eulerian-based approach for the topological skeleton of the WSS vector identification.

in a 3D space is a constant tangent vector in each triangle element [84].
In detail, given a generic surface mesh triangle T_η ($\eta = 1, .., N$, where N is the number of mesh triangles), we consider a vertex-based representation of the WSS vector field $\boldsymbol{\tau}$ where $\boldsymbol{x}_\zeta \in \mathbb{R}^3$ is the location of the generic vertex ζ ($\zeta = i, j, k$). The first step of the algorithm is the discretization of the vector field through a piecewise constant vector per mesh triangle face representation.
To do that, the vector field components $(\tau_x)_\zeta, (\tau_y)_\zeta, (\tau_z)_\zeta$ defined on each vertex mesh in a Cartesian reference frame, are interpolated in a generic position inside mesh triangle T_η using barycentric coordinates using piecewise linear basis functions B_ζ:

$$\begin{aligned}
\tau_x(\mathbf{p}) &= (\tau_x)_i B_i(\mathbf{p}) + (\tau_x)_j B_j(\mathbf{p}) + (\tau_x)_k B_k(\mathbf{p}) \\
\tau_y(\mathbf{p}) &= (\tau_y)_i B_i(\mathbf{p}) + (\tau_y)_j B_j(\mathbf{p}) + (\tau_y)_k B_k(\mathbf{p}) \\
\tau_z(\mathbf{p}) &= (\tau_z)_i B_i(\mathbf{p}) + (\tau_z)_j B_j(\mathbf{p}) + (\tau_z)_k B_k(\mathbf{p}),
\end{aligned} \tag{3.1}$$

where $\mathbf{p} = (x, y, z) \subset T_\eta$. The basis functions B_ζ are of the form (Figure 3.2):

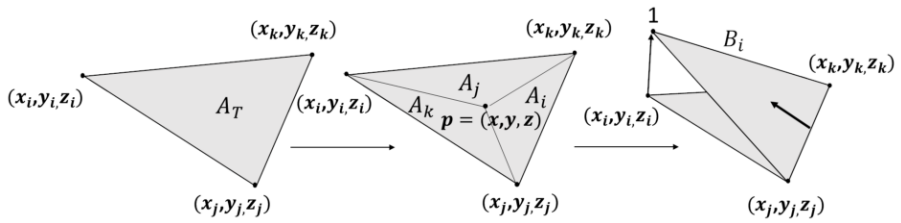

Figure 3.2: Piecewise linear basis function B_i

$$B_i(\mathbf{p}) = \frac{A_i}{A_T},\ B_j(\mathbf{p}) = \frac{A_j}{A_T},\ B_k(\mathbf{p}) = \frac{A_k}{A_T} \tag{3.2}$$

where, A_T is the surface area of triangle mesh T_η, and A_i,A_j,A_k are the surface areas of the triangles of coordinates$\{\mathbf{p}, \boldsymbol{x}_j, \boldsymbol{x}_k\}$, $\{\mathbf{p}, \boldsymbol{x}_i, \boldsymbol{x}_k\}$, $\{\mathbf{p}, \boldsymbol{x}_j, \boldsymbol{x}_j\}$, respectively (Figure 3.2). By construction (Figure 3.2),

$$B_i(\boldsymbol{x}_i) = B_j(\boldsymbol{x}_j) = B_k(\boldsymbol{x}_k) = 1 \ \text{ and } \ B_i(\boldsymbol{x}_{j,k}) = B_j(\boldsymbol{x}_{i,k}) = B_k(\boldsymbol{x}_{i,j}) = 0.$$

By differentiating the basis functions B_ζ, the gradient of τ_x in $\mathbf{p}$ can be expressed as:

$$\begin{aligned}
\nabla\tau_x(\mathbf{p}) &= (\tau_x)_i \nabla B_i(\mathbf{p}) + (\tau_x)_j \nabla B_j(\mathbf{p}) + (\tau_x)_k \nabla B_k(\mathbf{p}) \\
\nabla\tau_y(\mathbf{p}) &= (\tau_y)_i \nabla B_i(\mathbf{p}) + (\tau_y)_j \nabla B_j(\mathbf{p}) + (\tau_y)_k \nabla B_k(\mathbf{p}) \\
\nabla\tau_z(\mathbf{p}) &= (\tau_z)_i \nabla B_i(\mathbf{p}) + (\tau_z)_j \nabla B_j(\mathbf{p}) + (\tau_z)_k \nabla B_k(\mathbf{p}),
\end{aligned} \tag{3.3}$$

where $\nabla \mathrm{B}_\zeta(\mathbf{p})$ is the steepest ascent direction perpendicular to the opposite edge, expressed as:

$$\begin{aligned}
\nabla B_i(\mathbf{p}) &= \frac{\boldsymbol{n}_{T\eta} \times \mathbf{e}_{jk}}{2\ A_T} \\
\nabla B_j(\mathbf{p}) &= \frac{\boldsymbol{n}_{T\eta} \times \mathbf{e}_{ki}}{2\ A_T} \\
\nabla B_k(\mathbf{p}) &= \frac{\boldsymbol{n}_{T\eta} \times \mathbf{e}_{ij}}{2\ A_T},
\end{aligned} \tag{3.4}$$

where $\boldsymbol{n}_{T\eta}$ is the unit vector normal to the triangle surface T_η and $\mathbf{e}_{jk}$, $\mathbf{e}_{ki}$, $\mathbf{e}_{ij}$ denote the edges opposite to vertex i, j, k, respectively (Figure 3.2).
Combining eq. (3.3) and eq. (3.4), the divergence of WSS vector field in $\mathbf{p} \subset T_\eta$

can then be obtained:

$$\nabla \cdot \boldsymbol{\tau}\left(\mathbf{p}\right) = \nabla \tau_x\left(\mathbf{p}\right) \cdot \hat{\mathbf{x}} + \nabla \tau_y\left(\mathbf{p}\right) \cdot \hat{\mathbf{y}} + \nabla \tau_z\left(\mathbf{p}\right) \cdot \hat{\mathbf{z}}\ . \tag{3.5}$$

The value of $\nabla \cdot \boldsymbol{\tau}$ at each vertex ζ of the mesh triangle T_η is calculated as the average value of the WSS divergence over all triangles of the mesh the considered vertex ζ belongs to:

$$(\nabla \cdot \boldsymbol{\tau})_\zeta = \frac{\sum_{T_\chi \sim \zeta}\ (\nabla \cdot \boldsymbol{\tau})_{T_\chi \sim \zeta}}{\#T_\chi}, \tag{3.6}$$

where $\#T_\chi$ is the total number of surface mesh triangles the vertex ζ belongs to.

3.2 Wall Shear Stress fixed points identification and classification

Typically, computational data are available as discrete samples at the vertices of a mesh, and the direct application of the theory of dynamical system to sampled data could lead to consistency loss [85].
Here, identification of fixed points location on the luminal surface of a vessel is performed using the Poincarè index, as briefly introduced in Section 2.1. The relevance of this topological index lies in its mesh-independent and topologically invariant proprieties. As an explanatory definition that may help the better understanding of the mathematical concept, the Poincaré index for a $2D$ arbitrary vector is provided in eq. ((2.4)) (Section 2.1) and displayed in Figure 3.3.

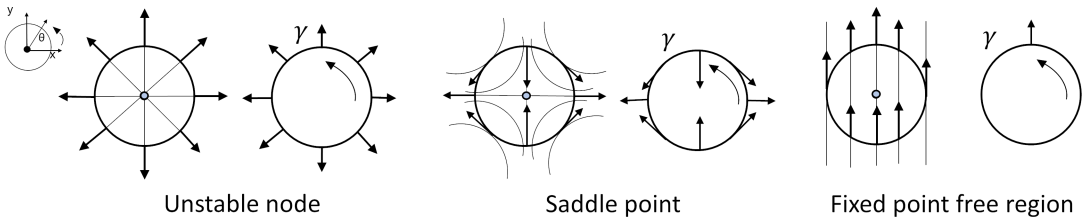

Figure 3.3: Unstable node, saddle point and fixed point free region configuration for a arbitrary 2D vector field. While travelling along the closed curve γ in positive direction, the Poincaré index is the number of the positive fields rotations.

Detection methods of isolated fixed points in analytical or 2D vector fields have

been already proposed by several authors [86]. Less work has been done on fixed points detection on vertex-based representations of 3D vector fields defined on unstructured triangle meshes representing the boundary of complex geometries (as blood vessels are). In the present study, the numerical method for fixed points detection proposed by Bhatia [85] and reworded by Wang [87] was implemented because of its demonstrated numerical robustness, which minimizes the risk of identification of incorrect topological structures due to numerical instabilities. The algorithm is based on the following theorem [87]:

Theorem 1. *Let* $\{\boldsymbol{x}_1, \boldsymbol{x}_2, \boldsymbol{x}_3\}$ *be the vertexes of a triangle of a triangulated surface with vectors* $\{\boldsymbol{\tau}_i, \boldsymbol{\tau}_j, \boldsymbol{\tau}_k\}$*, applied at the vertexes* i*,* j*,* k*, respectively, in a Cartesian three-dimensional reference system. There is a fixed point in the interior of the considered triangle if and only if the following determinants have all the same sign:*

$$det[\boldsymbol{\tau}_i, \boldsymbol{\tau}_j, \boldsymbol{n}],\ det[\boldsymbol{\tau}_j, \boldsymbol{\tau}_k, \boldsymbol{n}],\ det[\boldsymbol{\tau}_k, \boldsymbol{\tau}_i, \boldsymbol{n}] \tag{3.7}$$

where $\boldsymbol{n}$ *is the unit vector normal to the triangle face.*
Moreover, if a fixed point is located in the interior of the considered triangle, the Poincaré index is given by:

$$Sign(det[\boldsymbol{\tau}_i, \boldsymbol{\tau}_j, \boldsymbol{n}]). \tag{3.8}$$

Using Theorem 1, fixed points of a 3D vector field can be identified.

The fixed points identified by the Poincaré index are classified according to their nature, as briefly introduced in Section 2.1. The full classification of fixed points can be carried out using the largely adopted approach based on the analysis of the eigenvalues of the Jacobian matrix over each triangle face containing a fixed point [31]. The eigenvalues-based fixed point classification of a vector field is summarized in Table 2.1 in Section 2.1. In detail, three eigenvalues of the Jacobian matrix, with one of them having value close to zero, are obtained. Then, the eigenvalue-based analysis for the WSS fixed points classification can be performed by considering only the two eigenvalues different from zero.

An explanatory sketch of the complete topological skeleton of the WSS vector field at the luminal surface of an artery is presented in Figure 3.4

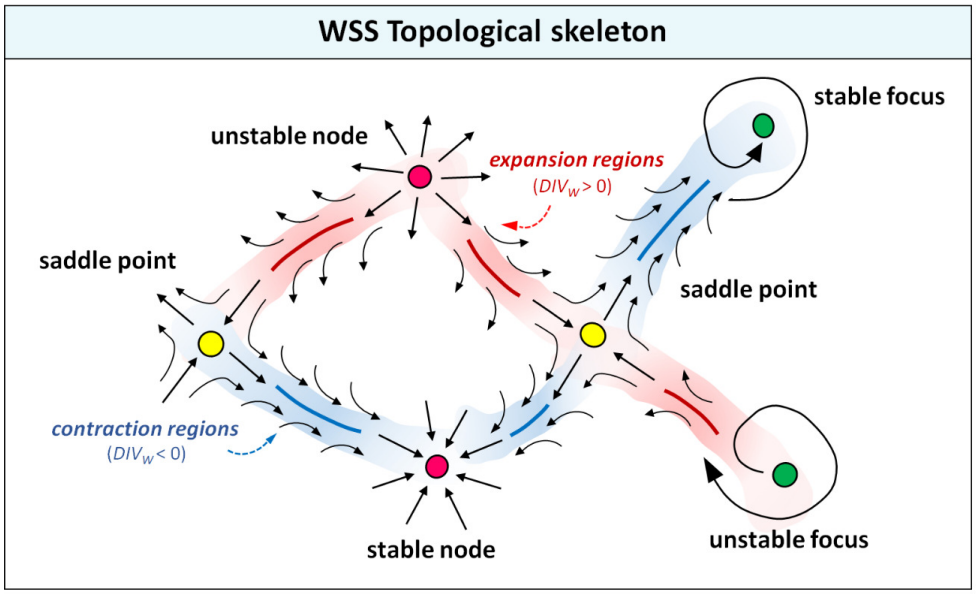

Figure 3.4: Explanatory sketch of the topological skeleton of a vector field. Configuration of each fixed point-type and contraction/expansion regions, colored by blue/red, are displayed.

3.3 Wall Shear Stress topological skeleton descriptors

The proposed practical approach for the identification and the analysis of manifolds and fixed points of the WSS vector field at the luminal surface of an artery is applied in a two-step strategy. In the first step, the cycle-average WSS vector field at the luminal surface of 3D vessels, defined in eq. (2.15), is analyzed. It has been already suggested that cycle-average WSS vector field $\bar{\boldsymbol{\tau}}$ fixed points and their associated manifolds influence the near-wall intravascular transport [23].
In the second step, the unsteady nature of WSS fixed points and manifolds along the cardiac cycle is analysed. To do that, a measure of instantaneous WSS fixed points residence times along the cardiac cycle is introduced. In detail, the fraction of cardiac cycle (General Residence Time, RT) spent by a specific fixed point of specific nature inside a generic surface triangle is calculated as follows:

$$RT_{x_{fp}}(e) = \frac{\bar{A}}{A_e}\frac{1}{T}\int_0^T \mathbb{I}_e(\boldsymbol{x}_{fp}, t), \tag{3.9}$$

where:

$$\mathbb{I}_e\left(\boldsymbol{x}_{fp}, t\right) = \begin{cases} 1 & \text{if} \quad \boldsymbol{x}_{fp}(t) \in e \\ 0 & \text{otherwise.} \end{cases}$$

In eq. (3.9) $\boldsymbol{x}_{fp}\left(t\right)$ is the WSS fixed point position at time $t \in [0, T]$, e is the generic triangular element of the superficial mesh of area A_e and $\bar{A}$ is the average surface area of all surface triangles of the mesh characterizing the luminal surface of the vessel. Eq. (3.9) quantifies the fraction of cardiac cycle spent by a WSS fixed point inside the generic mesh surface element e.

Moreover, a modified version of eq. (3.9) is proposed, where the residence time of a fixed point in a triangular mesh surface element is weighted by the absolute value of the instantaneous WSS vector divergence. Physically, this Weighted Residence Time ($RT\nabla_{x_{fp}}\left(e\right)$) gives a measure of the strength of the local contraction/expansion action of local shear forces:

$$RT\nabla_{x_{fp}}\left(e\right) = \frac{\bar{A}}{A_e}\frac{1}{T}\int_0^T \mathbb{I}_e\left(\mathbf{x}_{fp}, t\right)|(\nabla \cdot \boldsymbol{\tau})_e|dt, \tag{3.10}$$

where $(\nabla \cdot \boldsymbol{tau})_e$ is the instantaneous WSS divergence computed in the surface triangle e containing the instantaneous WSS fixed point.

The difference between $RT_{x_{fp}}(e)$ and $RT\nabla_{x_{fp}}\left(e\right)$ resides in the term $|(\nabla \cdot \boldsymbol{\tau})_e|$, that has been incorporate into eq. (3.10) to measure the contraction/expansion strength acting on the wall. Roughly speaking, with respect to eq. (3.9), in eq. (3.10) the contribution of those fixed points surrounded by a marked local contraction or expansion action, even for a small fraction of the cardiac cycle, is emphasized.

Finally, a measure to compute the fraction of the cardiac cycle (Specific Residence Time, $RT_{x_{fp}}\left(e_{\bar{\tau}_{fp}}\right)$) that the surface triangle containing a cycle-average WSS fixed point hosts an instantaneous WSS fixed point is here presented:

$$RT_{x_{fp}}\left(e_{\bar{\tau}_{fp}}\right) = \frac{\bar{A}}{A_e}\frac{1}{T}\int_0^T \mathbb{I}_{e_{\bar{\tau}_{fp}}}\left(\boldsymbol{x}_{fp}, t\right)dt, \tag{3.11}$$

where $e_{\bar{\tau}_{fp}}$ is the specific surface triangle of the superficial mesh containing a cycle-average WSS fixed point.

The proposed WSS fixed points residence time measures, namely the General Residence Time (eq. (3.9)), the Weighted Residence Time (eq. (3.10)) and the specific residence time (eq. (3.11)) are summarized in Figure 3.5.

In addition, based on the physical meaning of eq. 2.22, we proposed the quantity Topological Shear Variation Index ($TSVI$) aiming at quantifying the amount of variation in the WSS contraction and expansion action exerted on the endothelium along the cardiac cycle. The $TSVI$ index is defined as the root mean square deviation of the divergence of the normalized WSS with respect to its average over the cardiac cycle:

$$TSVI = \{\frac{1}{T}\int_0^T [\nabla \cdot (\boldsymbol{\tau}_u) - \overline{\nabla \cdot (\boldsymbol{\tau}_u)}]^2\}^{\frac{1}{2}} = \{\frac{1}{T}\int_0^T [DIV_W - \overline{DIV_W})]^2\}^{\frac{1}{2}}, \quad (3.12)$$

where T is the cardiac cycle period. It is an integral measure of the local unsteady nature of the WSS vector field manifolds along the cardiac cycle, without differentiating between a contraction or expansion action of WSS at the endothelium.

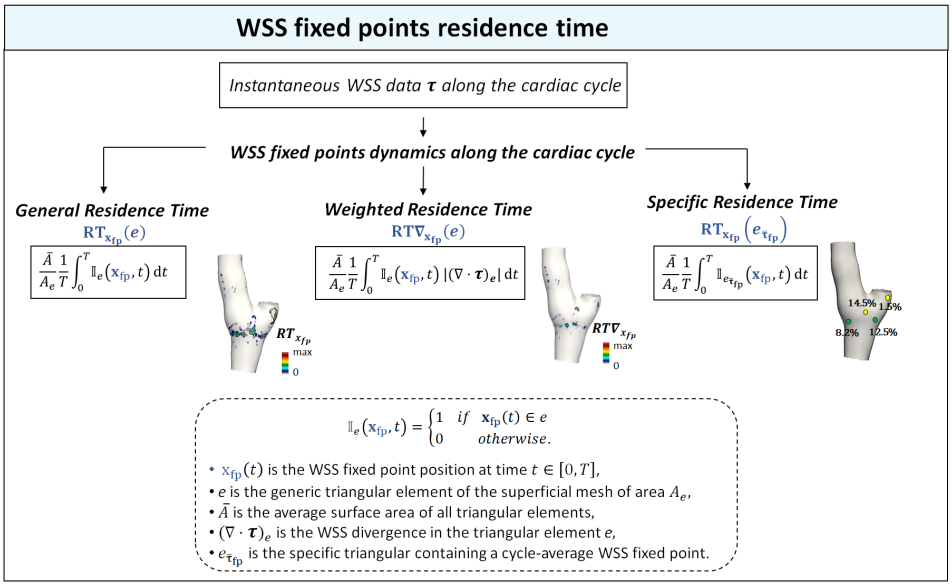

Figure 3.5: Three different formulations, namely General Residence Time, Weighted Residence Time and Specific Residence Time to quantified the WSS fixed points residence times along the cardiac cycle.

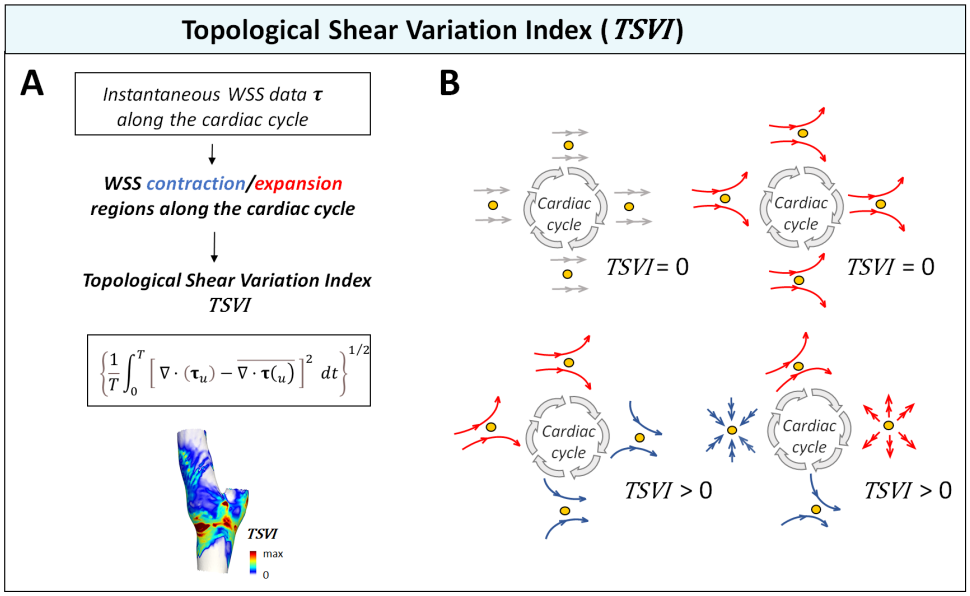

Figure 3.6: A) Definition of $TSVI$ index; B) Blue, red and grey arrows indicate the WSS vector field instantaneous streamlines in the neighbourhood of the generic point (yellow circle) on the luminal surface at different time points along the cardiac cycle.

Chapter 4

Benchmarking

4.1 2D analytical vector field

An analytical 2D vector field, described by the following autonomous system:

$$\begin{cases} \dot{x} = x - \frac{x^3}{3} - y \\ \dot{y} = x - 2y, \end{cases} \tag{4.1}$$

is used here for benchmarking and testing the proposed method.
The analytical 2D vector field described by eq. (4.1) is characterized by the presence of a saddle point configuration in the origin of the cartesian reference system, and two symmetrical stable foci at cartesian coordinates $\left(\pm 2\sqrt{\frac{3}{8}}; \pm\sqrt{\frac{3}{8}}\right)$.
To trace out the unstable manifold, the classical method was applied considering perturbed coordinates of the saddle point as initial condition [31, 22]. The numerical integration was carried out by applying the *Runge Kutta Fehlberg* $4-5$ numerical scheme and integration was continued until the trajectory reached the other fixed point. On the same vector field (1) the divergence of normalized vector field was computed to identify contraction/expansion regions and (2) the Poincaré index was used to identify fixed points. For an in-depth benchmarking, the recent trajectory-free method proposed by [88] was here applied on the autonomous system of eq. (4.1) to find attracting and repelling invariant manifolds using the trajectory divergence rate $\dot{\rho}$ defined by:

$$\dot{\rho} = \boldsymbol{n}^T \mathbf{S}\, \boldsymbol{n}, \tag{4.2}$$

where $\boldsymbol{n}$ is the unit vector normal and S the rate-of-strain tensor.
The autonomous system of eq. (4.1) is presented in Figure 4.1, where the position of the three fixed points is highlighted and the unstable manifold (corresponding to a saddle-type fixed point and calculated according to [31, 22]), is delineated. It can be observed that the map of the divergence of the normalized vector field perfectly encases the unstable manifold within the contraction region (blue color in Figure 4.1, panel B) according to theory: regions of negative divergence correspond to converging vectors and unstable manifolds tend to attract nearby trajectories (the distance between points belonging to unstable manifolds decreases producing a converging point series).
Finally, the results obtained implementing the trajectory-free method proposed elsewhere [88] on the autonomous system of eq. (4.1), reported in Figure 4.1 panel C, clearly show that the divergence of normalized vector map captured the unstable manifold of the system as well as the trajectory divergence rate $\dot{\rho}$. Notably, although both the divergence-based methods provide a scalar measure to quantify the attraction/repulsion of nearby trajectories, the here proposed divergence of the normalized vector field captured the unstable manifold only, as opposed to the trajectory divergence rate $\dot{\rho}$, that highlighted also regions of the phase space that are not an unstable manifold (Figure 4.1, panel C).
The results of the application of the approach proposed here to practically identify manifolds and fixed points to the autonomous system of eq. (4.1) confirm that the method is able to: (1) correctly approximate manifolds without resorting to the numerical integration schemes; (2) correctly identify and classify fixed points (Figure Figure 4.1), confirming the numerical robustness of the Poincaré Index.

4.2 3D complex geometries

A further analysis aiming at testing the ability of the proposed Eulerian-based approach to correctly identify (1) Lagrangian WSS structures and (2) WSS manifolds is performed on a 3D complex geometry of a carotid bifurcation model. Details on geometry reconstruction, meshing and CFD simulation where extensively reported in Section 6.2.1, Section 7.2.2 and elsewhere [89, 90, 19]. WSS LCS are identified by numerically integrating high number ($\approx$ 300 000) of luminal surface tracer particles (depicted in Figure 4.2A) seeded on the luminal surface of the carotid bifurcation model based on the near-wall blood flow velocity, as described

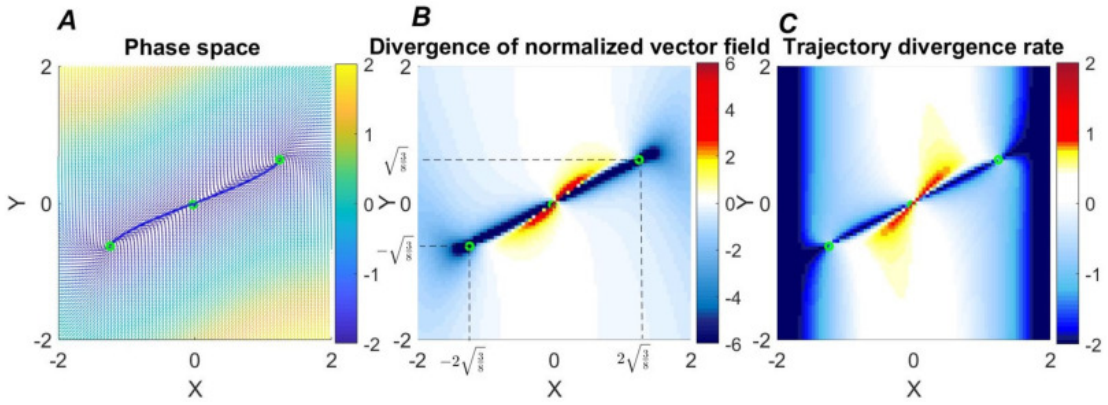

Figure 4.1: Panel A: Fixed points (green circles) and attractive manifold (blue line). Vector field is normalized for visualization and colored based on its magnitude. Panel B: Divergence of the normalized vector field. Panel C: Trajectory divergence rate field

in Section 2.2.3. In particular, attracting WSS LCS are traced out with forward time integration of surface tracer particles for 40 cardiac cycle, exploiting the periodicity of WSS vector field, used to compute the blood flow velocity near the wall. Emerging attracting WSS LCS, displayed in Figure 4.2A LCS is located at the carotid bulb, a region characterized by flow disturbances. On the same carotid bifurcation model, unstable manifolds of the cycle-average WSS vector field are traced out by applying the classical method consisting in the integration in forward time of the vector field, starting from perturbed coordinated of saddle point positions and in the directions of the positive eigenvectors. Finally, on the same carotid bifurcation model, cycle-average WSS contraction regions are identified by negative values of the normalized cycle-averag WSS divergence (depicted in Figure 4.2C), according to the proposed method. For the present analyses, *Runge Kutta 4-5* numerical integration scheme was used to be consistent with previous studies [46].

Figure 4.3 shows the cycle-average WSS contraction regions at the luminal surface of the carotid bifurcation model, superimposed on the attracting WSS LCS (4.3A) and on cycle-average WSS unstable manifolds (4.3B).
By visual inspection of Figure 4.3, it can be appreciated that cycle-average WSS contraction regions co-localize with attracting WSS LCS and with cycle-average WSS unstable manifolds, confirming the ability of the Eulerian-based approach to identify Lagrangian structures.

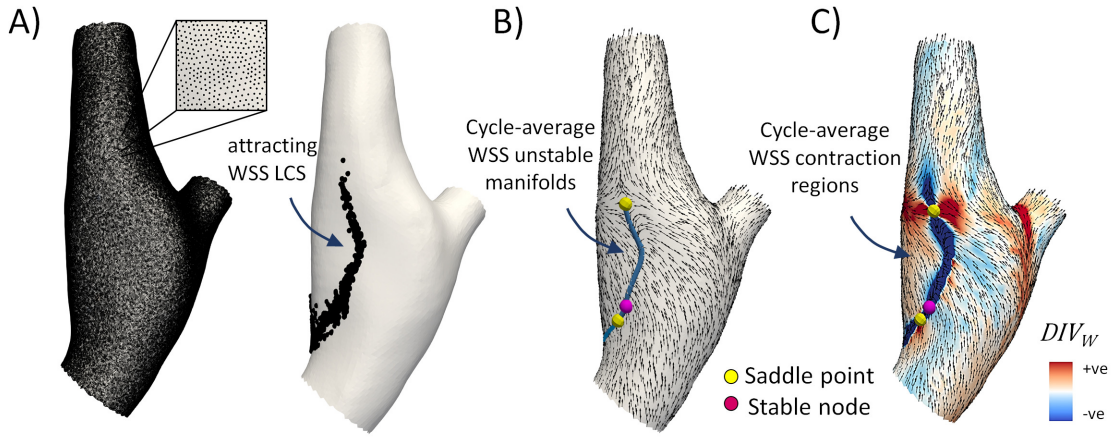

Figure 4.2: A) Initial tracers position on the luminal surface of a carotid bifurcation model and the emerging attracting WSS LCS traced out from forward time integration of surface tracers. B) Unstable manifolds (blue lines) and fixed points of cycle-average WSS traced out by integrating cycle-average WSS vector starting from saddle point positions. C) Topological skeleton of the cycle-average WSS vector. Blue and red color define contraction and expansion regions, respectively.

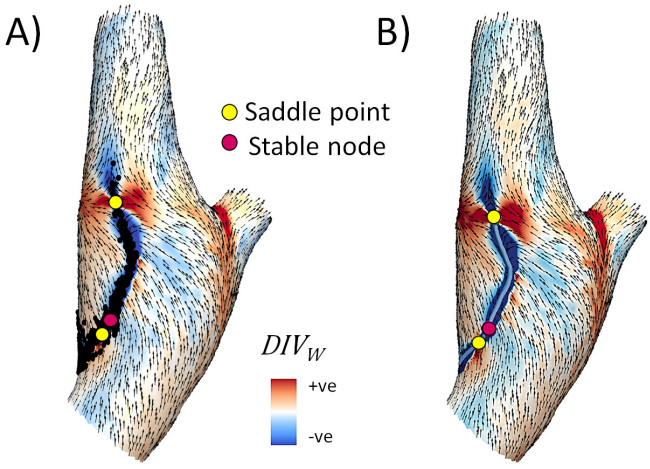

Figure 4.3: A) Qualitatively co-localization between cycle-average WSS divergence-based contraction regions and attracting WSS LCS. B) Qualitatively co-localization between cycle-average WSS divergence-based contraction regions and cycle-average WSS unstable manifolds WSS LCS.

Chapter 5

Wall Shear Stress Divergence as a Template of Near-Wall Mass Transport in Aortic Flow

A version of this chapter has been published in:
Pàtron Editor, Congress of the National Group of Bioengineering 2020, ISSN: 2724-2129
"Eulerian-based Wall Shear Stress Topological Skeleton Analysis and Near-wall Transport in Aortic Flow."
G. De Nisco, V. Mazzi, K. Calò, R. Ponzini, G. Rizzo, D. A. Steinman, D. Gallo, U. Morbiducci

5.1 Introduction

Mass transport plays a key role in vascular disease. In the past, it has been suggested that the accumulation of high molecular weight solutes in the arterial intima might promote early atherosclerosis [74], and observations have reported that high plasma levels of low-density lipoproteins (LDL) are causally related to the development of atherosclerotic lesions [91]. Among the complex and non-linear mechanisms regulating blood-arterial wall mass transfer [26, 92], the shear forces exerted by the streaming blood on endothelial cells (ECs) have been identified to play a key role, because of their influence on the permeability of the endothelial lining [11]. The complexity of the scenario has markedly limited in vivo studies on the biomechanical role exerted by the wall shear stress (WSS) on blood arterial

wall mass transfer. Aiming at filling this gap of knowledge, in the last decade, computational fluid dynamics (CFD) has been proposed to study the impact that local hemodynamics has on LDL transport and on their blood-to-wall transfer in realistic models of human aorta [93, 94, 95], a cardiovascular district characterized by intricate local hemodynamics [61]. These studies have demonstrated that regions at the luminal surface where LDL concentration is high in general co localize with low shear regions.

However, cardiovascular mass transport problems are characterized by high Peclet number (≈108 for LDL), indicating the relative predominance of advective vs. diffusive transport. Therefore, highly resolved computational grids are needed to accurately solve the near-wall transport and blood-wall transfer [80]]. Due to that, high computational costs are usually associated with this class of numerical simulations [81].

To overcome this limitation, a marked interest has recently emerged on using WSS Lagrangian Coherent Structures (WSS LCS) to study mass transport in cardiovascular flows. In detail, WSS LCS have been brilliantly proposed to provide a template for near-wall transport, with reduced computational costs compared to a full transport problem [23, 22]. In addition, previous studies have proved the capability of the LCS in identifying WSS topological skeleton features, i.e., WSS manifolds, which in turn have been demonstrated to be connected with near-wall mass transport [23, 22].

Here we briefly remind that the WSS topological skeleton consists in fixed points and stable/unstable manifolds connecting them. In detail, a fixed point is a point where the WSS vector field vanishes, and the WSS manifolds identify the strength and the nature of the WSS contraction/expansion imparted on the endothelium.

This study is based on the considerations that the use of LCS might have some practical limitations, namely the poor control over the flow region of interest and the application of higher-order integration schemes [96]. The aim of the present study is to test the ability of the proposed Eulerian method for WSS topological skeleton analysis based on WSS vector field divergence to provide an affordable template of the LDL blood-wall transfer in patient-specific computational hemodynamic models of human aorta. Such endeavour would identify a methodology faster and less computationally expensive than both Lagrangian-based techniques and full 3D continuum problems to solve mass transport in cardiovascular flows.

5.2 Computational haemodynamics

An overview of the study methods is provided in Figure 5.1.

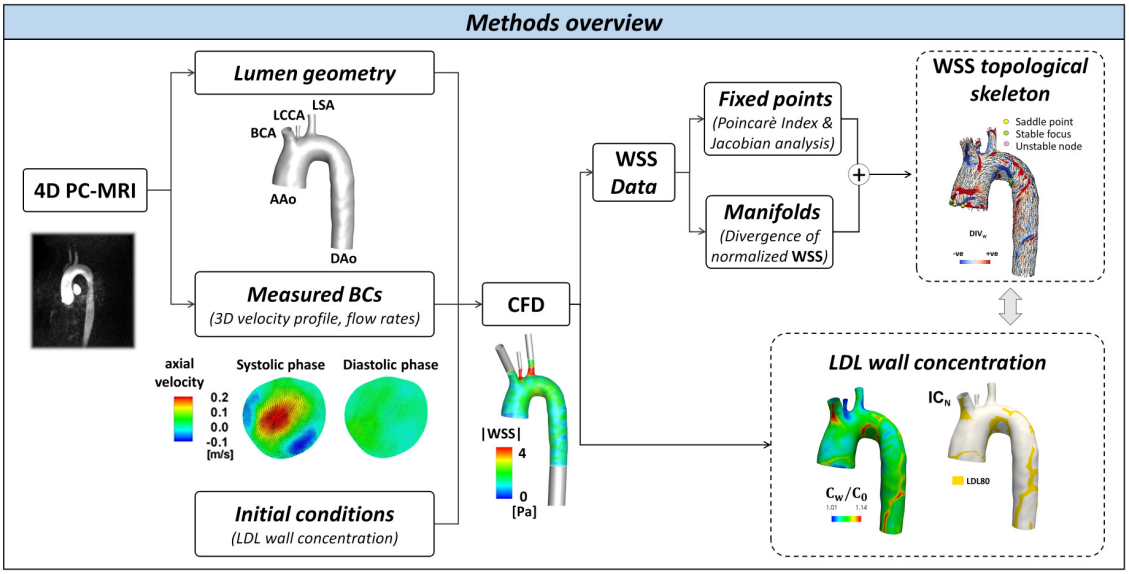

Figure 5.1: Overview of the proposed approach to study near-wall LDL transport and WSS topological skeleton. Explanatory examples of contours of the 4D flow MRI-derived axial velocity component, applied as inflow BCs, averaged along systole and diastole are also displayed.

The geometry of an ostensibly healthy human aorta was reconstructed from 4D flow MRI images, by applying a multiple step procedure into the Vascular Modeling Toolkit environment (VMTK). MRI image acquisition and aortic geometry reconstruction are extensively described elsewhere [60, 97, 98].
To model LDL transport in the streaming blood, the governing equations of fluid motion (the Navier-Stokes equations) were coupled with the advection-diffusion equation under unsteady flow conditions. In detail, LDL was modelled as a passive non-reacting scalar, transported in the flowing blood according to the advection-diffusion equation:

$$\frac{dC}{dt} + \mathbf{u} \cdot \nabla C - D_{LDL} \nabla^2 C = 0 \tag{5.1}$$

where C is the LDL concentration, $\mathbf{u}$ is the velocity vector, and D_{LDL} is the diffusivity of LDL in blood, set to $5.98 \cdot 10^{-12}\ m^2 s^{-1}$. Blood was assumed to be an isotropic, incompressible, homogeneous, Newtonian viscous fluid with density

equal to 1060 kg/m3 and dynamic viscosity equal to 0.0035 Pa s. The finite volume method was applied to solve the coupled Navier-Stokes and advection-diffusion equations in their discretized form. The general purpose CFD code Fluent (ANSYS Inc., USA) was used on a computational mesh-grid with 30 layers of high-quality prismatic cells near the wall and structured tetrahedral elements in the lumen region [81]. The instantaneous measured (with 4D flow MRI) 3D velocity profiles were prescribed as inflow boundary condition (BC) at the ascending aorta (AAo) inlet section (Figure 5.1) [98]. The strategy applied at the outflow boundaries is the same as in previous studies [98]. Briefly, at the outflow sections of the supra-aortic vessels (BCA - brachiocephalic artery; LCCA - left common carotid artery; LSA - left subclavian artery) and of the descending aorta (DAo) measured flow rate ratios were imposed as BCs. Arterial walls were assumed to be rigid with no-slip condition at the wall.

To solve the governing equation of mass transport (Eq. (5.1)) a constant LDL concentration C_0 equal to $2.86 \cdot 10^{-9}\, mol/m^3$ (corresponding to the physiological LDL concentration in whole blood) [99] was prescribed at the inlet section, and the stress free condition was applied at each outlet. To be consistent with previous studies [81, 23, 22], the LDL blood-to-wall transfer was modelled by prescribing Eq. (5.2) at the luminal surface [81]:

$$C_W v_W - D_{LDL} \frac{dC}{dn}|_W = 0 \tag{5.2}$$

where C_W is the LDL concentration at the vessel wall, v_W the water filtration velocity through the wall, $\frac{dC}{dn}$ is the concentration gradient normal to the wall.

To be consistent with previous studies using WSS LCS to identify mass transfer to the arterial wall [23, 22] a null LDL concentration was applied as initial condition to the whole domain (with the exception of the inflow section, as detailed before). Details on the applied numerical schemes and convergence criteria are extensively provided elsewhere [81].

5.3 WSS topological skeleton and Co-localization analysis

The proposed Eulerian method to identify and analyse the topological skeleton of the WSS vector field was considered. Briefly, the divergence of the WSS vector field allows to encase the connections between WSS fixed points, i.e., the WSS manifolds.

Consequently, the divergence of the normalized WSS vector field was here computed according to eq. (2.22). In detail, negative values of DIV_W identify contraction regions, approximating the unstable manifolds, while positive DIV_W values identify expansion regions, approximating the stable manifolds, on the luminal surface of a vessel.

To complete the WSS topological skeleton analysis, the Poincaré index was considered to identify WSS fixed points on the luminal surface. Once identified, the Jacobian analysis was carried out to classify fixed points, distinguishing between an attractive or repelling nature of fixed points. Poincaré index values and eigenvalues of the Jacobian matrix for each fixed point-type are summarized in Table 2.1.

The Eulerian-based WSS topological skeleton analysis was here applied to the cycle-average WSS vector field $\bar{\boldsymbol{\tau}}(\boldsymbol{x})$ at the aortic luminal surface, according to eq. (2.15).

The analysis of the extent of the co-localization between luminal WSS contraction/expansion regions and local LDL uptake was carried out according to schemes proposed elsewhere [81, 20]. In detail, an objective threshold for the normalized LDL concentration at the aortic luminal surface (C_W/C_0) was identified as the 80^{th} percentile value of (C_W/C_0) distribution. The surface area (SA) exposed to normalized LDL concentration values higher than the defined threshold was then quantified and denoted as LDL80.

As for WSS topology, luminal contraction regions were identified by determining the 20^{th} percentile value of normalized WSS divergence and computing the SA exposed to DIV_W values lower than this threshold. The latter area was denoted as DIV20. No threshold was set for identifying the luminal expansion regions, because no co-localization was observed with high LDL uptake regions, by visual inspection.

5.4 Results

A qualitative comparison between normalized LDL wall distribution at the luminal surface and cycle-average WSS topological skeleton is provided in Figure 5.2 (panel A and B, respectively).
WSS contraction regions are coloured by blue, while WSS expansion regions are presented in red colour.
Interestingly, it can be observed that only one unstable node of cycle-average WSS vector is identified at the luminal surface of the investigating thoracic aorta. The unstable fixed point, repelling near-wall trajectories, is located at a point at the ascending aorta luminal surface characterized by a low value of LDL concentration. Contrarily, all the stable fixed points of cycle-average WSS vector are located in luminal regions where the normalized LDL concentration assumes high values ($>$ 15%, Figure 5.2).
As for WSS manifolds, a marked co-localization between high LDL luminal concentration and WSS contraction regions clearly emerges from Figure 5.2: the regions at the luminal surface where the divergence of the normalised WSS vector is negative are characterized by LDL concentration polarization. This is particularly evident in three main regions along the aortic wall, i.e., the inner part of the BCA, the intrados of the aortic arch and the DAo segment.
A direct co-localization analysis between LDL concentration polarization and WSS contraction regions at the aortic luminal surface is provided in Figure 5.3, where LDL80 (yellow-coloured regions) and DIV20 (blue contour lines) luminal SAs are displayed. The figure shows a marked spatial overlap between LDL80 and DIV20, with the contour lines of DIV20 mostly encasing luminal regions with high LDL concentration. Their co-occurrence is less evident only locally at the AAo and at the proximal DAo.
The latter results suggest that WSS contraction regions lead to high LDL uptake in their surroundings, in accordance to previous findings linking the WSS topological skeleton to near-wall mass transport using a Lagrangian approach [23]. The maps in Figures 5.2 and 5.3 prove the ability of the Eulerian-based WSS topological skeleton analysis to provide an affordable template of the LDL concentration polarization at the luminal surface of the aorta.

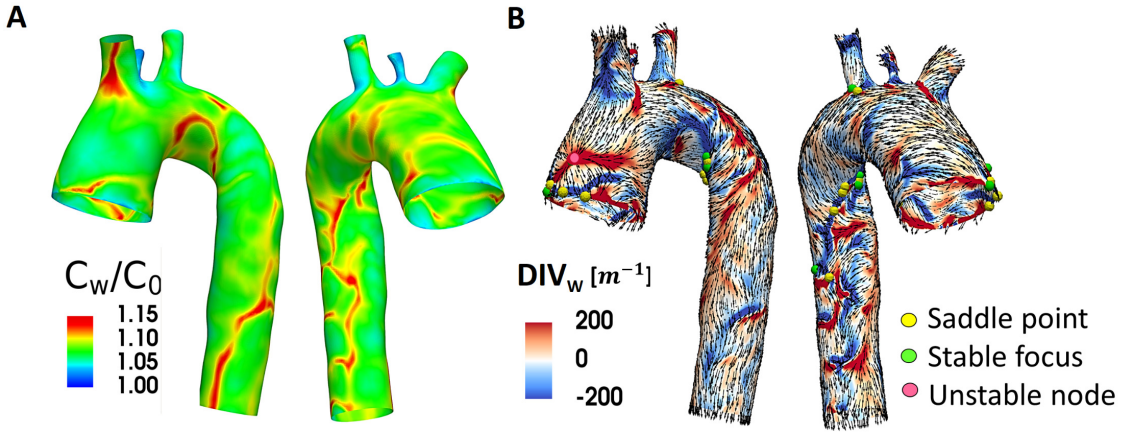

Figure 5.2: A: LDL wall concentration. B:Cycle-average WSS topological skeleton. Blue and red color define the contraction and expansion regions, respectively. Vector field is normalized for visualization LDL wall concentration (two different views).

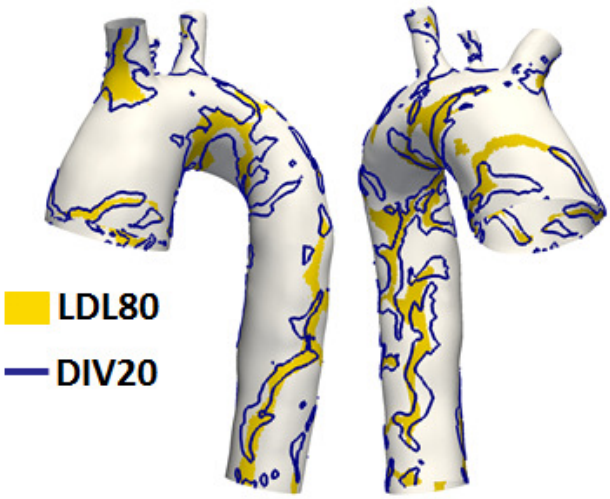

Figure 5.3: Distribution of LDL80 (yellow-coloured regions) and DIV20 (blue contour lines) luminal SAs (two different views).

5.5 Discussion

Recent studies [23, 22] have demonstrated that WSS LCS can be used as a template of near-wall mass transport, allowing to reduce the computational effort needed to solve the full transport problem. In particular, it has been demonstrated that attracting WSS LCS attract biochemicals, leading to high near-wall concentration in their neighbourhood, whereas repelling WSS LCS have been shown to

act as near-wall transport barriers.
In this study the here proposed Eulerian-based method is applied to compute WSS topological skeleton in a patient-specific computational model of human aorta, and its ability to properly describe LDL wall transfer is tested.
This study demonstrates that the proposed Eulerian-based method to identify WSS topological skeleton efficiently provides a template of the LDL blood-to-wall transfer. The methodology, requiring less computational efforts with respect to a fully 3D simulation of mass transport in cardiovascular flows, as well as less computational efforts than LCS-based strategies, candidates as an effective tool enriching the analysis of cardiovascular flows with relatively low computational effort [81].
The plausibility of the here reported findings finds a physical explanation in the theory of dynamical systems [39], affirming that near-wall trajectories are attracted by WSS contraction regions and they accumulate around these structures, thus producing high surface concentration.
In addition, recent studies have demonstrated the marked impact of the prescribed LDL concentration initial conditions on the results of mass transport simulations [81]. Moving from this consideration, future studies investigating the effects of the imposed LDL initial conditions on the relation between WSS topological skeleton and LDL transfer are warranted and encouraged.

Chapter 6

Analysis of the Unsteady Nature of Wall Shear Stress Topological Skeleton Features

A version of this chapter has been published in:
Biomechanics and Modeling in Mechanobiology; 19:1403-1423. doi: 10.1007/s10237-019-01278-3, 2020
"A Eulerian method to Analyze Wall Shear Stress Fixed Points and Manifolds in Cardiovascular Flows"
V. Mazzi, D. Gallo, K. Calò, M. Najafi, M. O. Khan, G. De Nisco, D. A. Steinman, U. Morbiducci

6.1 Introduction

A marked interest recently emerged on WSS fixed points and the stable and unstable manifolds that connect them [23, 21], forming the topological skeleton of the WSS vector field. Previous studies mostly focused on the cycle-average WSS topological skeleton [22, 100], highlighting that the cycle-average WSS topological skeleton is strongly linked to arterial near-wall mass transport and could explain luminal surface concentration patterns of, e.g., low density lipoprotein or oxygen [22, 100], which are involved in the atherosclerosis initiation processes. However, WSS fixed points patterns is markedly instantaneous by nature, with fixed points

appearing, moving, disappearing and changing their nature at predisposed locations at the luminal surface of a vessel, along the cardiac cycle. In light of this, a practical method for an in-depth analysis of the instantaneous WSS fixed points along the cardiac cycle is needed. The proposed Eulerian-based practical method can be easily adopted to focus on WSS topological skeleton analysis along the cardiac cycle. An in-depth analysis of the time dependence of the WSS topological skeleton along the cardiac cycle is provided, enriching the information obtained from cycle-average WSS. The proposed methods are applied here to personalized computational hemodynamic models of one carotid bifurcation and one intracranial aneurysm to explore their potential usefulness on cardiovascular districts characterized by distinguishable "disturbed" flow features.

6.2 Methods

6.2.1 Computational hemodynamics

The vascular geometries considered here are part of two broader studies. In detail, one carotid bifurcation model from the Vascular Aging-The Link That Bridges Age to Atherosclerosis (The VALIDATE Study) [19] and one intracranial aneurysm model from the Toronto Western Hospital aneurysm clinic were considered.
Carotid bifurcation geometry and inlet/outlet flow boundary conditions were extracted from contrast-enhanced angiography and phase-contrast MRI, respectively. Details on geometry reconstruction, meshing and CFD simulation where extensively reported elsewhere [89, 90, 19]. Briefly, the lumen geometry was reconstructed from its brachiocephalic origin to well above the bifurcation using the open-source Vascular Modelling Toolkit (VMTK, www.vmtk.org). A quadratic tetrahedral mesh of cardinality 1160048 was generated using ANSYS ICEM-CFD software and pulsatile, patient-specific flow waveforms were imposed as boundary conditions at the CCA inlet and ICA outlet sections. Computational fluid dynamics simulation was carried out using a finite element-based in-house solver [101] and using up to 4800 time steps per cardiac cycle. As regards intracranial aneurysm model, details regarding geometry reconstruction, meshing strategy and CFD settings were presented elsewhere [102]. In particular, VMTK software was used to generate a tetrahedral mesh of cardinality 3315791. Simulation was performed using a minimally-dissipative solver developed within the open-source finite-element-method library FEniCS [103] and

using up to 10000 time steps per cardiac cycle. A fully developed Womersley velocity profile was applied at the inlet, and outflow division was based on a splitting method presented elsewhere [102].
The considered intracranial aneurysm model was characterized by the presence of cycle-invariant flow instabilities [104].

6.2.2 WSS topological skeleton

The WSS topological skeleton analysis was carried out applying the proposed Eulerian-based method, following the scheme summarized in Figure 3.1.
First, the WSS topological skeleton of the cycle-average WSS vector field $\bar{\boldsymbol{\tau}}$ (eq. (2.15)) at the luminal surface was analysed. Subsequently, the unsteady nature of the WSS fixed points along the cardiac cycle was characterized using the WSS fixed point residence time measures, namely the General Residence Time RT defined in eq. (3.9), the Weighted Residence Time ($RT\nabla_{x_{fp}}(e)$), defined in eq. (3.10) and the Specific Residence Time $RT_{x_{fp}}\left(e_{\bar{\tau}_{fp}}\right)$, defined in eq. (3.11).

6.3 The physiological significance of the cycle-average Wall Shear Stress vector fixed points

It has been already suggested that cycle-average WSS vector field $\bar{\boldsymbol{\tau}}$ fixed points and their associated manifolds influence the near-wall intravascular transport [23]. However, a cycle-average WSS vector field ($\bar{\boldsymbol{\tau}}$) fixed point would have never been a null vector along the cardiac cycle, i.e., it would have never been a real fixed point. This is also confirmed by the explanatory example in Figure 6.1, where it is shown that the fact that $\bar{\boldsymbol{\tau}} = 0$ at a point at the luminal surface of the vessel does not necessarily implies that at the same point the TAWSS, i.e., the cycle average value of the magnitude of vector $\boldsymbol{\tau}(t, \boldsymbol{x})$, is null. In fact, from the Integral Inequality Absolute Value it follows that:

$$|\bar{\boldsymbol{\tau}}(\boldsymbol{x})| = |\frac{1}{T}\int_0^T \boldsymbol{\tau}(t, \boldsymbol{x})dt| \leqslant \frac{1}{T}\int_0^T |\boldsymbol{\tau}(t, \boldsymbol{x})|dt = \text{TAWSS}(\boldsymbol{x}), \tag{6.1}$$

suggesting that a null value for $|\bar{\boldsymbol{\tau}}|$ does not necessarily imply the same for TAWSS. Moreover, it can be easily demonstrated that:

$$\mathrm{TAWSS}(\boldsymbol{x}) = 0 \;\leftrightarrow\; |\boldsymbol{\tau}\,(t, \boldsymbol{x})| = 0 \;\forall t \in [0, T]\,, \tag{6.2}$$

since $|\boldsymbol{\tau}\,(t, \boldsymbol{x})|$ is a non-negative function $\forall t \in [0, T]$. Eqns (6.1) and (6.2) call into question the real physical meaning of fixed points of the cycle-average WSS vector field at the luminal surface. In particular, eq. (6.2) clearly states that a fixed point of the cycle-average WSS vector field at a specific location at the luminal surface is a real fixed point if and only if the WSS vector at that location is always a fixed point (i.e., is always a null vector), along the cardiac cycle. The intricate near-wall and intravascular hemodynamics establishing in most healthy and diseased vessels make this a rarely satisfied condition in the arterial system. Notably, in the presence of a real, physically meaningful fixed point of the cycle-average WSS vector field as the one identified by the condition of eq. (6.2), the definition of other WSS-based descriptors measuring WSS directionality (see 1.1) such as the Oscillatory Shear Index (OSI) [105], and the transverse Wall Shear Stress (transWSS) [16] become meaningless.
This result has stimulated a more detailed investigation, focused on the time dependence of WSS fixed points and manifolds location and nature along the cardiac cycle.

6.4 Results

6.4.1 Cycle-average Wall Shear Stress topological skeleton analysis

In this section the results obtained applying the proposed Eulerian-based approach to realistic vascular models are presented, and cycle-average WSS topological skeleton is analyzed.
The normalized WSS vector maps, emphasizing the structure of the vector field, allows for a clear interpretation of the results, confirming that fixed points are properly identified at the luminal surface of the carotid bifurcation (Figure 6.2) and of the intracranial aneurysm (Figure 6.3). As for the carotid bifurcation model, four saddle-type cycle-average WSS fixed points and three stable foci are identified on

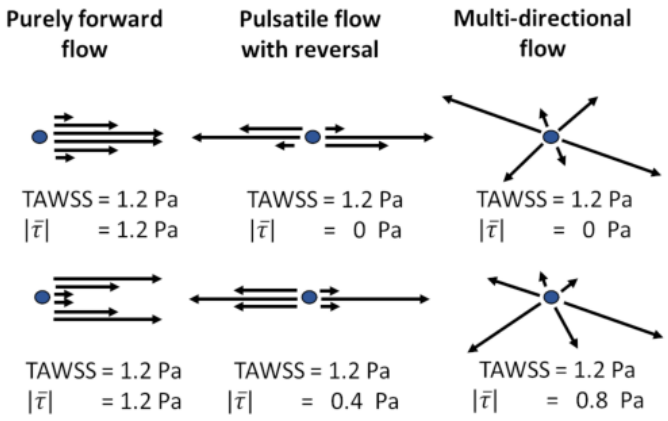

Figure 6.1: Comparison between $|\bar{\boldsymbol{\tau}}|$ and TAWSS in three different flow environments at the luminal surface of an artery. The black arrows depict WSS vectors at various times along cardiac cycle.

the luminal surface, all located at the carotid bulb. In particular, two saddle points are identified on the carotid sinus (Figure 6.2), one (A_C) at the outer wall of the proximal internal carotid artery (ICA), and one (D_C) at the proximal external carotid artery (ECA). The other two saddle points (C_C, E_C) and the stable foci (B_C, F_C, G_C) are identified immediately upstream of the maximum cross-sectional expansion of the carotid bulb (Figure 6.2). All the identified fixed points locations of the cycle-average WSS vector field belong to the bifurcation region characterized by slow, recirculating and disturbed flow that, based on the so-called hemodynamic hypothesis, promotes atherosclerosis [79, 12].

Four saddle points, two stable foci and one unstable node are identified and classified at the luminal surface of intracranial aneurysm model (Figure 6.3). Among them, two saddle points (B_A, F_A), the two stable foci (A_A, G_A) and the unstable node (C_A) are identified on the aneurysm sac, thus reflecting the intricate aneurysmal hemodynamics. Interestingly, one stable focus is identified on the dome (A_A), consistently with previous results [31, 106]. One saddle point (B_A) and the unstable node (C_A) are identified close to the neck region (Figure 6.3). The other two identified saddle points (D_A, E_A) are located at the luminal surface of the parent artery, in regions characterized by an intricate hemodynamics (i.e., immediately upstream of the aneurysm and close to a bifurcation, respectively).

The complete topological skeleton of the cycle-average WSS vector field at the luminal surface of carotid bifurcation and intracranial aneurysm models is presented in Figures 6.4 and 6.5, respectively. The contraction and expansion patterns, highlighted by the divergence of the normalized cycle-average WSS vector field, identify where unstable and stable manifolds are located.Moreover, the WSS divergence-based approach allows the separation of the luminal surface in regions representing the basins of attraction for the stable fixed points associated with manifolds (i.e., WSS vector trajectories starting in these areas are bound to stay in these regions, attracted to the associated stable fixed points). The effectiveness of the proposed approach in highlighting contraction/expansion regions, and partition of the luminal surface in regions with different WSS vector field behavior emerges from Figures 6.4 and 6.5. Notably, all cycle-average WSS vector stable field fixed points identified at the luminal surface of the carotid bifurcation (Figure 6.4) and of the intracranial aneurysm (Figure 6.5) are located within contraction regions, thus confirming the appropriateness of the proposed approach. On the opposite, as expected by the theory, the unstable node identified at the luminal surface of the aneurysm model, is located within an expansion region (Figure 6.5).

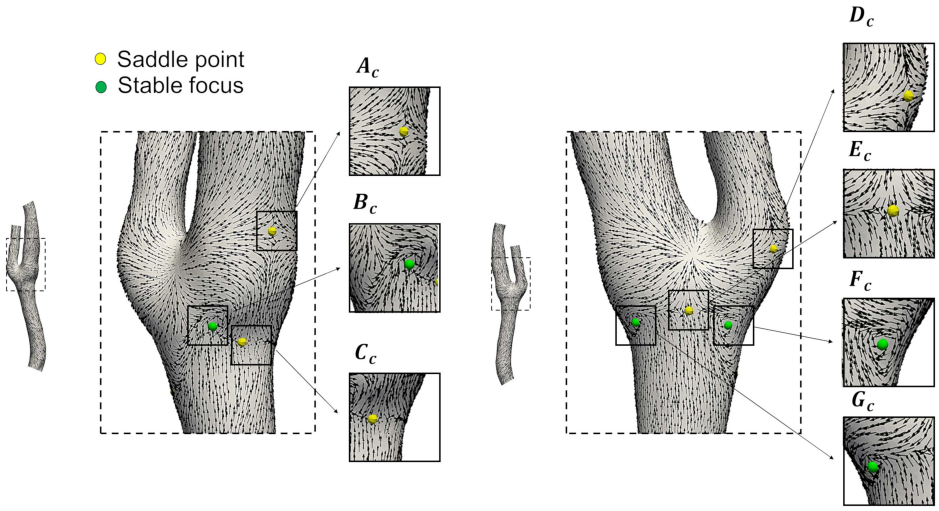

Figure 6.2: Different type of cycle-average WSS fixed points in carotid bifurcation model. Vector field is normalized for visualization. Two different views and a total of 7 insets are displayed to appreciate the vector field arrangement around the fixed points.

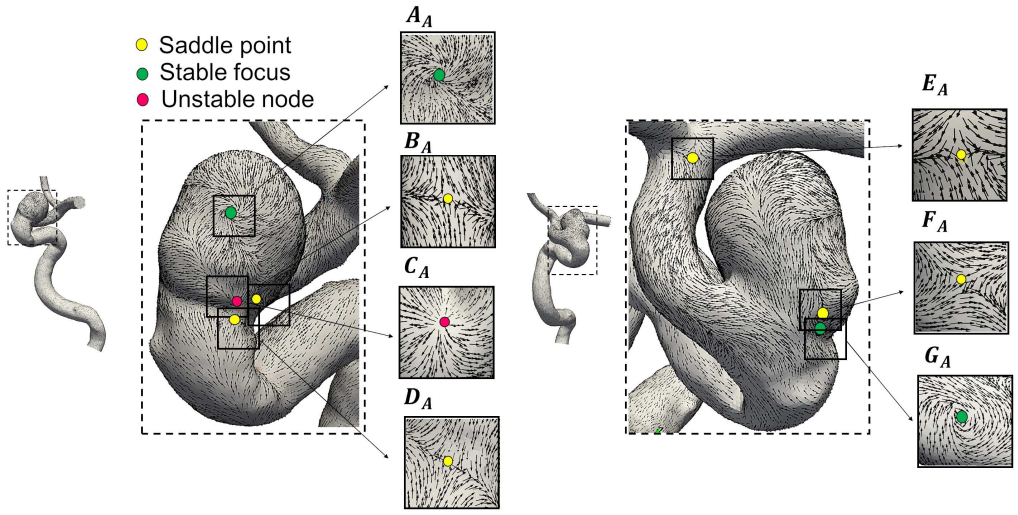

Figure 6.3: Different type of cycle-average WSS fixed points in intracranial aneurysm model. Vector field is normalized for visualization. Two different views and a total of 7 insets are displayed to appreciate the vector field arrangement around the fixed points.

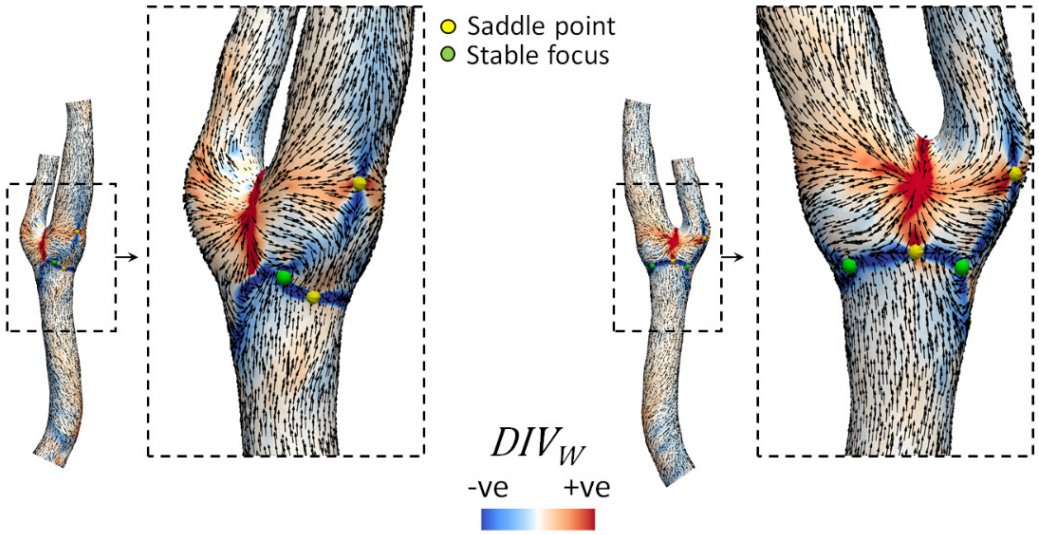

Figure 6.4: Topological skeleton of cycle-average WSS vector field in carotid bifurcation model. Blue and red color define the contraction and expansion region, respectively, linking the fixed points.

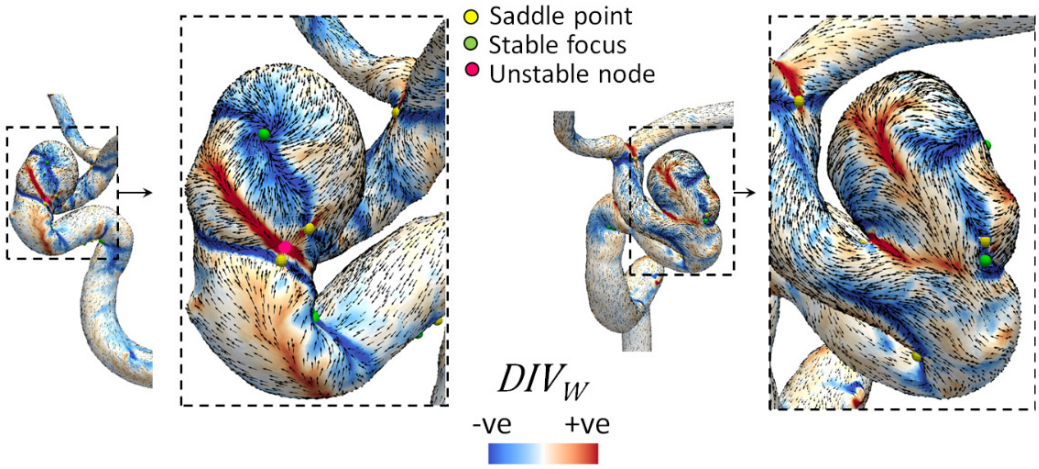

Figure 6.5: Topological skeleton of cycle-average WSS vector field in intracranial aneurysm model. Blue and red color define the contraction and expansion region, respectively, linking the fixed points.

6.4.2 Instantaneous Wall Shear Stress topological skeleton analysis

For an in-depth comprehension of the physiological significance of the WSS vector field fixed points, here their time of residence and nature along the cardiac cycle is investigated. The quantity $RT_{x_{fp}}(e)$ as defined in eq. (3.9) allows the evaluation of the fraction of cardiac cycle each generic surface triangle mesh element is hosting instantaneous WSS fixed points. For visualization purpose, regions of interest R_{fp} (including cycle-average WSS fixed points locations, as identified before in Figures 6.2, 6.3) are highlighted at the luminal surface around high $RT_{x_{fp}}(e)$ regions (Figures 6.6A,6.7A).

For the carotid bifurcation model, the map of $RT_{x_{fp}}(e)$ highlights that there are preferential regions at the luminal surface where instantaneous WSS saddle points and/or stable foci appear and reside for longer fraction of the cardiac cycle (Figure 6.6A). In detail, in regions R_{E_C} and R_{G_C} fixed points residence times is up to 30% of the cardiac cycle (Figure 6.6A).

Interestingly, most of the long fixed points residence time regions at the luminal surface of the carotid bifurcation fall within cycle-average low WSS regions identified by TAWSS20 and TAWSS10 maps (Figure 6.6A), where TAWSS20 (TAWSS10)

represents the luminal surface area exposed to TAWSS below the 20^{th} (10^{th}) percentile. The value of 20^{th} and 10^{th} percentile of TAWSS are imposed according to threshold values proposed elsewhere [19].

The quantity $RT\nabla_{x_{fp}}(e)$ defined in eq. (3.10) measures not only the time of residence, but also the strength of the vector field contraction/expansion around an instantaneous WSS fixed point. The luminal surface around the bifurcation apex of the carotid bifurcation model (Figure 6.6B) presents high $RT\nabla_{x_{fp}}(e)$ values. This is mainly the consequence of the markedly high instantaneous values of WSS divergence in that region, as also confirmed by the fact that instantaneous WSS fixed points reside for a small fraction of cardiac cycle there (Figure 6.6A). To complete the picture, high $RT\nabla_{x_{fp}}(e)$ spots around the apex are not located in low TAWSS regions (Figure 6.6). Contrarily, at locations at the bulb where fixed points reside for a longer fraction of the cardiac cycle, and where TAWSS is low (e.g., R_{E_C} and R_{G_C}, Figure 6.6A), $RT\nabla_{x_{fp}}(e)$ is barely lower than the apex, because of the moderate strength of the contraction/expansion of the WSS vector field, as quantified by instantaneous WSS divergence values there (Figure 6.6B).

Finally, a more detailed analysis carried out using the quantity $RT_{x_{fp}}\left(e_{\bar{\boldsymbol{\tau}}_{fp}}\right)$ as defined in eq. (3.11), highlights the nature and residence time of instantaneous fixed points at locations of the luminal surface where cycle-average WSS vector field fixed points were identified (see Figure 6.2). The results summarized in Table 6.1 clearly show that: (1) in general, instantaneous WSS fixed points reside for small fractions of the cardiac cycle (range $0.0 - 14.5\%$, average 6.4%) in cycle-average WSS fixed points identified locations at the luminal surface; (2) in regions R_{D_C}, R_{E_C} and R_{F_C} instantaneous WSS fixed points are of the same type as cycle-average WSS fixed points; (3) it emerges that at position C_C where a cycle-average WSS saddle point is located (Figure 6.2), the instantaneous WSS vector never qualifies as a fixed point along the cardiac cycle (Figure 6.6A), thus questioning the physical significance of WSS fixed points on cycle-average WSS vector fields; (4) weighting the time of residence of WSS fixed points at the luminal surface with the absolute value of the WSS divergence corresponds to put more emphasis on the strength of the expansion/contraction of the WSS vector field in the closest range, which is higher in regions of the carotid bifurcation such as the apex, which are known to be scarcely atherosusceptible.

The results of the analysis of instantaneous WSS fixed points along the cardiac cycle at the luminal surface of the intracranial aneurysm model are summarized

in Figure 6.7 and in Table 6.2. It can be observed that in regions R_{E_A} and R_{D_A}, identified at the luminal surface of the parent artery, the WSS fixed points residence time $RT_{x_{fp}}(e)$ reaches 70% of the cardiac cycle, meaning that instantaneous WSS fixed points spend a large fraction of the cardiac in the same position, while in regions belonging to the aneurysmal sac fixed points residence time is up to 40% of the cardiac cycle (in region R_{C_A}, Figure 6.7A). Interestingly, the long fixed points residence time locations at the luminal surface of the intracranial aneurysm model are part of the cycle-average low WSS regions identified by TAWSS_{th} map, where TAWSS_{th} represents the luminal surface area exposed to TAWSS below the threshold value, set according to previous studies [107] as the 10% of the value of the mean TAWSS over the parent artery (Figure 6.7A), the sole exception being represented by region R_{A_A} on the aneurysm dome.

In the aneurysm model, the analysis based on a combination of time of residence and strength of the WSS vector field contraction/expansion around instantaneous WSS fixed points ($RT\nabla_{x_{fp}}(e)$) highlights that: (1) high $RT\nabla_{x_{fp}}(e)$ values are located on the neck (R_{C_A} and R_{D_A}, Figure 6.7B), and on the dome of the aneurysmal sac (R_{A_A}, Figure 6.7B); (2) contrary to what observed for the carotid bifurcation, these higher $RT\nabla_{x_{fp}}(e)$ value locations on the aneurysmal neck and dome present high instantaneous values of WSS divergence and, at the same time, moderate-to-high WSS fixed points times of residence (Figure 6.7A); (3) $RT\nabla_{x_{fp}}(e)$ spots outside regions of interest R_{fp} identified on the aneurysmal sac are not observed; (4) at locations (R_{B_A}, R_{E_A}, R_{F_A} and R_{G_A}) where WSS fixed points reside for a sensible fraction of the cardiac cycle, (e.g., R_{E_A} Figure 6.7A) very low $RT\nabla_{x_{fp}}(e)$ values are observed, because of the weak contraction/expansion of the WSS vector field there.

Also in the case of the aneurysm model, the nature and residence time of instantaneous fixed points is investigated with respect to cycle-average WSS vector field fixed points (Figure 6.3) using the quantity $RT_{x_{fp}}\left(e_{\bar{\boldsymbol{\tau}}_{fp}}\right)$.

The results of the analysis for the intracranial aneurysm are summarized in Table 6.2, from which emerges that: (1) instantaneous WSS fixed points reside for large fractions of the cardiac cycle (58.2% and 46.2%) in cycle-average WSS fixed points locations at the luminal surface of the parent vessel; (2) considering cycle-average WSS fixed points on the aneurysmal sac (A_A, B_A, C_A, F_A, G_A, Figures 6.3 and **??**A), instantaneous WSS fixed points reside at those locations for moderate fractions of the cardiac cycle (range $3.6-21.3\%$, average 11.4%); (3) the instantaneous

WSS fixed points are always of the same nature as cycle-average WSS fixed points; (4) at position A_A where a cycle-average WSS stable focus is identified (Figure 6.3), the instantaneous WSS vector qualifies always as a stable focus for the 10.3% of the cardiac cycle (Table 6.2), but this location does not fall within cycle-average low WSS regions identified by TAWSS_{th} map, thus questioning again the physical significance of WSS fixed points on cycle-average WSS vector fields; (5) elevated values of the strength of the expansion/contraction of the WSS vector field around instantaneous WSS fixed points are observed on the aneurysmal dome and close to the neck region, reflecting the intricate hemodynamics characterizing these regions.

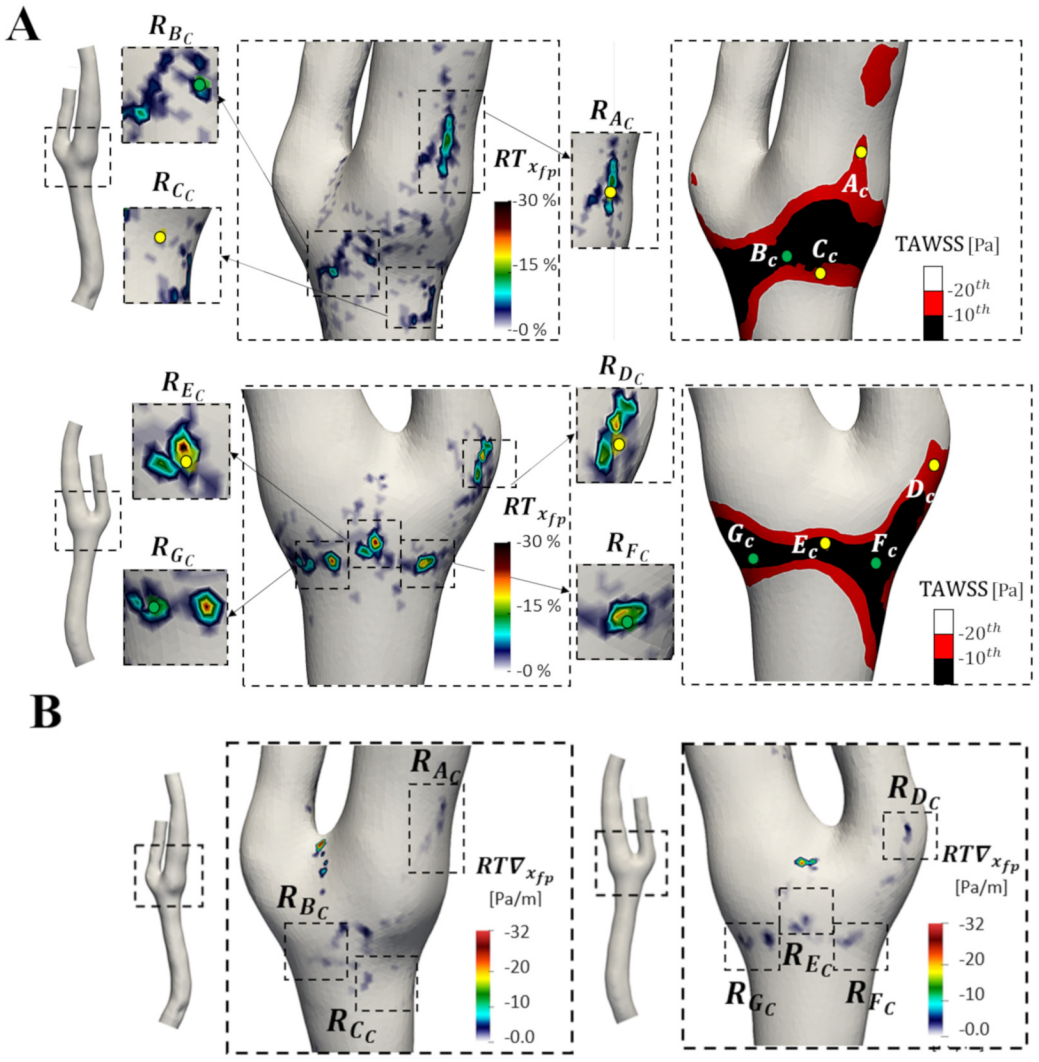

Figure 6.6: Panel A: Map of fixed points residence time $RT_{x_{fp}}(e)$ on the carotid bifurcation model. Two views and seven insets are displayed, zooming on the locations of cycle-average WSS fixed points. Yellow points denote the presence of a saddle point, while green points indicate a stable focus. In the right panels, the exposure to low TAWSS is visualized. Red and black areas denote TAWSS values below respectively the 20^{th} and 10^{th} percentile of the TAWSS distribution. Panel B: Map of measure $RT\nabla_{x_{fp}}(e)$ on the carotid bifurcation model. Two views are displayed. Dashed lines delimit regions R_{A_C}, R_{B_C}, R_{C_C}, R_{D_C}, R_{E_C}, R_{F_C}, and R_{G_C}.

Table 6.1: Analysis of WSS fixed points residence time and nature along the cardiac cycle on the carotid bifurcation model. TAWSS20 (TAWSS10) represents the luminal surface area exposed to TAWSS below the 20^{th} (10^{th}) percentile. SPs and SFs denote Saddle Points and Stable Foci, respectively

Region of interest R_{fp}	Instantaneous WSS fixed points nature in R_{fp}	Cycle-Average WSS fixed point nature in R_{fp}	Instantaneous WSS residence time fixed points and nature at cycle-average WSS fixed point location in R_{fp}	WSS fixed points residence time and the local contraction/expansion in R_{fp}	TAWSS percentile at cycle-average WSS fixed point location in R_{fp}
R_{A_C}	SPs and SFs	SP (A_C)	3.4% (3.4% SPs, 0% SFs)	Low $RT\nabla_{x_{fp}}$	TAWSS20
R_{B_C}	SPs and SFs	SF (B_C)	4.9% (2% SPs, 2.9% SFs)	Low $RT\nabla_{x_{fp}}$	TAWSS10
R_{C_C}	SPs and SFs	SP (C_C)	0% (0% SPs, 0% SFs)	Low $RT\nabla_{x_{fp}}$	TAWSS20
R_{D_C}	SPs	SP (D_C)	1.5% (1.5% SPs, 0% SFs)	Low $RT\nabla_{x_{fp}}$	TAWSS20
R_{E_C}	SPs	SP (E_C)	14.5% (14.5% SPs, 0% SFs)	Low $RT\nabla_{x_{fp}}$	TAWSS10
R_{F_C}	SFs	SF (F_C)	12.5% (0% SPs, 12.5% SFs)	Low $RT\nabla_{x_{fp}}$	TAWSS10
R_{G_C}	SPs and SFs	SF (G_C)	8.2% (0% SPs, 8.2% SFs)	Low $RT\nabla_{x_{fp}}$	TAWSS10

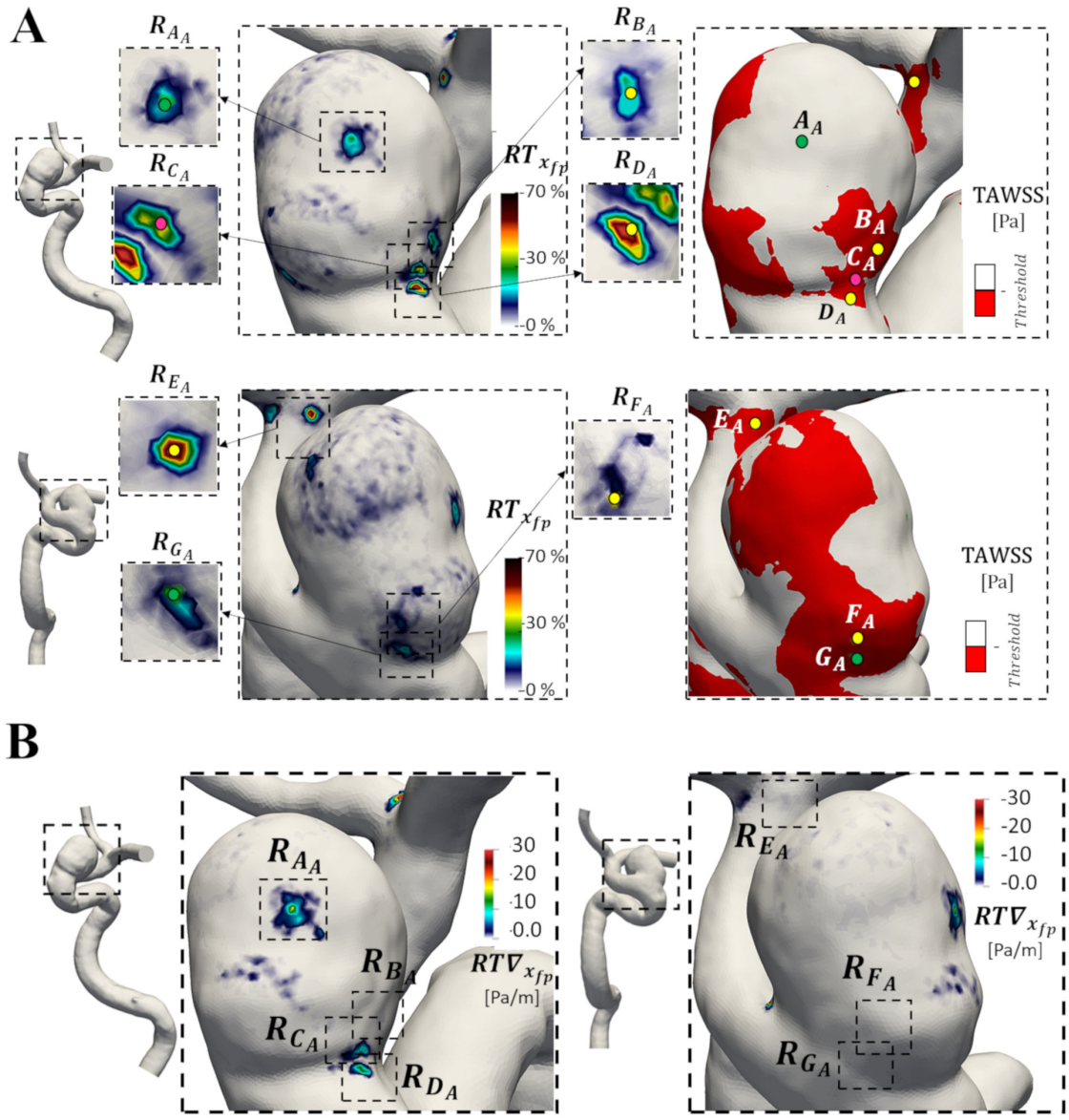

Figure 6.7: Panel A: Map of fixed points residence time $RT_{x_{fp}}(e)$ on the intracranial aneurysm model. Two views and seven insets are displayed, zooming on the locations of cycle-average WSS fixed points. Yellow points denote the presence of a saddle point, green points indicate a stable focus, red points indicate unstable nodes. In the right panels, the exposure to low TAWSS is visualized. Red area denotes TAWSS values below the fixed threshold (10% of the value of the mean TAWSS over the parent artery). Panel B: Map of measure $RT\nabla_{x_{fp}}(e)$ on the intracranial aneurysm model. Two views are displayed. Dashed lines delimit regions R_{A_A}, R_{B_A}, R_{C_A}, R_{D_A}, R_{E_A}, R_{F_A}, and R_{G_A}.

Table 6.2: Analysis of WSS fixed points residence time and nature along the cardiac cycle on the intracranial aneurysm model. $TAWSS_{th}$ represents the luminal surface area exposed to TAWSS below the 10% of the value of the mean TAWSS over the parent artery. SPs, SFs and UNs denote Saddle Points, Stable Foci and Unstable Nodes, respectively

Region of interest R_{fp}	Instantaneous WSS fixed points nature in R_{fp}	Cycle-Average WSS fixed point nature in R_{fp}	Instantaneous WSS residence time fixed points and nature at cycle-average WSS fixed point location in R_{fp}	WSS fixed points residence time and the local contraction/expansion in R_{fp}	TAWSS percentile at cycle-average WSS fixed point location in R_{fp}
R_{A_A}	SFs	SF (A_A)	10.3% SFs	High $RT\nabla_{x_{fp}}$	
R_{B_A}	SPs	SP (B_A)	15.3% SPs	Very low $RT\nabla_{x_{fp}}$	$TAWSS_{th}$
R_{C_A}	UNs	UN (C_A)	21.3% UNs	Moderate $RT\nabla_{x_{fp}}$	$TAWSS_{th}$
R_{D_A}	SPs	SP (D_A)	46.2% SPs	Moderate $RT\nabla_{x_{fp}}$	$TAWSS_{th}$
R_{E_A}	SPs	SP (E_A)	58.2% SPs	Very low $RT\nabla_{x_{fp}}$	$TAWSS_{th}$
R_{F_A}	SPs	SP (F_A)	3.6% SPs	Very low $RT\nabla_{x_{fp}}$	$TAWSS_{th}$
R_{G_A}	SFs	SF (G_A)	6.6% SFs	Very low $RT\nabla_{x_{fp}}$	$TAWSS_{th}$

6.5 Discussion

Unlike previous studies focusing on the cycle-average WSS topological skeleton [22, 100], here the Eulerian-based practical approach has allowed to easily analyze the unsteady nature of WSS fixed points along the cardiac cycle. In general, it emerged that WSS fixed points patterns is markedly instantaneous by nature, with fixed points appearing, moving, disappearing and changing their nature at predisposed locations at the luminal surface of a vessel, along the cardiac cycle. More in detail, on the carotid bifurcation model, it was observed that (1) most of the instantaneous WSS fixed points reside in low cycle-average WSS regions (Figure 6.6A); (2) expansion/contraction of the WSS vector field is strong around those fixed points located in the bifurcation apex, a scarcely atherosusceptible region (Figure 6.6B); (3) instantaneous WSS fixed points co-localize with cycle-average WSS fixed points for small fractions of the cardiac cycle (Table 6.1).
As for the intracranial aneurysm model, it emerged that: (1) both the aneurysmal dome and the neck region are characterized by a marked WSS expansion/contraction action (Figure 6.7B); (2) an instantaneous focus is present on the aneurysm dome throughout the cardiac cycle, as a consequence of the interaction with the wall of the dynamic vortex structures developing in the sac (Figure 6.7A); (3) instantaneous WSS fixed points co-localize with cycle-average WSS fixed points locations for moderate fractions of the cardiac cycle on the aneurysmal sac, and for large fractions on the parent vessel (Table 6.2). Furthermore, the present analysis highlights the importance of considering the unsteadiness of WSS fixed points and manifolds along the cardiac cycle. The consideration of WSS fixed points analysis along the cardiac cycle enriches the information that can be obtained when considering cycle-average WSS topological skeleton [22, 100, 21]: with respect to previous studies mainly focusing on cycle-average WSS topological skeleton, the present findings underline the physical significance of WSS fixed points dynamics along the cardiac cycle. More in detail, it emerged that: (1) on the carotid bifurcation model, the location on the luminal surface where a cycle-average WSS saddle point is located never hosts instantaneous WSS fixed points along the cardiac cycle (Table 6.1); (2) on the intracranial aneurysm model, a persistent instantaneous WSS focus moves over a confined surface area of the sac which is not co-localized with the cycle-average low WSS region (Table 6.2).

Chapter 7

Wall Shear Stress Topological Skeleton Predicts long-term Restenosis Risk after Surgery in the Carotid Bifurcation

A version of this chapter has been published in:
Annals of Biomedical Engineering; 48: 2936-2949, doi.org/10.1007/s10439-020-02607-9, 2020
"Wall shear stress topological skeleton independently predicts long-term restenosis after carotid bifurcation endarterectomy"
U. Morbiducci, V. Mazzi, M. Domanin, G. De Nisco, C. Vergara, D. A. Steinman, D. Gallo

7.1 Introduction

Extensive research has investigated the mechanisms through which the hemodynamic environment at the carotid artery bifurcation influences the origin and progression of cardiovascular diseases [12]. In particular, Wall Shear Stress (WSS) has been recognized as atherogenic [12], with previous evidence demonstrating that exposure to low [19] and oscillatory [108] WSS is a significant independent risk factor for identifying individuals at greater susceptibility for carotid atherosclerosis. The exposure to low WSS appears promising also in terms of predicting the risk

of long-term restenosis after carotid endarterectomy (CEA), a surgical intervention consisting in the removal of the plaque on both symptomatic and asymptomatic patients with moderate to severe carotid stenosis [109].

Long-term restenosis, an important complication affecting CEA outcome leading to development of cerebral symptoms or even carotid occlusion and stroke, presents similarities with native carotid artery stenosis[110, 109] when the absence of post-CEA residual atherosclerosis and short-term restenosis (i.e., $>$ 6 months and $<$ 24 months [111, 110]) are accounted for. Thus, the mechanisms underlying both atherosclerosis and long-term restenosis are mechanistically influenced by the hemodynamic environment. However, the specificity of the currently considered hemodynamic features based on low and oscillatory WSS, which are significant but only moderate predictors of disease localization [19, 110], and their clinical added value, hampered by the practical challenges of including hemodynamic information from computational modelling in large prospective clinical studies [112], have been questioned [19, 110].

To improve, refine and extend our current understanding of the association between local hemodynamics and vascular disease, an increasing interest has been recently dedicated to the analysis of WSS vector field topological skeleton,[23, 21] composed by fixed points and the stable/unstable manifolds connecting them. At a fixed point, the WSS vector field focally vanishes, and manifolds identify regions where the WSS vector field exerts a contraction/expansion action on the endothelial cells lining the luminal surface. It can therefore be presumed that WSS topological skeleton features influence vascular pathophysiology. This presumption is supported by the fact that the WSS topological skeleton is determined by blood flow structures associated to adverse vascular response at the carotid bifurcation, including near-wall flow stagnation, separation and recirculation [21]. Moreover, the fluid-phase mass transport of solutes near the wall has been demonstrated to be governed by the cycle-average WSS topological skeleton [23, 24]. However, the exact mechanisms by which the WSS topological skeleton and related descriptors influence vascular pathophysiology are still underexplored.

The present study investigates the association between the WSS topological skeleton and markers of vascular disease at the carotid bifurcation from real-world, longitudinal clinical data. To do that, a cohort of 12 asymptomatic patients submitted to 13 CEA interventions [113] was adopted. A recently proposed Eulerian-based

analysis of the topological skeleton of the WSS vector field was applied to patient-specific computational hemodynamic models of the carotid bifurcation at 1 month after CEA. Intima-media thickness (IMT) was clinically measured at 60 months after CEA to provide an indicator of vascular response and detect the presence of long-term restenosis. Additionally, to explore how the CEA intervention impacts local hemodynamics and, ultimately, the clinical outcome, the WSS topological skeleton analysis was carried out on the pre-CEA (i.e., stenotic) carotid bifurcation models.
For the purpose of contextualization of the results, the WSS topological skeleton analysis was (1) extended to a computational hemodynamics dataset of 46 ostensibly healthy carotid bifurcation models, and (2) complemented with the analysis of the exposure to low WSS, which was previously demonstrated to be directly associated to adverse vascular responses on the same post-CEA dataset adopted here [113].

7.2 Methods

7.2.1 Patient population data

Endarterectomy procedures were performed on 13 carotid arteries in 12 patients at the Vascular Surgery Operative Unit of Fondazione IRCCS Ca' Granda, Ospedale Maggiore Policlinico in Milan. All of the 13 carotid arteries had diameter stenosis of greater than 70 %. As detailed elsewhere,[114, 115] all cases were asymptomatic, one case had contralateral occlusion of the internal carotid artery (ICA), and three cases were previously submitted to contralateral CEA. Age, sex, location of carotid stenosis, diameters of ICA and risk factors are listed in Table 7.1. The study was approved by the I.R.C.C.S. Fondazione Policlinico Ethics Committee according to institutional ethics guidelines, and participants provided informed consent. After endarterectomy, patch graft angioplasty was performed in 9 cases (PG1-9) using a polyester collagen-coated patch (Ultra-thin Intervascular®, Mahwah,NJ U.S.A), and 4 cases underwent primary closure, i.e. without patch graft (PC1-4). Further details about the surgical cohort are reported elsewhere[113].
All patients were then submitted to Doppler ultrasound (DUS) follow-up at 3, 24 and 60 months. Cases of restenosis were defined by a peak systolic velocity (PSV) of $>$ 130 cm/s as measured by DUS (an indicator of the presence of a diameter

stenosis greater than 50 %,[116] according to the European Carotid Stenosis Trial standard). No sign of restenosis and no symptoms of cerebrovascular ischemia emerged in any patient from follow-ups at 3 and 24 months. During the follow-up period, one patient died for myocardial infarction (PG4), and one for pancreatic carcinoma (PG8). All eligible patients were submitted to DUS follow-up at 60 months. Intima-media thickness (IMT) was measured using a Philips iU22 ultrasound scanner with linear 8 MHz probe (Philips Ultrasound, Bothwell, U.S.A) and automatically extracted offline with the clinical software Qlab (Philips Ultrasound, Both-well, U.S.A) at the following locations: ICA distal to the carotid bulb (CB); CB; distal end of the common carotid artery (CCA), i.e., the flow divider (FD); CCA at 1 cm and 2 cm from the distal end of the CCA (FD- 1cm and FD-2cm, respectively). As previously proposed, [113] the maximum value of IMT found in the bifurcation region was also considered.

Table 7.1: Age, classification of sex (F female; M male), clinical risk factors (HTN: presence of hypertension, DIAB: diabetes, DYSLIP: dyslipidemia, SMOKE: smoking), location of the carotid stenosis (CCA Common carotid artery; CB Carotid bulb; ICA Internal carotid artery; ECA external carotid artery), peak systolic velocity (PSV) measurements at the stenosis, and diameter measurements at CCA, CB, ICA and ECA. * Cases PG1 and PG2: respectively, right and left carotid of the same patient.

Patient	**Age (years)**	**Sex**	**Clinical Risk Factors**	**Stenosis Location**	**ICA (mm)**
PG1*	65	F	HTN	CCA, CB	5.00
PG2*	65	F	HTN	CB	5.40
PG3	81	F	HTN, SMOKE	CB, ICA	4.20
PG4	82	F	HTN	CB, ICA	4.00
PG5	72	M	HTN, DIAB, SMOKE	ICA	4.50
PG6	68	F	HTN, SMOKE	CB	4.50
PG7	71	F	HTN	CB, ICA	4.90
PG8	76	M	HTN, SMOKE	CB	4.00
PG9	67	M	HTN, DIAB, DYSLIP, SMOKE	CB, ICA	4.80
PC1	81	F	HTN, DYSLIP, SMOKE	CB, ICA	4.74
PC2	79	M	DIAB, DYSLIP	CB, ICA	5.00
PC3	79	M	HTN, DIAB, DYSLIP, SMOKE	CCA, CB, ICA	7.00
PC4	61	M	HTN, DYSLIP	CB	6.60

7.2.2 Computational Hemodynamics

Magnetic resonance angiography (MRA) acquisitions were performed before and within a month after surgery to obtain the pre-CEA and post-CEA 3D geometry of the carotid bifurcations with a level set approach using the Vascular Modeling Toolkit software (VMTK, www.vmtk.org), as detailed elsewhere [113, 117]. Blood was modelled as an incompressible homogeneous Newtonian fluid [118, 119], under laminar flow and rigid wall assumptions [115, 117]. The governing equations of fluid motion were solved numerically using the finite element library LifeV (http://www.lifev.org) in discretized fluid domains discretized with tetrahedral meshes [117]. Patient-specific flow rate waveforms were extracted at the CCA and ICA before and after CEA from echo-color DUS and imposed as boundary conditions in the numerical simulations. At the external carotid artery (ECA) outlet section, a traction-free condition was imposed. Details on image acquisition, mesh refinement study and computational settings are extensively described elsewhere [115, 113, 117].

To characterize the WSS topological skeleton features of the physiological carotid artery hemodynamics, and provide objective thresholds for quantitative analysis of the WSS topological skeleton descriptors introduced in the following, the topological skeleton analysis was performed on a previously characterized computational hemodynamics dataset of 46 ostensibly healthy carotid bifurcation models [19, 20] denoted with the prefix He (He1–He46). Briefly, the 3D geometry of 46 carotid bifurcations was reconstructed from contrast enhanced MRA30 with a level set approach using the VMTK software and the governing equations of fluid motion were solved numerically using a validated in-house finite element solver [19] with the same assumptions as the CEA dataset. Patient-specific flow rate waveforms were extracted from cine phase contrast magnetic resonance acquisitions at the CCA and ICA and imposed as boundary conditions in the numerical simulations, while at the ECA outlet section a traction-free condition was imposed [19]. Further information on image acquisition, mesh refinement study and computational hemodynamic simulation of the ostensibly healthy carotid bifurcations is detailed elsewhere [19, 20, 120].

7.2.3 WSS Topological Skeleton Analysis and Quantitative Description

Starting from the WSS vector distribution at the luminal surface, the WSS topological skeleton analysis was carried out applying the proposed Eulerian-based method (Figure 3.1).

As a first step, the WSS topological skeleton of the cycle-average WSS vector field at the luminal surface was analysed. Subsequently, the WSS topological skeleton dynamics along the cardiac cycle was characterized. In order to measure the amount of variation in the WSS contraction/expansion action exerted at the carotid luminal surface along the cardiac cycle, here we adopted the quantity Topological Shear Variation Index ($TSVI$), defined in eq. (3.12).

The unsteady nature of the WSS vector field fixed points along the cardiac cycle was characterized using the WSS fixed point weighted residence time ($RT\nabla_{x_{fp}}(e)$) along the cardiac cycle, defined in eq. (3.10).

In order to perform a quantitative analysis of the WSS topological skeleton, each pre-CEA, post-CEA and healthy carotid bifurcation was split in its CCA, ICA and ECA branches [121]. The bifurcation region was delimited by sections located at 3, 5 and 2 radii along the CCA, ICA and ECA, respectively [122] (denoted CCA3, ICA5 and ECA2). According to a previously employed threshold-based approach for the identification of regions at the luminal surface exposed to disturbed shear, [113, 20, 123] here the exposure to large variations in the WSS contraction/expansion action was quantified by the relative surface area exposed to high values of $TSVI$, considering as threshold value the 80^{th} percentile of the pooled $TSVI$ distribution of the healthy models in the CCA3-ICA5-ECA2 region. This variable, denoted as Topological Shear Variation Area (TSVA), defines the relative area exposed to high normalized WSS divergence variability. Similarly, the exposure to the action of instantaneous WSS fixed points was quantified by the relative surface area exposed to non-null values of $RT\nabla_{x_{fp}}(e)$, i.e. considering the luminal surface area where fixed points occurred along the cardiac cycle in the CCA3-ICA5-ECA2 region. This variable is denoted as weighted Fixed Points Area (wFPA).

To complement the WSS topological skeleton characterization, the luminal distribution of Time-Averaged Wall Shear Stress (TAWSS) magnitude along the cardiac cycle was also evaluated, as the exposure to low TAWSS values was previously linked to an increased long-term restenosis risk [113]. The exposure to low TAWSS

values was quantified by the relative surface area exposed to TAWSS values below a threshold value, corresponding to the 20^{th} percentile of the pooled TAWSS distribution of the healthy models in the CCA3-ICA5-ECA2 region. This variable is denoted as Low Shear Area (LSA). Oscillatory WSS was not considered here as a previous investigation on the post-CEA cohort reported a not significant association with IMT [113].

7.2.4 Statistical analysis

Differences among the three cohorts (i.e., pre-CEA, post-CEA and healthy) in terms of WSS features were evaluated with a Wilcoxon rank sum test, with significance assumed for $p < 0.05$. The relationships between the relative exposure to high $TSVI$, $RT\nabla_{x_{fp}}(e)$ and low TAWSS (respectively, TSVA, wFPA and LSA) were assessed with linear regression analysis. The quality of the regression was evaluated with the coefficient of determination R^2. Significance was assumed for $p < 0.05$. Successively, the nature of the relationship (if any) between WSS topological skeleton descriptors and clinical follow-up data was explored in the post-CEA dataset to test the physiological significance of WSS topological skeleton. Linear regression analysis was used to identify relationships between WSS topological skeleton descriptors with the measured IMT values. The quality of the regression was evaluated with the coefficient of determination R^2. Significance was assumed for $p < 0.05$.

7.3 Results

7.3.1 Cycle-Average WSS Topological Skeleton Analysis

As a preliminary step, an exploration of the cycle-average WSS vector field topological skeleton was carried out to identify its main integral features on pre-CEA, post-CEA and healthy cohorts. Cycle-average WSS contraction/expansion regions, highlighted by the divergence of the normalized cycle-average WSS vector field, are presented in Figure 7.1. In pre-CEA models, a WSS contraction region was located in correspondence of the cross-sectional area reduction at the stenosis, while for the post-CEA and healthy cohorts contraction and expansion regions were mainly located at the carotid bulb (Figure 7.1). A WSS expansion region

was identified around the bifurcation apex as a feature common to all the carotid models (Figure 7.1). As for the cycle-average WSS fixed points, saddle points, stable foci and unstable nodes were present on the carotid luminal surface of most of the carotid models, independent of the cohort, but at different locations: (1) in the pre- CEA cohort, cycle-average WSS fixed points were mostly located in proximity to the stenosis; (2) on post- CEA models, cycle-average WSS fixed points were located at the carotid bulb, in general with similarities to the cycle-average WSS topological skeleton of healthy carotid bifurcations (Figure 7.1). A detailed analysis on the occurrence of cycle-average WSS fixed points for pre-CEA, post-CEA and healthy cohorts is reported in the Supplementary Material, highlighting that the healthy cohort presented on average the largest number of saddle points and unstable nodes in the bifurcation region (Fig. 7.8, Supplementary Material). Furthermore, the complete topological skeleton of the cycle-average WSS vector field can be better appreciated on selected representative cases for pre-CEA, post-CEA and healthy cohorts in Figure 7.9 of the Supplementary Material.

7.3.2 WSS Topological Skeleton Dynamics Along the Cardiac Cycle

WSS topological skeleton was then analyzed along the cardiac cycle to account for its dynamics. The visualization of the $TSVI$ luminal distributions in the pre-CEA and post-CEA cohorts (Figure 7.2) was extended beyond the bifurcation region delimited by sections CCA3-ICA5-ECA2 to include in the pre-CEA models possible distal ICA/ECA stenoses.

For the pre-CEA cohort, $TSVI$ maps highlighted that the highest variations in the contraction/expansion action exerted by the WSS on the endothelium along the cardiac cycle were located mainly immediately downstream of the stenosis, where recirculating flow is expected. In the post-CEA cohort, high $TSVI$ regions were observed at the cross-sectional enlargement in correspondence of the bifurcation, a known promoter of disturbed flow [124, 113], and extended downstream in the ICA and ECA. Considering the $TSVI$ luminal distributions in the healthy cohort (Figure 7.2), the regions undergoing large variation in the WSS contraction/expansion action were in general located at the cross-sectional enlargement in the CCA, at the bulb in the ICA and around the bifurcation apex.

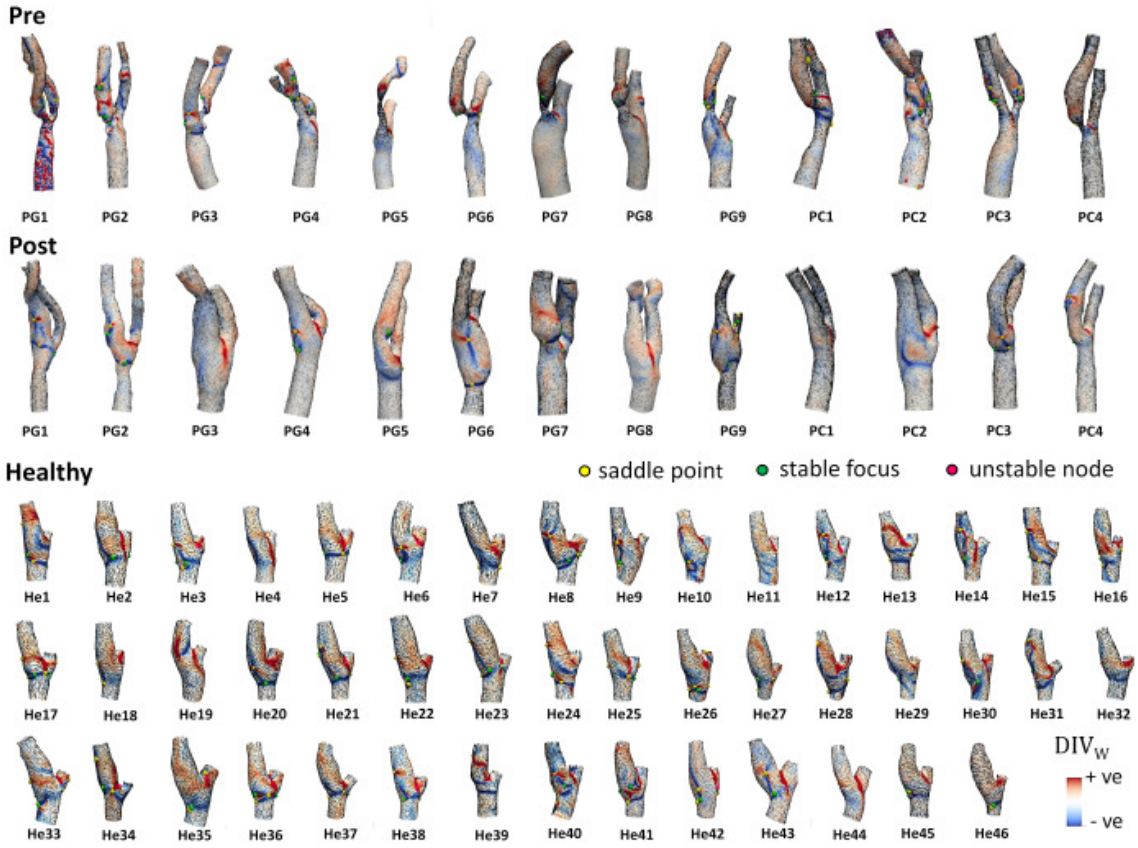

Figure 7.1: Topological skeleton of cycle-average WSS vector in pre-CEA (Pre), post-CEA (Post) and healthy cohorts. The topological skeleton in pre-CEA and post-CEA cohorts is extended beyond the bifurcation region (delimited by sections CCA3- ICA5-ECA2) to include in the pre-CEA models possible distal stenoses. Blue and red color define contraction and expansion regions, respectively. The WSS vector field is normalized for visualization.

In terms of $TSVI$ averaged over the bifurcation region, marked differences in the distributions as well as significant differences emerged between the healthy and both pre- and post-CEA cohorts ($p < 0.001$), as highlighted by the violin plots in Figure 7.3.

To further characterize the high variations in the contraction/expansion action exerted by the WSS on the endothelium along the cardiac cycle, TSVA values were also evaluated in the three cohorts: (1) markedly different distributions were observed among the three cohorts (Figure 7.3); (2) statistically significant differences emerged between post-CEA and healthy cohorts ($p < 0.05$, Figure 7.3); (3) the post-CEA cohort exhibited the lowest intra-variability with respect to the other

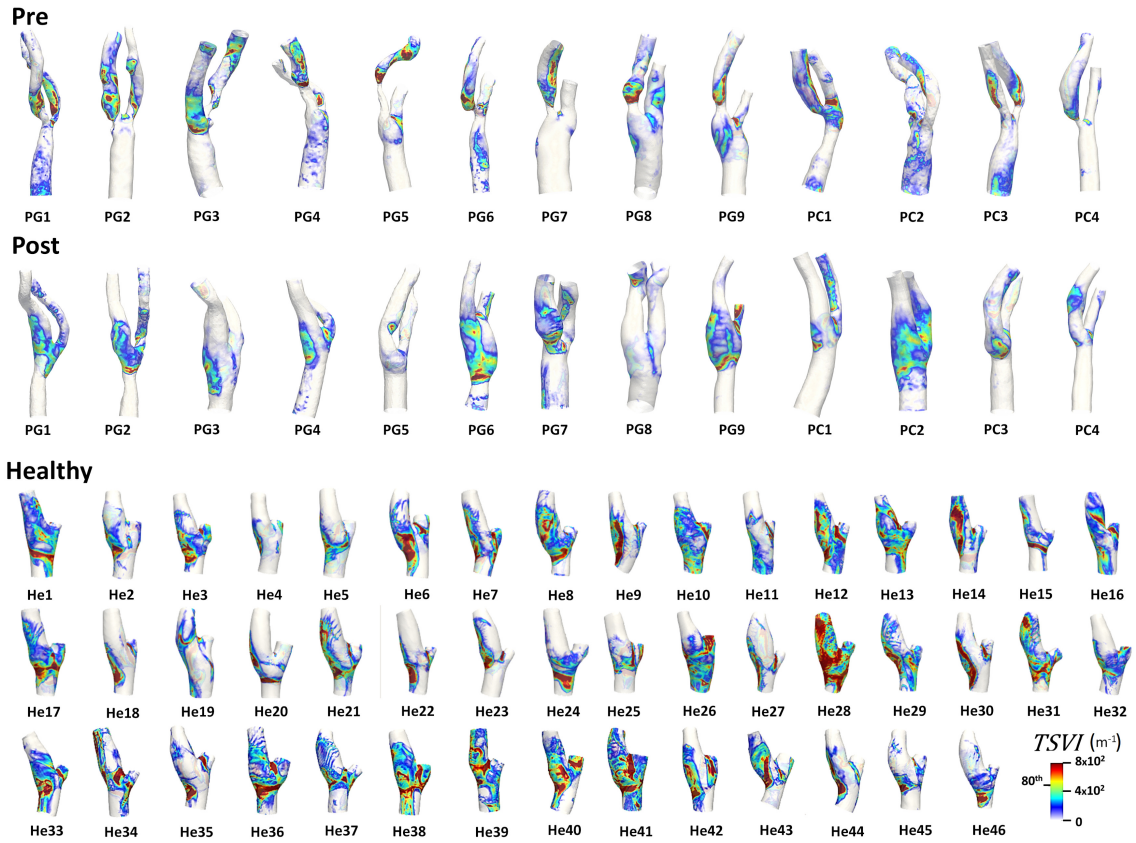

Figure 7.2: Luminal distribution of the Topological Shear Variation Index ($TSVI$) in pre-CEA (Pre), post-CEA (Post) and healthy cohorts. The $TSVI$ distribution in pre-CEA and post-CEA cohorts is extended beyond the bifurcation region (delimited by sections CCA3-ICA5-ECA2) to include in the pre-CEA models possible distal stenoses. The 80^{th} percentile value of the pooled $TSVI$ distribution of the healthy cohort in the bifurcation region is reported in the legend.

cohorts for both mean $TSVI$ and TSVA (Figure 7.3).

The analysis of the luminal surface distribution of WSS fixed points weighted residence time along the cardiac cycle highlighted their focal nature on the luminal surface of the carotid bifurcations, giving origin to a scattered distribution of non-null $RT\nabla_{x_{fp}}(e)$ (Figure 7.4).

In pre-CEA carotid models, the highest $RT\nabla_{x_{fp}}(e)$ were located immediately downstream of the stenosis, differing from the carotid models in the post-CEA and healthy cohorts, the latter exhibiting the lowest $RT\nabla_{x_{fp}}(e)$. Moreover, a marked co-localization can be observed between high $TSVI$ and high $RT\nabla_{x_{fp}}(e)$ regions at the luminal surface (Figures 7.2 and 7.4, respectively). Considering the

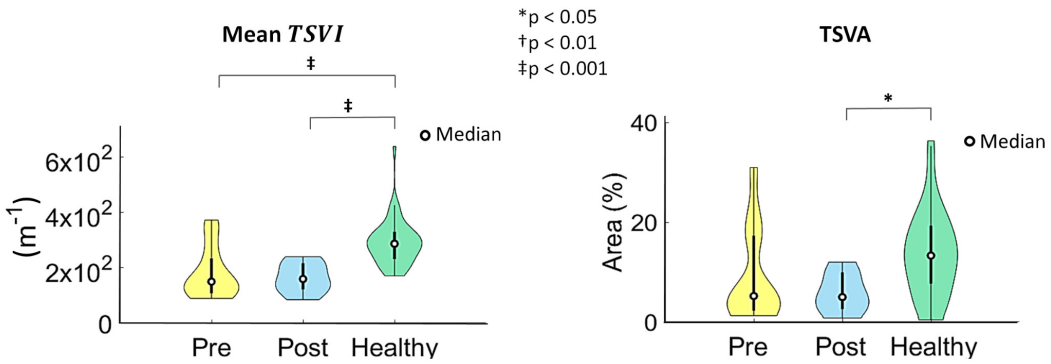

Figure 7.3: Violin plots of the mean value of the Topological Shear Variation Index ($TSVI$) and the Topological Shear Variation Area (TSVA) in the bifurcation region (delimited by sections CCA3-ICA5-ECA2) for pre-CEA (Pre), post-CEA (Post) and healthy cohorts. The distribution, median and quartile range are displayed for each cohort. Differences among the three cohorts are evaluated with a Wilcoxon rank sum test.

values of $RT\nabla_{x_{fp}}(e)$ averaged over the bifurcation region, also in this case marked differences emerged in the distributions for the three cohorts (Figure 7.5), as well as statistically significant differences between the healthy and both pre- and post-CEA cohorts ($p < 0.01$, Figure 7.5). The exposure to high values, quantified by wFPA, resulted significantly different between post-CEA and healthy cohorts only ($p < 0.05$, Figure 7.5).

For each investigated carotid bifurcation model, the visualization of the surface area exposed to low TAWSS (LSA), highlighting wide interindividual variability, is reported in Figure 7.6.

The distribution of the values of TAWSS averaged over the bifurcation region in the three cohorts was markedly different between the pre-CEA and both post-CEA and healthy cohorts, as highlighted by the shape of violin plots in Figure 7.7 and confirmed by the statistically significant differences between the healthy and both pre- and post-CEA cohorts ($p < 0.01$, Figure 7.7). Statistically significant differences in LSA values in the bifurcation region emerged between the pre CEA and both post-CEA and healthy cohorts ($p < 0.05$ and $p < 0.01$, respectively, Figure 7.7), whereas the LSA in the bifurcation region for the post-CEA and healthy cohorts was not significantly different (Figure 7.7).

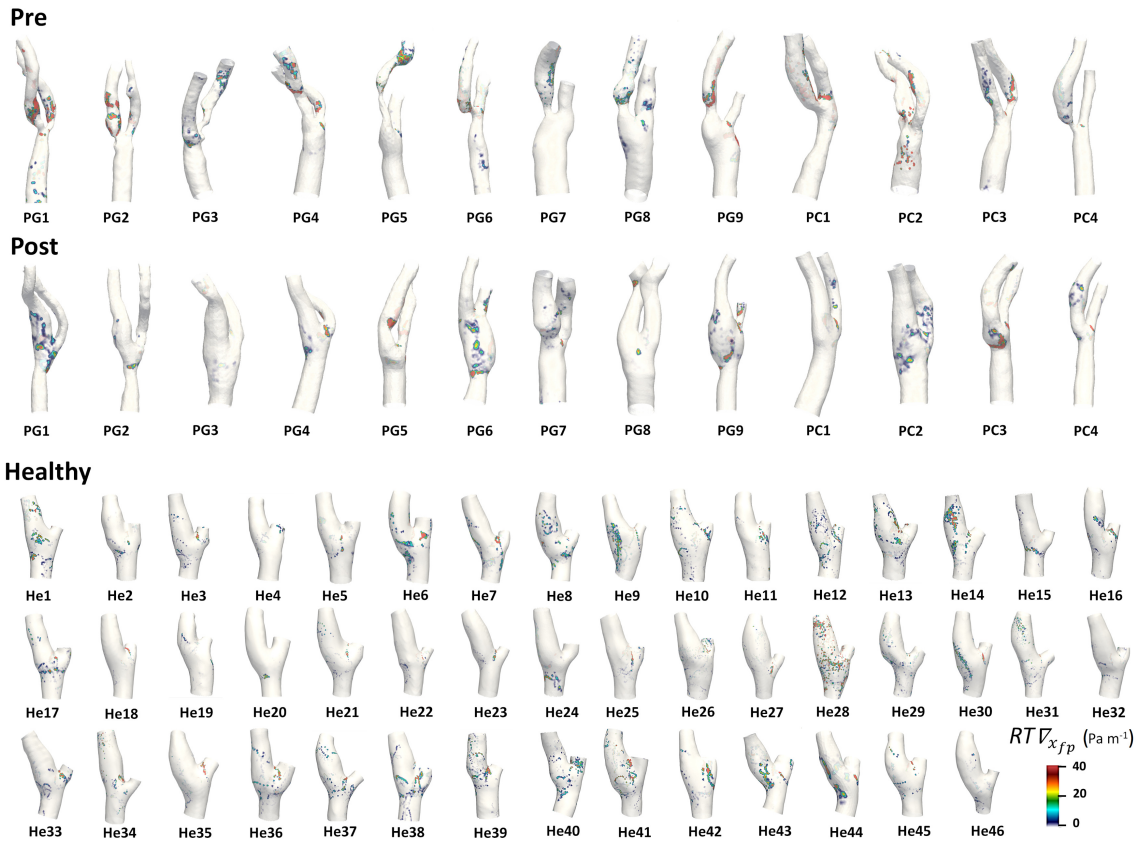

Figure 7.4: Luminal distribution of WSS fixed points weighted residence time ($RT\nabla_{x_{fp}}(e)$) in pre-CEA (Pre), post-CEA (Post) and healthy cohorts. The $RT\nabla_{x_{fp}}(e)$ distribution in pre-CEA and post-CEA cohorts is extended beyond the bifurcation region (delimited by sections CCA3-ICA5-ECA2) to include in the pre-CEA models possible distal stenoses.

7.3.3 Relationships Among WSS Features

The coefficients of determination R^2 between each couple of WSS-based descriptors are summarized in Table 7.2. As for the WSS topological skeleton, significant direct associations emerged between wFPA and TSVA for all three cohorts, ranging from $R^2 = 0.463$ ($p < 0.05$) in the post-CEA cohort to $R^2 = 0.646$ ($p < 0.01$) in the pre-CEA cohort (Table 7.2). For all three cohorts LSA was not associated to either wFPA or TSVA (Table 7.2), indicating that those WSS topological skeleton descriptors represent statistically independent variables with respect to the commonly adopted exposure to low TAWSS as a main indicator of disturbed shear in arteries [113, 19, 12].

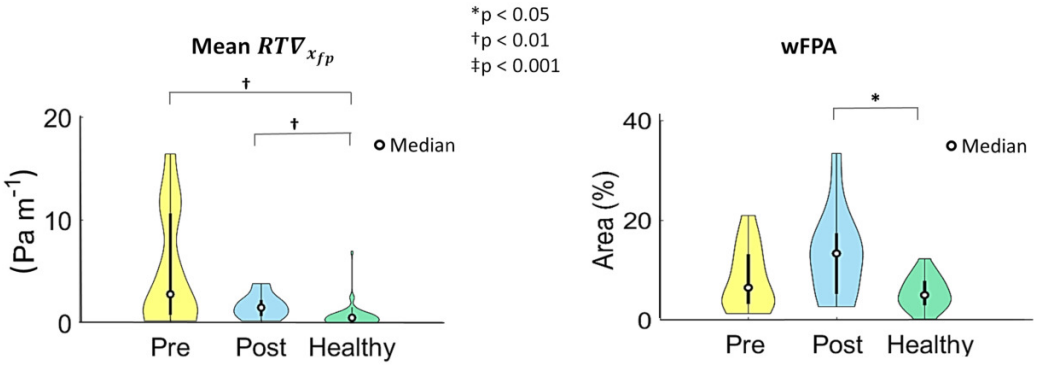

Figure 7.5: Violin plots of the mean value of WSS fixed points weighted residence time ($RT\nabla_{x_{fp}}(e)$) and weighted Fixed Points Area (wFPA) in the bifurcation region (delimited by sections CCA3-ICA5-ECA2) for pre-CEA (Pre), post-CEA (Post) and healthy cohorts. Distribution, median and quartile range are displayed for each cohort. Differences among the three cohorts are evaluated with a Wilcoxon rank sum test.

Table 7.2: Pairwise correlations among the Topological Shear Variation Area (TSVA), the weighted Fixed Points Area (wFPA), and the Low Shear Area (LSA). (‡ $p < 0.001$)

	Pre		**Post**		**Healty**	
R^2	TSVA	LSA	TSVA	LSA	TSVA	LSA
wFPA	0.646‡	0.075	0.463‡	0.292	0.554‡	0.001
TSVA		0.193		0.164		0.011

7.3.4 Wall Shear Stress vs. Clinical Outcome

Linear regressions revealed significant associations between the WSS topological skeleton descriptors and IMT at 60 months follow up. In detail, a significant association emerged between maximum IMT and both TSVA ($R^2 = 0.505$, $p < 0.05$) and wFPA ($R^2 = 0.534$, $p < 0.05$), as reported in Table 7.3. A significant association was observed also between LSA and maximum IMT ($R^2 = 0.619$, $p < 0.001$, Table 7.3). These associations, albeit slightly weaker ($p < 0.05$), were also observed considering the IMT values at the CB (Table 7.3). In the ICA distally to the CB, wFPA and LSA were significantly associated with the local IMT values (respectively, $R^2 = 0.541$, $p < 0.001$ and $R^2 = 0.530$, $p < 0.05$, Table 7.3), whereas TSVA was not.

Figure 7.6: Luminal surface area exposed to low Time-Averaged Wall Shear Stress (TAWSS) as expressed by the Low Shear Area (LSA), in pre-CEA (Pre), post-CEA (Post) and healthy cohorts. The LSA in pre-CEA and post-CEA cohorts is extended beyond the bifurcation region (delimited by sections CCA3-ICA5-ECA2) to include in the pre-CEA models possible distal stenoses. Red areas represent TAWSS value below the 20^{th} percentile of the pooled TAWSS distribution of the healthy models in the bifurcation region.

7.4 Discussion

WSS topological skeleton features reflect cardiovascular flow complexity [23, 22, 21] with direct links to arterial flow patterns like near-wall flow stagnation, separation and recirculation, which are known to be promoting factors for cardiovascular disease [21, 12]. In this sense, the role of WSS topological skeleton in vascular pathophysiology is currently based on circumstantial evidence documenting how the complex flow features associated to the WSS topological skeleton induce a

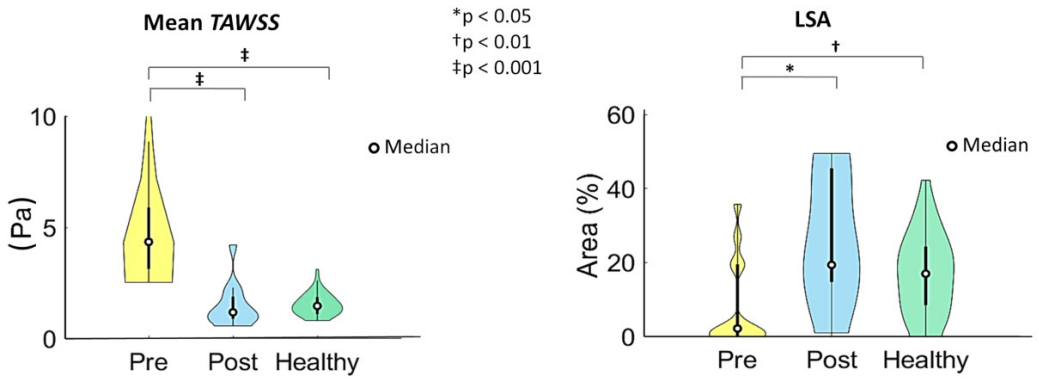

Figure 7.7: Violin plots of the mean value of Time-Averaged Wall Shear Stress (TAWSS) and Low Shear Area (LSA) in the bifurcation region (delimited by sections CCA3-ICA5-ECA2) for pre-CEA (Pre), post-CEA (Post) and healthy cohorts. Distribution, median and quartile range are displayed for each cohort. Differences among the three cohorts are evaluated with a Wilcoxon rank sum test.

Table 7.3: Relationship between the hemodynamic variables TSVA, wFPA or LSA and intima-media thickness (IMT) measurements.).
(Maximum IMT, IMT measured at the bifurcation level (flow divider FD), CCA at 2 cm and 1 cm proximal to the FD (FD-2 cm and FD-1 cm), at the CB, at the ICA downstream of the CB. CCA: common carotid artery, CB: carotid bulb, FD: flow divider, ICA: internal carotid artery.)
($*\,p < 0.05$, $\dagger\, p < 0.01$, $\ddagger\, p < 0.001$)

Coefficient of determination R^2	TSVA	wFPA	LSA
Maximum IMT	0.505∗	0.534∗	0.619‡
IMT at FD-2 cm	0.116	0.108	0.006
IMT at FD-1 cm	0.004	0.271	0.046
IMT at FD	0.032	0.161	0.272
IMT at CB	0.474∗	0.425∗	0.421∗
IMT at ICA	0.090	0.541†	0.530∗

focal vascular response [21]. At the carotid bifurcation, the extent of flow recirculation has been shown to correlate with atherosclerotic biomarkers [125], while flow stagnation and separation at the carotid bulb have been associated to endothelial dysfunction [19] and intimal thickening [79], respectively. In addition, further circumstantial evidence about the role of the WSS topological skeleton in vascular disease has been provided by previous studies demonstrating that the cycle-average WSS topological skeleton governs the near-wall mass transport in arteries [23, 21,

24], a process linked to the onset and progression of early atherosclerosis [11].
Here, we directly link the WSS topological skeleton to the vascular response after 60 months follow-up, defined by clinical IMT measurements. The IMT measurements additionally provide an indicator of restenosis, a common adverse event of CEA procedures [109]. As a main finding of the study, we report that the investigated WSS topological descriptors TSVA and wFPA were associated with the IMT measurements at 60 months follow-up after CEA in the CB and in the ICA (R^2 up to 0.541,$p = 0.009$ as presented in Table 7.3). Albeit the strength of these associations is moderate, it is comparable to the strength of the correlation between exposure to low WSS and IMT measurements at 60 months follow-up (Table 7.3).
Distilling these correlations into mechanistic implications, the here-proposed topological skeleton analysis suggests that exposure to (1) high temporal variation of WSS contraction/expansion action on the endothelium (quantified by TSVA) and (2) high residence times of fixed points at the luminal surface, weighted by WSS contraction/expansion strength (quantified by wFPA), may act as biomechanical triggers of long-term restenosis after CEA, a process anecdotally anticipated to vascular surgeons by the presence of flow disturbances [109]. In other words, our findings support the hypothesis that the WSS topological skeleton features here considered could contribute to promote long-term restenosis, which represents recurrent atherosclerosis [110, 109]. This is corroborated by the fact that, in post-CEA cohort: (1) within 3 months of CEA no sign of lesions (which would represent residual atherosclerosis rather than restenosis [109]) was reported; (2) short-term restenosis, developing between 6 and 24 months postoperatively subsequently to neointimal hyperplasia [109], was not observed clinically after 24 months from CEA. Therefore, the approach presented here potentially contributes to a deeper understanding of the hemodynamics- driven processes underlying long-term restenosis development in the carotid bifurcation and could be extended to the study of biomechanical triggers of atherosclerosis and vascular disease.
To investigate more in depth the physiological significance of the WSS topological skeleton features, the analysis was extended to a dataset of ostensibly healthy carotid bifurcation models. By comparing the pre- CEA, post-CEA and healthy cohorts, it was possible to understand to what extent the pathological pre-CEA near-wall hemodynamics can be restored towards a more physiological condition as a result of the CEA intervention. Interestingly, on average it emerged that differences in WSS topological skeleton features with respect to the healthy carotid

bifurcations persisted after the CEA intervention (Figs. 7.3 and 7.5). Moreover, the contribution of saddle points and foci to the wFPA was associated to maximum IMT, IMT values at the CB and at the ICA distally to the CB (R^2 up to0.557, $p < 0.01$ as reported in Table S1, Supplementary Material), while the contribution of nodes to the wFPA was weakly associated to IMT values measured at 2 cm from the distal end of the CCA ($R^2 = 0.390$ $p < 0.05$, Table S1, Supplementary Material). This suggests an influence of the type of WSS fixed point on the associations between wFPA and IMT measurements at 60 months.

On the same post-CEA cohort adopted here, a significant direct association between the exposure to low WSS (quantified by LSA) with maximum IMT at 60 months follow up after CEA was previously reported [113]. An exact understanding of the mechanistic process underlying the development of carotid restenosis after CEA has not yet been achieved; however, the present findings expand the current hypothesis that larger LSAs lead to an increased long-term restenosis risk [113], by demonstrating that other hemodynamic features besides low shear are independently linked to long-term restenosis. These features are obtained starting from the WSS topological skeleton and quantified by the WSS topological descriptors wFPA and TSVA. The statistical independence between both wFPA and TSVA and LSA in all three examined cohorts (reported in Table 7.2) suggests that these WSS topological skeleton features and low WSS represent different hemodynamic stimuli, possibly impacting differently the vascular response. Consistently, the co-localization of high $TSVI$ and high $RT\nabla_{x_{fp}}(e)$ regions with low cycle-average WSS regions was moderate for the post-CEA and healthy cohorts, and poor for the pre-CEA cohort (Figs. 7.2, 7.4 and 7.6), where a severe stenosis might induce a marked flow recirculation characterized by large variations in the WSS contraction/expansion action, high fixed points residence time, but concurrently relatively high cycle-average WSS. As a consequence of these observations, in principle the prediction of the long-term restenosis risk by hemodynamic analysis might be improved by taking into account not only the amount of time-averaged low shear [113], but also the introduced descriptors based on WSS topological skeleton. As previously reported on the same post-CEA cohort adopted here [113], the exposure to oscillatory WSS was not associated to IMT, thereby suggesting differences in the vascular response to focal (i.e., point-based) WSS oscillatory directional changes with respect to directional changes in the neighborhood of a point leading to variations in the contraction/expansion action.

On the other hand, although the different physical meanings underpinning the two WSS topological skeleton descriptors wFPA and TSVA (i.e., exposure to non-null values of the residence time of a fixed point, weighted by the local WSS contraction/expansion action vs. exposure to high normalized WSS divergence variability, respectively), a significant association between them emerged in all three cohorts (Table 7.2). This was consistent with the observed co-localization between luminal surface areas exposed to high $TSVI$ and $RT\nabla_{x_{fp}}(e)$ in all models (Figs. 7.2 and 7.4, respectively), with the former encompassing the latter. Consequently, fixed points occurred in regions where normalized WSS divergence variations were high (Fig. 7.2) and the contraction/expansion regions connecting fixed points were characterized by both high normalized WSS divergence absolute values and high normalized WSS divergence variations (Fig. 7.2). At 60 months after CEA, restenosis occurred in post-CEA carotid models PG1 and PG2, with diameter stenosis $>$ 70 % and $>$ 50 % respectively [113]. Notably, in the post-CEA cohort, PG1 was characterized by the highest wFPA value, while PG2 had the highest TSVA value (Figs. 7.2 and 7.4). Those two cases were also characterized by the highest LSA values in the post- CEA cohort, as can be seen in Fig. 7.6 and as previously reported [113], although using a different TAWSS threshold value to define LSA. A marked intima-media thickening was also observed [113] at 60 months follow-up in post-CEA patients PG3 and PC2 at the FD, PG6 in the CCA (FD-2 cm), in correspondence of either low cycle-average WSS (PG3, Fig. 7.6) or large variations in the WSS contraction/expansion and weighted fixed point residence times (7.2 and 7.4, respectively).

This study faces possible limitations. Among them, we mention differences between the CEA patients and healthy cohorts, mainly in terms of cohort size and mean age (72.8 $\pm$ 7.2 vs. 58.7 $\pm$ 11.8, respectively). These differences can be partially ascribed to the clinical real-world nature of the data adopted for the CEA cohorts, which however allowed to address the typical challenges related to longitudinal studies (e.g., long time-scale of the vascular pathophysiology processes, patients' recruitment and follow-up). Moreover, randomization was not performed for the selection of the CEA patients, and the exact extension of the region that underwent CEA surgical intervention (either with or without graft) could not be extracted from the imaging data. The relationships here reported might be influenced by the uncertainties (e.g., reconstruction errors) and assumptions/idealizations (e.g., Newtonian viscosity, rigid walls, as widely discussed elsewhere [126, 112]) affecting

computational hemodynamics. Because of these limitations, future investigations are warranted to further confirm the validity of the relationships presented here. Further investigations detailing and elucidating the effects of the WSS topological skeleton on vascular pathophysiology are encouraged. In this regard, the here applied Eulerian-based method for topological skeleton analysis confirms its potential as an effective biomechanical tool for increasing the chance of elucidating the mechanistic link between flow disturbances and clinical observations.

7.5 Supplementary Material

In violin plots of Figure 7.8, the distribution, median and quartile range are presented for the occurrence of cycle-average WSS fixed points in the bifurcation region for pre-CEA, post-CEA and healthy cohorts. In general, in the bifurcation region delimited by sections CCA3-ICA5-ECA2, the distribution of the different fixed points types in the three cohorts was markedly different, except for unstable nodes in pre- and post-CEA models (as highlighted by the shape of violin plots in Figure 7.8). More in detail, no cycle-average WSS fixed point was observed in two pre-CEA models (PG4 and PG8, Figure 7.1$and Figure$7.8) and in one healthy model (He4, Figure 7.1 and Figure 7.8), while all post-CEA models presented at least one cycle-average WSS fixed point. Focusing the analysis on the occurrence of saddle points, three pre-CEA models did not present any saddle point in the bifurcation region (PG4, PG7 and PG8, Figure 7.1 and Figure 7.8), while in the post-CEA cohort all models presented at least one saddle point. Considering the carotid bifurcations in the healthy cohort, on average they exhibited a higher number of saddle points in the bifurcation region than the other two cohorts (median number of saddle points in pre-CEA cohort: 1, post-CEA cohort: 3, healthy cohort: 4, Figure 7.1). Statistically significant differences emerged among the three cohorts in terms of occurrence of saddle points (Figure 7.8). Concerning the presence of cycle-average WSS stable foci in the bifurcation region, five pre-CEA models did not exhibit any (PG4, PG5, PG8, PC3 and PC4, Figure 7.1 in the main article and Figure 7.8). In consequence of the CEA, the number of stable foci in the bifurcation region increased or remained constant in eleven models, while it decreased to zero for two models (PC1 and PC2). Cycle-average WSS stable foci were observed in all but two healthy carotid models (He4 and He7). Statistically significant differences in the occurrence of stable foci emerged between the pre-CEA and healthy cohorts

($p = 0.026$, Figure 7.8). Unstable nodes were identified in the bifurcation region of one pre-CEA model only (PC1, Figure 7.1). After CEA, cycle-average WSS unstable nodes appeared in models PG1, PG6, PC4, and disappeared in model PC1. In the healthy cohort, unstable nodes were observed in a relatively larger number of models (39 out of 46) with respect to the other two cohorts. Consequently, statistically significant differences in the occurrence of unstable nodes emerged between the healthy cohort and both pre-CEA and post-CEA cohorts (Figure 7.8).

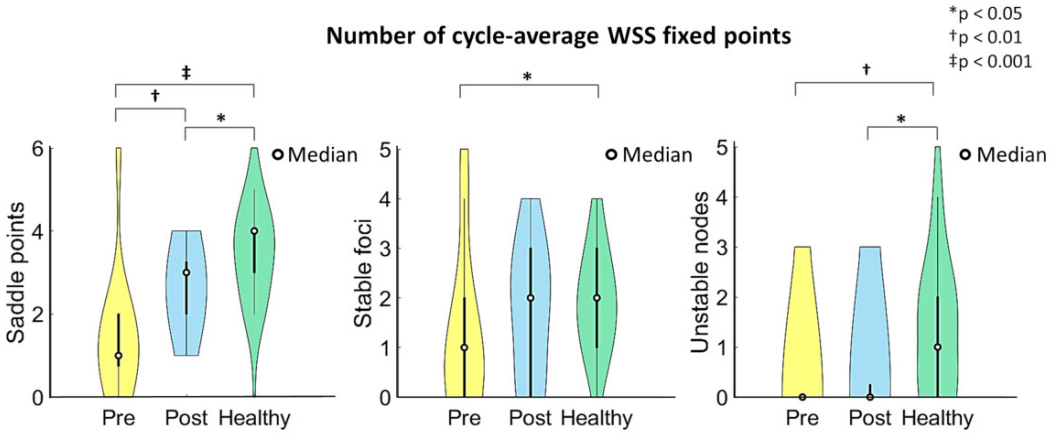

Figure 7.8: Violin plots of the occurrence of cycle-average WSS fixed points in the bifurcation region (delimited by sections CCA3-ICA5-ECA2) for pre-CEA, post-CEA and healthy cohorts. Differences among the three cohorts are evaluated with a Wilcoxon rank sum test.

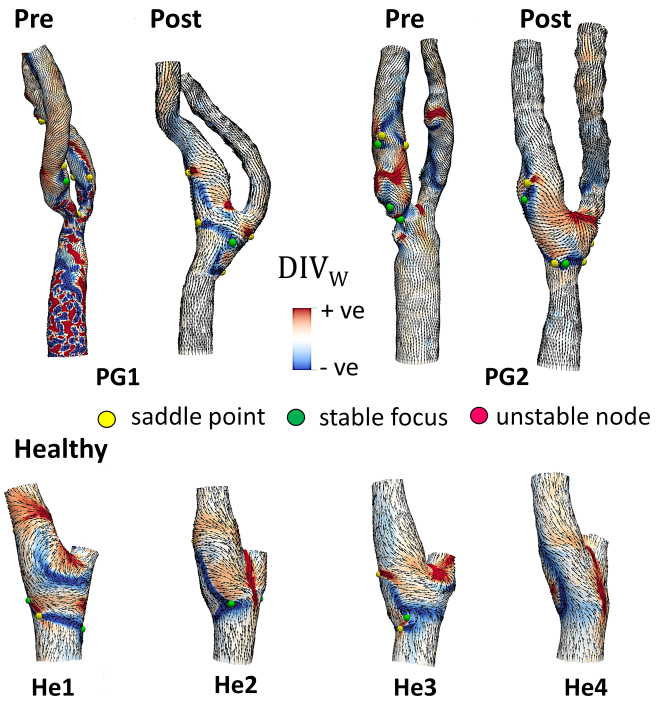

Figure 7.9: Topological skeleton of cycle-average WSS vector in selected pre-CEA (Pre), post-CEA (Post) and healthy cases. The topological skeleton in pre-CEA and post-CEA cohorts is extended beyond the bifurcation region to include in the pre-CEA models possible distal stenoses.

Figure 7.10: Luminal surface area exposed to high Topological Shear Variation Index ($TSVI$) value, as expressed by Topological Shear Variation Area (TSVA), in pre-CEA, post-CEA and healthy cohorts. The TSVA in pre-CEA and post-CEA cohorts is extended beyond the bifurcation region to include in the pre-CEA models possible distal stenoses. Red areas represent a $TSVI$ value above the 80^{th} percentile of the pooled $TSVI$ distribution of the healthy models in the bifurcation region.

Chapter 8

Deciphering Ascending Thoracic Aortic Aneurysm Hemodynamics in Relation to Biomechanical Properties

A version of this chapter has been published in:
Medical Engineering & Physics; 82: 119-129 , doi.org/10.1016/j.medengphy.2020.07.003, 2020
"Deciphering ascending thoracic aortic aneurysm hemodynamics in relation to biomechanical properties"
G. De Nisco, P. Tasso, K. Calò, V. Mazzi, D. Gallo, F. Condemi, S. Farzaneh, S. Avril, U. Morbiducci

8.1 Introduction

Ascending thoracic aortic aneurysm (ATAA) is an unphysiological localized ballooning of the aorta at the ascending segment proximal to the brachiocephalic trunk, which can grow in size and eventually rupture, leading to serious complications and death. The common clinical treatment of ATAA consists in surgical repair by replacing the diseased aortic segment with a synthetic graft. Due to significant mortality rates associated to prophylactic surgery (3-5 %) [127], indications for

surgical treatment depend on the estimated maximum aortic diameter, with a suggested critical threshold value of 5.5 cm (except for patients with Marfan syndrome) [128, 129, 130]. However, the diameter-based criterion for surgical intervention has been widely recognized as inadequate [131, 132]. To find complementary or alternative markers of ATAA risk of rupture, a plethora of studies have focused on, e.g., genetic, biological, structural and biomechanical factors involved in the ATAA wall dilatation/degeneration[133, 134, 135, 136, 137, 138, 139].

However, current evidence is still insufficient to rely on biomechanical factors alone [136, 138], and rather suggests a possible relation between ATAA hemodynamics and wall mechanical properties, which might better explain the complexity of ATAA development and progression. In particular, the analysis of aortic hemodynamics, with the as- sessment of distinguishable intravascular flow features and wall shear stress (WSS) distribution on the luminal surface as obtained from *in vivo* [140, 141, 142, 143] and patient-specific computational studies [144, 145, 146, 147, 148], has been suggested to derive markers of rupture risk, giving the supposed link between hemodynamic features and ATAA wall mechanical properties. For instance, previous follow-up studies reported a significant association between the luminal exposition to relatively low WSS values and ascending aorta wall weakening and dilatation in ATAA patients [147, 149, 150]. In this context, we propose a framework combining patient-specific computational fluid dynamics (CFD), advanced fluid mechanics analysis and personalized *in vivo* estimates of the local aortic stiffness.

The aims are to interpret the complex role played by local hemodynamics in ATAA and to decipher the existing links between near-wall features and ATAA wall stiffness. More specifically, changes in hemodynamics associated with pathologic aortic dilatation were analyzed by applying a recently proposed methodology on two subject-specific (1 healthy - 1 diseased) CFD models. The approach relies on the analysis of WSS vector field topological skeleton, essentially consisting of a collection of critical points (i.e., locations at the luminal surface of the vessel where the WSS vanishes), and special lines which separate the luminal surface into areas of different WSS behavior, ultimately identifying where an expansion/contraction action is exerted by WSS on the endothelium (which is expected to have biological relevance) [21]. Finally, ATAA local stiffness was obtained through a recently proposed inverse method based on gated CT scans [151]. Spatial correlations with WSS features were extracted from the topological skeleton analysis to ultimately

associate ATAA complex hemodynamic features and wall mechanical properties.

8.2 Methods

One 36 years old healthy subject with no history of cardiovascular diseases, and one 59 years old subject with bicuspid aortic valve (BAV), moderate aortic valve insufficiency and a 6.03 cm x 5.95 cm ATAA were enrolled in the study after informed consent. An overview of the methods applied in this study is provided in Figure 8.1 and detailed onwards.

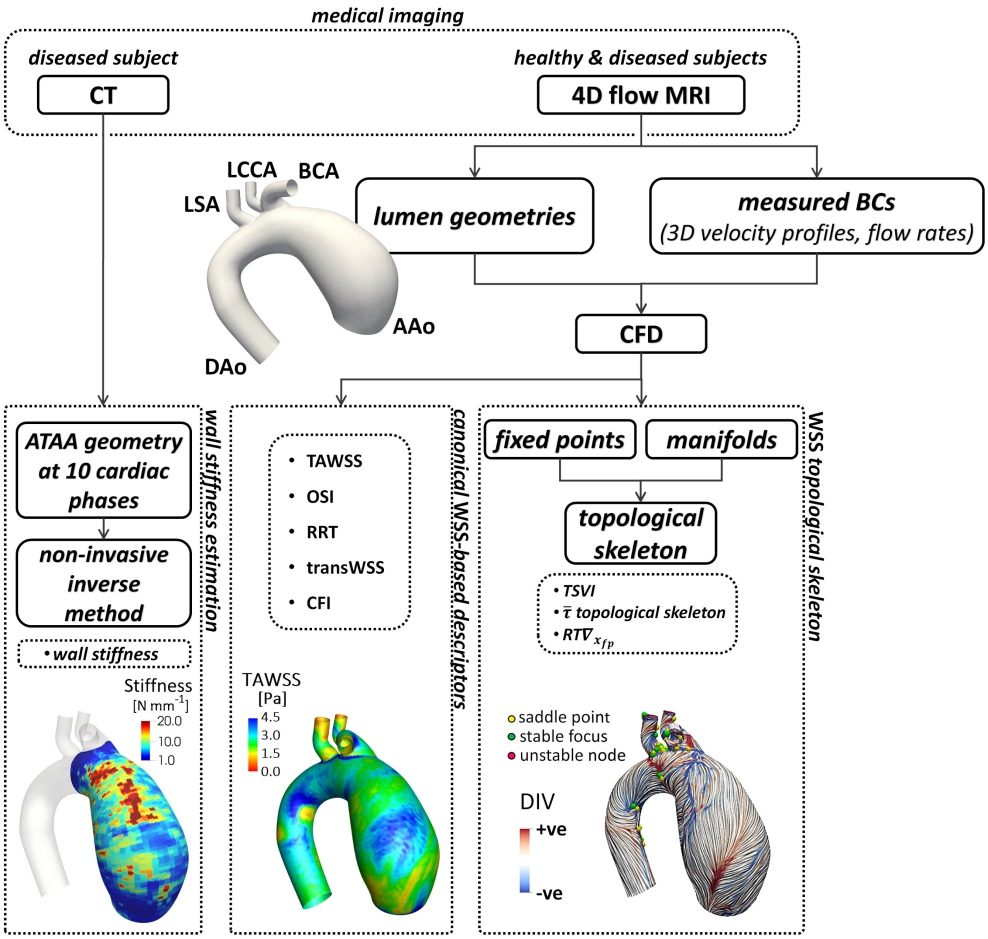

Figure 8.1: The diagram shows how imaging data contribute to define vessel geometry, hemodynamic variables and wall mechanical properties. BCs: boundary conditions; CFD: computational fluid dynamics; ATAA: ascending thoracic aorta aneurysm.

8.2.1 Medical imaging, geometry reconstruction and *in vivo* aortic wall stiffness estimation

The two subjects were imaged by a 3T MR scanner (Siemens Magnetom Prisma) without contrast agent, using the same 4D flow MRI protocol exhaustively detailed elsewhere [148]. Based on 4D flow MRI images, the 3D geometries of each subject were reconstructed using CRIMSON (CardiovasculaR Integrated Modelling and SimulatiON) [152]. The resulting geometries included the ascending thoracic aorta, the aortic arch, the descending thoracic aorta and the supra-aortic vessels (brachiocephalic artery - BCA, left common carotid artery - LCCA, and left subclavian artery - LSA, as shown in Figure 8.1). Additionally, the diseased subject underwent ECG gated CT imaging in order to identify ATAA wall local stiffness with a re- cently proposed inverse method [151] detailed below.
A recently proposed non-invasive inverse approach was ap- plied here to identify aortic wall stiffness for the diseased subject. Briefly, ATAA geometries at ten phases along the cardiac cycle, including diastolic and systolic phases, were (1) reconstructed from gated CT scans (resolution: 512 $\times$512, slice thickness = 0.5 mm) using MIMICS (v.10.01, materialise NV), and (2) meshed ensuring a set of nodes attached to the same material points at all the recorded cardiac phases [151]. Based on the Fourier series analysis of temporal changes in position of each node, the local strain distribution was reconstructed and the wall stiffness at every location was derived by satisfying the local equilibrium equation under the acting tensions. The strategy applied to estimate local wall stiffness *in vivo* is exhaustively detailed elsewhere [151].

8.2.2 Computational haemodynamics

The finite element-based code SimVascular (https://simvascular.github.io/) was adopted to solve the governing equations of fluid motion in the two models. In detail, the Navier–Stokes equations, in their discretized form and under unsteady flow conditions, were solved using a stabilized finite element method supporting the use of linear tetrahedral elements (P1–P1) in the SimVascular flow solver for velocity and pressure[153]. Newtonian blood rheology (with prescribed constant density and dynamic viscosity respectively equal to $1050\,kg\,m^{-3}$ and 0.0035 Pa s) and rigid wall with no-slip condition were assumed. To ensure a grid-independent solution, based on a mesh sensitivity analysis, an average tetrahedral element size

of $1.05 \cdot 10^{-3}\, m$ with a near- wall refinement consisting of 12 tetrahedral boundary layers with a decreasing ratio of 0.90 was adopted. The resulting computational grids consisted of 4.13 and 7.97 million elements for healthy and diseased model, respectively. Boundary conditions were prescribed using patient-specific 4D flow MRI measurements. In detail, measured fully 3D phase velocity data were extracted along the cardiac cycle and imposed in terms of Dirichlet inflow boundary conditions (BCs) at the ascending aorta (AAo) inlet section (as detailed in our earlier work [98]). As regards outflow BCs, 4D flow MRI measured flow rates were prescribed at the supra-aortic vessels [97] in terms of fully developed velocity profiles. A three element Windkessel model was prescribed as BC at the descending aorta (DAo) outlet section, by applying a 3D-0D coupling scheme [148, 152].
The three element Windkessel model components (i.e., the impedance $-Z_C$, the distal resistance $-R$, and the capacitor $-C$) were tuned as described by elsewhere [148], obtaining patient specific values for the healthy (Z_C= $1.36{\cdot}10^{7}\, kg\, m^{-4}\, s^{-1}$; R =$2.28{\cdot}10^{8}\, kg\, m^{-4}\, s^{-1}$; $C = 1.50{\cdot}10^{-8}\, kg^{-1}\, m^{4}\, s^{2}$) and the pathologic subject (Z_C= $5.32{\cdot}10^{6}\, kg\, m^{-4}\, s^{-1}$; R =$9.02{\cdot}10^{7}\, kg\, m^{-4}\, s^{-1}$; $C = 3.18{\cdot}10^{-8}\, kg^{-1}\, m^{4}\, s^{2}$). On the simulated flow fields in the healthy and diseased models, advanced post-processing tools, implemented with MATLAB ® (The MathWorks, Inc.) and Python, were applied to better decipher the aortic hemodynamics complexity.

8.2.3 WSS topological skeleton analysis

The proposed Eulerian method was here considered to analyze the topological skeleton of the WSS vector field across the aortic luminal surface. WSS manifolds were captured using the divergence of the normalized WSS vector, according to eq. (2.22). In details, negative values of DIV_W identify contraction regions, approximating attracting manifolds; positive values of DIV_W identify expansion regions, approximating repelling manifolds.
For the complete WSS topological skeleton extraction, the identification of WSS fixed points location at the luminal surface was performed by computing the Poincaré index. Then, the identified fixed points were classified using the eigenvalues of the Jacobian matrix, which provide information about fixed points nature. Technically, the adopted eigenvalue-based criterion allowed to distinguish between fixed point node or focus configurations (Table 2.1).
As a first step, here the WSS topological skeleton of the cycle-average WSS vector

field $\bar{\boldsymbol{\tau}}$ at the luminal surface of both the healthy and diseased model was analyzed. The unsteady nature of the WSS vector field fixed points along the cardiac cycle was investigated using the WSS fixed points weighted residence time along the cardiac cycle $RT\nabla_{x_{fp}}(e)$, according to eq. (3.10).
Additionally, here the quantity based on WSS divergence, named Topological Shear Variation Index ($TSVI$), was computed to measure the amount of variation in WSS contraction and expansion action exerted at the luminal surface of the vessel, according to eq (3.12).

8.2.4 canonical WSS-based hemodynamic descriptors

In addition to the WSS topological skeleton analysis, flow disturbances were evaluated here also in terms of canonical WSS-based descriptors (Table 1.1), namely the Time Average Wall Shear Stress (TAWSS), Oscillatory Shear Index (OSI) [108], and Relative Residence Time (RRT) [15]. Moreover, a descriptor of WSS multidirectionality was considered (Table 1.1), i.e., the transversal WSS (transWSS) [16], defined as the average WSS component acting orthogonal to the time-averaged WSS vector direction.

8.2.5 Aortic hemodynamics *vs.* wall stiffness

To investigate the existence of possible relations between ATAA hemodynamics and the mechanical properties of the aortic wall, an analysis of co-localization between exposure to "disturbed" hemodynamics *vs.* wall stiffness was carried out according to schemes proposed elsewhere [154, 155, 20]. More specifically, objective thresholds for WSS-based hemodynamic descriptors and for wall stiffness were identified as the 2^{nd} tertile of the respective luminal distribution (1^{st} tertile for TAWSS). The co-localization of luminal surface areas (SAs) characterized by stiffness and each one of OSI, RRT, transWSS, or $TSVI$ values higher (lower for TAWSS) than the respective thresholds was quantitatively assessed by the similarity index (SI) [20]

$$SI = \frac{2(\mathrm{SA}_{high\ stiffness} \cap \mathrm{SA}_j)}{\mathrm{SA}_{high\ stiffness} + \mathrm{SA}_j}, \tag{8.1}$$

with j indicating a generic WSS-based hemodynamic descriptor. SI ranges between 0 (the SAs have no spatial overlap) and 1 (the SAs are equivalent and perfectly spatially overlapped).

8.3 Results

8.3.1 ATAA wall stiffness in vivo estimation

The in vivo estimated local wall stiffness distribution on the AAo of the diseased subject is presented in Figure 8.2. Consistent with previous observations [156, 156], local variations in the wall mechanical properties are evident in the investigated model, where the highest values of the stiffness are observed at the outer AAo wall. For this reason, in order to investigate the possible role played by hemodynamic features in the development and progression of aneurysm disease, the analysis was here focused at the proximal AAo outer wall of both healthy and diseased models, where the biomechanical wall alteration mainly occurred in the ATAA subject.

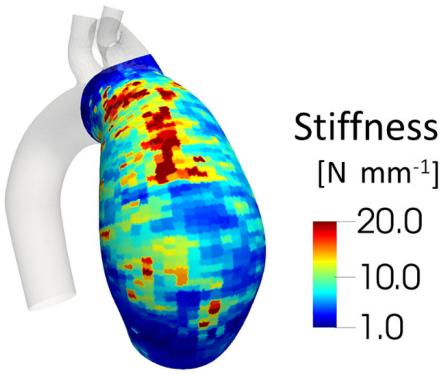

Figure 8.2: Estimated wall stiffness distribution at the luminal surface of ATAA model .

8.3.2 WSS topological skeleton analysis

Here the analysis of the WSS vector field topological skeleton at the aortic luminal surface was applied in a two-step strategy. As a first step, the aortic cycle-average WSS vector field topological skeleton was identified and analysed (Figure 8.3) aiming at identifying integral topological features differences between the healthy and ATAA model. It emerged that on both models a line of marked WSS expansion was located at the proximal AAo outer wall, as identified by positive DIV_W values.
However, the healthy aorta only presented there an unstable node. Moreover, marked contraction lines characterized the WSS topological skeleton on the ATAA

outer wall, but they were not present on the luminal surface of the healthy aorta. In the second step, the impact of the WSS vector field dynamics (along the cardiac cycle) on topological skeleton features was analysed. The analysis of the luminal surface distribution of fixed points weighted residence time ($RT\nabla_{x_{fp}}(e)$, Figure 8.3b) highlighted the presence of a wide region at the AAo outer wall of the diseased model where instantaneous WSS fixed points appear and reside for a longer fraction of cardiac cycle. Such region is surrounded by luminal regions with a high local WSS contraction/expansion strength. On the other hand, a completely different distribution was observed on the outer wall of the healthy model (Figure 8.3b), mainly characterized by low $RT\nabla_{x_{fp}}(e)$ values.
The analysis of the $TSVI$ luminal distributions (Figure 8.3c) highlighted that: (1) the highest local variations in the contraction/expansion action exerted by the WSS on the endothelium along the cardiac cycle are located at two distinct regions of the AAo outer wall luminal surface, in both healthy and diseased models; (2) in the diseased model, high $TSVI$ and high $RT\nabla_{x_{fp}}(e)$ regions are markedly co-localized on the outer wall luminal surface.

8.3.3 Aortic hemodynamics *vs.* wall stiffness

Here we assess the co-localization of the in vivo estimated wall stiffness at AAo outer wall of the ATAA model with the WSS topological skeleton-based quantities, and with canonical WSS-based descriptors of disturbed shear. A visual inspection of Figure 8.4 suggests that an association might exist between instantaneous WSS fixed points dynamics at the luminal surface and the aortic stiffness. Interestingly, instantaneous WSS fixed points undergo longer combinations of residence time and marked contraction/expansion strength of the WSS vector field (as expressed by the quantity $RT\nabla_{x_{fp}}(e)$) on those ATAA luminal surface areas where stiffness is high (Figure 8.4).
To explore more in depth the possible connections between peculiar WSS features and the altered biomechanical properties of the diseased aortic wall, the extent of the co-localization of high aortic wall stiffness regions with SAs exposed to presumably disturbed shear was quantified. By visual inspection of Figure 8.5a, it emerged that high stiffness co-localizes with high $TSVI$ better than with canonical WSS-based descriptors. Of note, it was observed that SAs exposed to low TAWSS

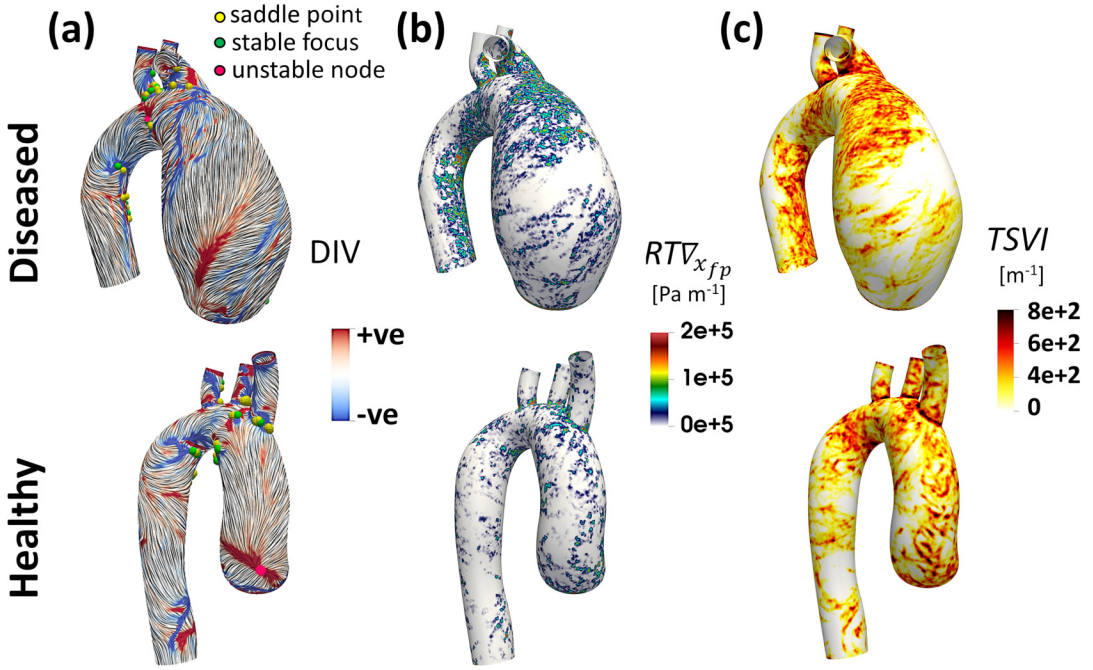

Figure 8.3: Aortic luminal distributions of (a) cycle-average WSS topological skeleton, (b) WSS fixed points weighted residence time $RT\nabla_{x_{fp}}(e)$, and (c) $TSVI$. The ATAA and healthy aortic models are displayed in the top and bottom panel, respectively

poorly co-localize with high stiffness regions. These observations were quantitatively confirmed by the SI values (Figure 8.5b), remarking the stronger capability of the WSS vector field divergence-based quantity $TSVI$ as indicator of altered arterial wall mechanical properties, than the canonical WSS- based descriptors. Indeed, $TSVI$ co-localizes with ATAA wall stiffness 206% more than TAWSS, 15% more than OSI and transWSS, and 45% more than RRT.

8.4 Discussion

Wall dilatation/degeneration of the ascending aorta is a complex multifactorial process promoted by a unique bio-chemo-mechanical environment, which may ultimately lead to aortic wall dissection/rupture [133, 134, 135, 136, 137, 138, 139]. Despite a large body of literature focused on the role played by individual biological, chemical, or biomechanical factors in the ATAA development [138], the heterogeneity characterizing ATAA disease cannot be exhaustively explained by

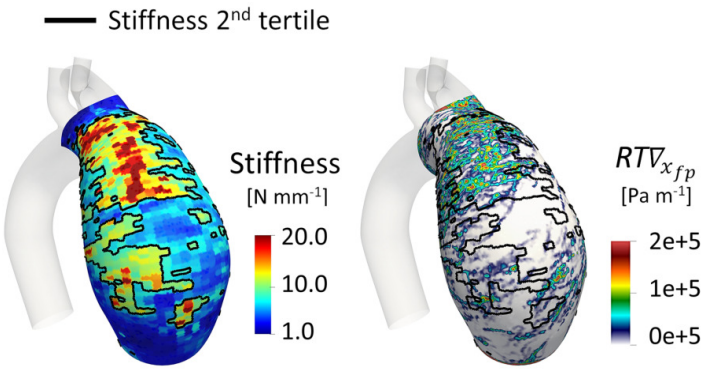

Figure 8.4: Contour maps of estimated wall stiffness (left) and WSS fixed points weighted residence time at the luminal surface of ATAA model. The black contour line represents the 2^{nd} tertile of stiffness luminal distribution at the ATAA outer wall.

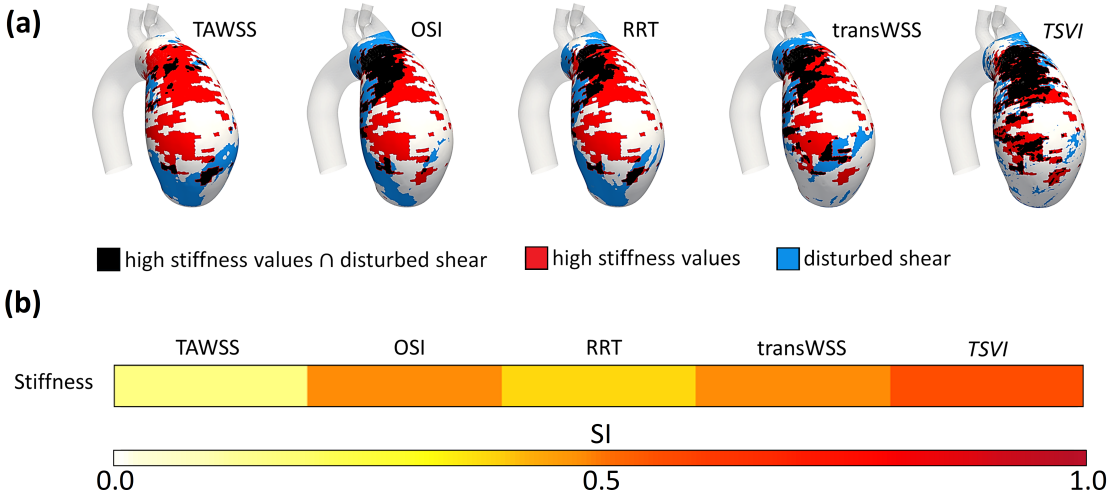

Figure 8.5: (a) Co-localization maps of high stiffness and disturbed shear; (b) similarity indices quantifying the co-localization of luminal SAs characterized by high stiffness and each descriptor of deranged hemodynamics (i.e., low TAWSS; high OSI, RRT, transWSS, $TSVI$).

individual features and the analysis of their complex interplay is still poorly investigated [136, 137, 138, 139]. In this context, here we aim to highlight the possible links between ATAA hemodynamics, obtained by CFD simulations and explored with advanced method, and *in* vivo estimated wall mechanical properties, inversely derived from gated CT scans [151]. The findings of this study confirm, on the

basis of an in-depth quantitative exploration, that the near-wall hemodynamic environment characterizing the ATAA model markedly differs from the healthy aorta. More in detail, the analysis of the WSS topological skeleton highlighted peculiar features on the ATAA outer wall, which are not or are poorly present on the luminal surface of the healthy ascending aorta (Figure 8.3), i.e.: (1) the presence of localized marked WSS contraction regions; (2) the appearance and persistence of instantaneous WSS fixed points along the cardiac cycle (as quantified by $RT\nabla_{x_{fp}}(e)$, which additionally weights the strength of the local contraction/expansion action exerted by the WSS); (3) a large luminal surface area undergoing marked variation in the WSS contraction/expansion action on the endothelium over the cardiac cycle (as indicated by $TSVI$).

The evidence emerged from the WSS topological skeleton analysis support the hypothesis that a complex interplay exists between hemodynamic features, aortic wall dilatation and its degradation in terms of wall mechanical properties. This statement is supported by the main finding of the study, i.e., that in the distal AAo outer wall of the ATAA model, extended high stiffness regions (indicating a degradation of the mechanical properties of the wall), co-localize with luminal surface areas of: (1) high instantaneous WSS fixed points residence time (weighted by WSS divergence value) (Figure 8.4); (2) large variations in the WSS contraction/expansion action exerted by the flowing blood along the cardiac cycle, here quantified by $TSVI$ (Figure 8.5). It is worth noting that the cross-sectional nature of this study does not allow to establish whether the observed hemodynamic features are responsible for wall dilatation and degradation, or whether they are consequence of the dilated geometry. However, previous studies suggested that altered aortic flow predisposes the ascending thoracic aorta to wall dilatation/degradation [147, 149] as a consequence of the purported role of endothelial shear in the pathogenesis of ATAA [157]. It is well known, in fact, that WSS has a relevant role in endothelial cells (ECs) function, gene expression and structure. Several studies have shown that WSS magnitude influences ECs morphology and orientation [157, 8] and may induce alteration of cellular functions regulating vascular homeostasis [8, 1]. Highly oscillatory patterns of WSS are also known to induce migration, proliferation and activation of transcription factors, as documented by in vitro studies [158, 159, 17]. Interestingly, previous investigations have also suggested how the WSS contraction/expansion action on the endothelium, highlighted by WSS manifolds, induces mechanical changes in ECs permeability [160] and could trigger focal pathological

vascular responses [21]. However, the role of WSS in the mechanical and rupture properties of the aortic wall in ATAA patients is still widely debated. Michel et al. [157] reported that low WSS values may promote the advection of plasma proteins through the aortic wall, which could eventually result in a decrease of elastic properties. On the other hand, low WSS has been associated to a decreased risk of ATAA rupture [161]. Moreover, previous evidences established that valve-mediated flow disturbances in ATAA patients with valvulopathy induce high peak WSS values on the outer aortic wall, potentially promoting adverse vascular remodeling [137, 162]. In particular, several studies reported associations between high WSS at the AAo and (1) elastin loss and regional aortic dysregulation of extracellular matrix [150], (2) elastic fiber thinning [140], and (3) higher concentration of circulating biomarkers (an hallmark of degradation of the extracellular matrix and increased wall stiffness) such as matrix metalloproteinase [163]. In this context, the findings of this study contribute to better elucidate the link between WSS and ECs biological response in ATAA disease, suggesting that future studies addressing the role of hemodynamics in the ascending thoracic aorta wall dilatation/degradation should include descriptors based on the WSS topological skeleton, such as $TSVI$ (Figure 8.5). In fact, such descriptors show a higher co-localization with regions at the aortic wall characterized by high stiffness than canonical WSS-based descriptors. The hemodynamic quantities presented here may improve the prediction of ATAA development and progression and contribute to a deeper understanding of the underlying hemodynamics-driven processes. In general, the use of advanced method as the one here applied to better decipher the aortic hemodynamics can be extended to all cardiovascular flows to further elucidate the possible link between flow disturbances and vascular mechanobiology.

Several limitations could weaken the findings of this study. The main limitation is that the present analysis is based on only one ATAA model and one healthy aorta model. For this reason, we acknowledge that the here reported association between the WSS topological skeleton-based descriptor $TSVI$ and ATAA wall weakening indicator should be confirmed on a larger dataset. The inverse approach here adopted to estimate local wall stiffness in vivo does not take into account the presence of surrounding tissue. Such simplification may lead to an overestimation of the local stiffness [151, 164, 165, 166] especially where the aortic wall radial motion is majorly constrained, like in the region where the AAo inner wall is in close contact

with the pulmonary artery. Due to the potential unreliability of the stiffness estimation in this region, the AAo inner wall was not considered for the analysis. The adopted stiffness estimation technique is also based on the assumption that the aortic wall behaves as a membrane with no through-thickness shear[151, 167]. The regions near the supra-aortic branches may not satisfy such assumption and were therefore excluded from the wall stiffness analysis. Moreover, in the perspective of extending the analysis of aortic stiffness at different stages of ATAA growth, an extensive use of the inverse approach may be limited by the use of X-ray during the gated CT scans procedure. In this regard, other techniques, such as ultrasounds [168] or MRI [169], may be adopted as a source of dynamic images of the aortic wall during the cardiac cycle. Finally, the main limitation regarding the numerical settings of the CFD study is represented by the rigid wall assumption. However, recent observations have demonstrated that aortic wall motion has a minor impact on WSS-based descriptors of disturbed shear, and on intravascular flow topology. Concerning the latter, for example, similar helical fluid structures have been observed in vivo [60, 61, 170] and in vitro both in rigid and distensible aortic phantoms [171, 172]. Therefore, we believe that the assumption on aortic wall distensibility does not entail the generality of the present results.

Chapter 9

Wall Shear Stress Topological Skeleton Features in Image-Based Stented Coronary Bifurcation Models

9.1 Introduction

Coronary stents are tube-shaped devices expanded inside an atherosclerotic coronary artery aiming at restoring the correct blood flow to the heart. The implantation of the coronary stent leads to a new local fluid dynamics generated by the protrusion of the stent struts inside the lumen. A large body of literature has highlighted that local blood flow disturbances may play a fundamental role in the pathophysiological trajectories leading to stent failure, e.g., in-stent restenosis [173, 174]. The Wall Shear Stress (WSS), the frictional force per unit area exerted by the streaming blood on the luminal surface, has been shown to be an important factor in the pathobiology of in-stent restenosis [175]. In vitro experiments have demonstrated a direct action of the WSS on endothelial cell morphology, function and orientation [176]. Moreover, it has been recognised that WSS action on the endothelium represents a stimulus to neointimal hyperplasia process, i.e., the excessive growth of tissue inside the stented region, through the production of abnormal stresses on the endothelial cells[177].

Notwithstanding the growing research interest in stented artery hemodynamic features as predictors of stent failure, how local hemodynamics influence flow-related processes leading to in-stent restenosis is still not completely understood. In this context, to improve and extent the current understanding of the association between local hemodynamics and vascular diseases, a marked interest recently has emerged on Wall Shear Stress (WSS) vector field topological skeleton analysis. Based on dynamical system theory, the topological skeleton of the WSS is composed by fixed points and their connections, called stable/unstable manifolds [22, 21]. A fixed point is a focal point where the WSS vanishes, and unstable/stable manifolds are contraction/expansion regions linking fixed points. Such an interest arises from the ability of WSS topological skeleton features to reflect cardiovascular complexity, with direct links to near-wall flow stagnation, separation, and recirculation, flow features which are usually classified as disturbed flow, known to be promoting factors for vascular diseases onset and progression, such as in-stent restenosis in coronary arteries [21].
The present study explores the WSS topological skeleton features in image-based computational fluid dynamics (CFD) stented coronary artery models replicating the complete clinical procedure of stent implantation performed in clinical practice [174]. The final aim is to investigate the possible involvement of WSS topological skeleton features in the processes leading to stent failure. To do that, the here proposed Eulerian-based method for the analysis of the topological skeleton of the WSS vector field is applied.

9.2 Computational haemodynamics

The two cases (i.e., CASE A and B) of pathologic Left Anterior Descending (LAD) artery with bifurcations treated with the provisional stenting technique considered here have been already partially presented elsewhere [174]. In CASE A, a Xience Prime stent by Abbott Vascular (nominal diameter of 3 mm, length of 28 mm and strut thickness of 81 μm), was implanted. In CASE B, two Endeavor Resolute stents by Medtronic (nominal diameter of 2.75 mm, length of 15 mm and strut thickness of 91 μm) were implanted. Pre-operative vessels were reconstructed combining conventional angiography and computed tomography angiography data [174], and structural finite element analyses replicating the clinical stenting procedures were used to obtain the post-operative, stented fluid domains [174]. A hybrid

discretization strategy using both tetrahedral and hexahedral elements was adopted [174], aiming at reducing computational time. In detail, an internal cylinder, created inside both models following the centre line of the main branch, was discretized using hexahedral elements. Tetrahedral elements were used to discretize the region between the cylinder and the wall, and a layer of pyramidal elements was created at the interface between the two meshes. Transient CFD simulations were performed using a finite-volume based code, applying a pulsatile flow waveform representative of the human LAD as inflow boundary condition. The non-Newtonian nature of the blood flow was taken into account considering the Carreau model and rigid wall with the no-slip boundary condition was assumed. Additionally, two transient simulations in the two non-stented geometries were performed. Exhaustive details on the computational settings are provided elsewhere [174].

9.3 WSS topological skeleton analysis

The WSS topological skeleton analysis was performed by considering the proposed Eulerian-based method. Briefly, based on Volume Contraction theory, it has been demonstrated that the divergence of the normalized WSS vector field, as defined in eq. (2.22), can be used to easily identify the connections between WSS fixed points, i.e., WSS manifolds. Technically, negative values of DIV_W identify contraction regions approximating attracting manifolds, while positive values of DIV_W identify expansion regions approximating repelling manifolds. To complete the WSS topological skeleton analysis, WSS fixed points were identified and classified by computing Poincaré index and eigenvalues of the Jacobian matrix respectively, according to the scheme described in Section 3.2.
First, the WSS topological skeleton of the cycle-average WSS vector field at the luminal surface of was analysed.
Subsequently, the unsteady nature of WSS fixed points and manifolds along the cardiac cycle was characterized. The quantity based on WSS divergence, named Topological Shear Variation Index ($TSVI$), i.e., the root mean square deviation of the divergence of the normalized WSS with respect to its average over the cardiac cycle, as defined in eq. (3.12) in Section 3.3, was here adopted. Roughly speaking, $TSVI$ measures the local amount of variation in WSS contraction/expansion action exerted along the cardiac cycle on Endothelial Cells (ECs) lining the luminal surface of a vessel.

In addition, the unsteady nature of the WSS fixed points along the cardiac cycle was here analysed by computing the WSS fixed points weighted residence time ($RT\nabla_{x_{fp}}(e)$), according to eq. (3.10) in Section 3.3. Roughly speaking, (3.10) measure allows to quantify the fraction of cardiac cycle a generic triangle mesh surface element on the vessel luminal surface hosted a fixed point, weighting the residence time by the strength of the local contraction/expansion action.

9.4 Results

The geometry of the two stented coronary artery models analysed in the present study is presented in Figure 9.1, where two insets are displayed aiming at zooming the malapposition region for CASE A and the overlapping zone between two stents for CASE B. It is recognised that (1) a malapposed stent strut, i.e., when it is not in contact with the vessel wall, can affect local blood flow and WSS profile [178] and (2) stent overlap is associated with increased risk of adverse clinical outcome [179].The cycle-average WSS topological skeleton, the $TSVI$ distribution and the $RT\nabla_{x_{fp}}(e)$ distribution along the luminal surface for stented CASE A and B are displayed in Figures 9.2 and 9.3, respectively. In both cases, cycle-average WSS fixed points were mostly located at the luminal surface in correspondence with stent peaks. Moreover, cycle-average WSS fixed points were located at the luminal surface close to all strut connectors in CASE A (Figure 9.2A) and in the overlapping region between the two stents in CASE B (Figure 9.3A). Both stented cases were characterized by cycle-average WSS contraction regions, identified by negative DIV_W values, located at immediately upstream struts regions and WSS expansions regions, identified by positive DIV_W values, located at immediately downstream struts regions. Interestingly, a completely reverse DIV_W distribution can be observed in the stent malapposition region for CASE A (Figure 9.2A) and in the overlapping zone between two stents for CASE B (Figure 9.3A). $TSVI$ maps highlighted that marked variations in the WSS contraction/expansion action exerted on the endothelium along the cardiac cycle were mainly located at the luminal surface in correspondence with stent peaks and close to all the struts in both models. The highest $TSVI$ values were located at the bifurcation, in the stent malapposition region and close to stent connectors for CASE A (Figure 9.2B), and at the stents overlapping region for CASE B (Figure 9.3B). The analysis of the luminal surface distribution of instantaneous WSS fixed points weighted residence time along the

cardiac cycle (Figure 9.2C for CASE A and Figure 9.3C for CASE B) suggested that instantaneous WSS fixed points appear and reside for a longer fraction of cardiac cycle at the luminal surface in correspondence with stent peaks. A marked co-localization can be observed between high values of $RT\nabla_{x_{fp}}(e)$ (Figure 9.2C for CASE A and Figure 9.3C for CASE B) and location of cycle-average WSS fixed points (Figure 9.2A for CASE A and Figure 9.3A for CASE B), suggesting a quasi-static behaviour of the WSS fixed points along the cardiac cycle. In fact, no instantaneous WSS fixed points appear inside each repeating stent cell along the cardiac cycle for both cases.

To appreciate the hemodynamic impact of the stenting procedures, the cycle-average WSS topological skeleton, the $TSVI$ and the $RT\nabla_{x_{fp}}(e)$ distribution along the luminal surface of the non-stented model CASE A and CASE B are displayed in Figure 9.4A and in Figure 9.4B, respectively. In non-stented models cycle-average WSS saddle points, cycle-average WSS contraction/expansion regions, high $TSVI$ values and high $RT\nabla_{x_{fp}}(e)$ values were located only at the bifurcation regions, and in the proximal region CASE A, where the vessel presents marked curvature and tortuosity.

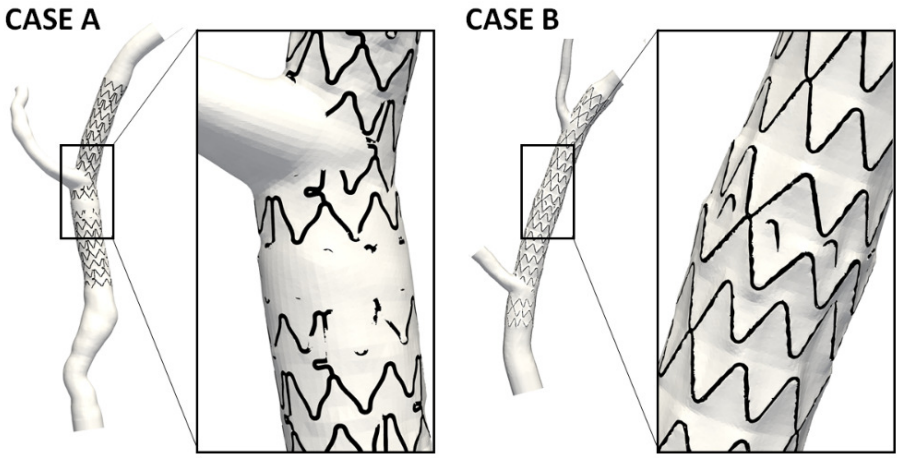

Figure 9.1: Geometry of the two stented coronary artery models. CASE A is displayed in the left panel and CASE B in the right one. Regions where the stent struts are in contact with the wall are black colored. The malapposition region for CASE A the overlapping zone between two stents for CASE B are highlighted.

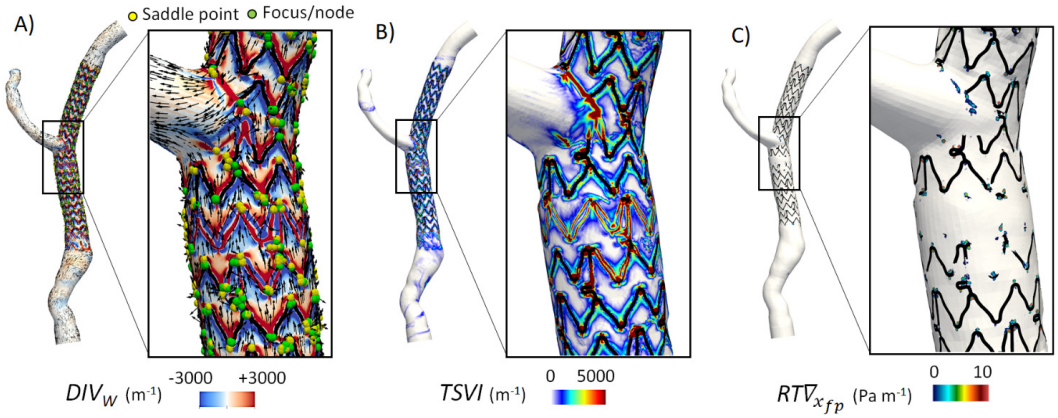

Figure 9.2: A) Cycle-average WSS topological skeleton, B) $TSVI$ and C) $RT\nabla_{x_{fp}}(e)$ distribution on the luminal surface for CASE A with stent. Regions where the stent struts are in contact with the wall are black colored.

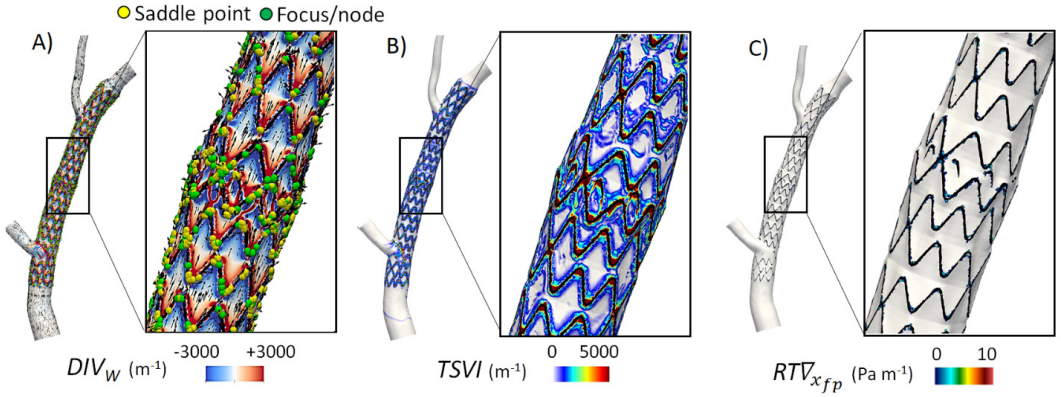

Figure 9.3: A) Cycle-average WSS topological skeleton, B) $TSVI$ and C) $RT\nabla_{x_{fp}}(e)$ distribution on the luminal surface for CASE A with stent. Regions where the stent struts are in contact with the wall are black colored.

9.5 Discussion

The present study aims to improve the current understanding of the impact of local hemodynamics on the flow-related processes leading to restenosis in coronary arteries, by applying a WSS topological analysis on two image-based stented coronary artery models. Here, we investigated for the first time the role of the WSS topological skeleton features in processes leading to in-stent restenosis in coronary arteries by applying a Eulerian-based WSS topological analysis.

From the present study, it emerged that WSS topological skeleton features are mostly located at the luminal surface in correspondence with stent peaks, close to

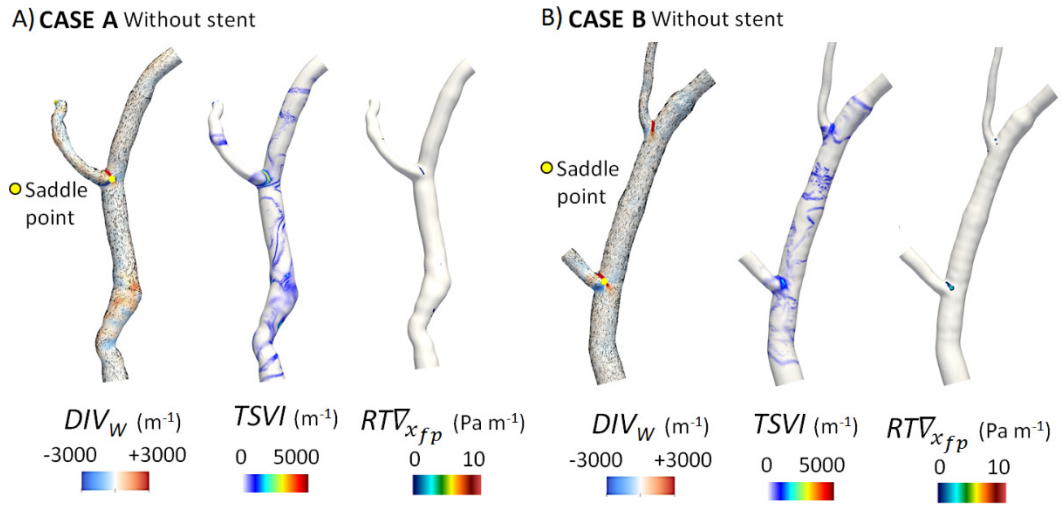

Figure 9.4: Cycle-average WSS topological skeleton and $TSVI$ and $RT\nabla_{x_{fp}}(e)$ distribution on the luminal surface for A) CASE A and for B) CASE B without the presence of stent.

all strut connectors, in the stent malapposition zone, and in the overlapping zone between two stents, suggesting that these regions are more prone to the risk of restenosis. Moreover, the findings of this analysis suggest that WSS topological skeleton features could represent a hemodynamic cue promoting coronary in-stent restenosis, in addition to the well-established low WSS. In detail, the luminal exposure to the high variability in the contraction and expansion action exerted by WSS (biomechanically described by $TSVI$) could induce a recurring variation in intracellular tension (acting e.g., on cell roundness) [180] and intercellular tension (e.g., increasing propagation of tension acting on junctions directionality)[181], with consequences on the endothelium permeability. Moreover, WSS contraction and expansion regions surrounding the stent struts could be linked to the EC migration and accumulation process observed in experimental studies [182], with WSS contraction action co-localized with ECs migration upstream from stent struts and WSS expansion action co-localized with ECs accumulation immediately downstream from stent struts [182].
In conclusion, the presented approach might contribute to a deeper understanding of the hemodynamics-driven processes underlying in-stent restenosis in coronary arteries.

Chapter 10

The Variability of the Shear Stress Contraction/Expansion Action Contributes to Wall Thickness Change in Coronary Arteries

This study has been performed in collaboration with Erasmus University Medical Center.

10.1 Introduction

There is ample evidence that a complex interplay of biological, biomechanical, and systemic factors is at the basis of coronary atherosclerosis onset and development [75, 12]. In particular, among the biomechanical factors, local hemodynamics is recognized as a major promoter of the initiation and progression of the atherosclerotic disease in coronary arteries, although its role is still not completely understood [183]. A large body of literature has supported the consistency of the 'hemodynamic risk hypothesis' in coronary disease, emphasizing the crucial and multifaceted role played by wall shear stress (WSS) in conditioning the initiation, localization, and growth of coronary lesions [184, 185]. In this scenario, an arsenal of hemodynamic descriptors has been proposed as markers of flow disturbances [186, 187, 188], aiming at quantifying the impact of different WSS features in promoting coronary atherosclerosis initiation/progression, inducing focal endothelial

dysfunction and inflammation [185], and affecting local blood-to-wall mass transfer rates [189, 190]. Low/oscillatory WSS has become the consensus hemodynamic mechanism for coronary atherosclerosis [75, 12, 183, 74, 108], with recent evidences attributing a role for multidirectional WSS in coronary plaque progression and changes in plaque composition [191, 192]. However, these WSS features may describe only partially the biomechanical stimulus affecting coronary atherosclerosis evolution. Moreover, the emerged weak-to-moderate capability of low, oscillatory or multidirectional WSS to identify/predict coronary lesion localization and development may indicate that a more complex mechanistic action of the shear forces on the endothelium is likely. In addition to this incomplete picture, a very recent study suggested a role for the shape of WSS time histories in the biological events leading to coronary atherosclerosis [193].

In this regard, a marked interest has recently emerged on the topological skeleton analysis applied to WSS vector field [21]. The WSS vector field topological skeleton consists of fixed points, where the WSS vector vanishes, and the regions connecting them (WSS manifolds), where the WSS vector field contracts or expands. The interest in such analysis is dictated by the fact that: (1) it is instrumental in identifying flow features usually classified as biomechanical events (e.g. flow stagnation, recirculation and separation), in the sense that they have been put in relation with "aggravating" biological events involved in atherosclerosis initiation/progression [21]; (2) it can be used to quantify the contraction/expansion action exerted by the WSS on the endothelium.

This study tests the ability of WSS topological skeleton features to predict the temporal evolution in coronary artery wall thickness (WT), a hallmark of atherosclerosis development, in an atherosclerotic pig longitudinal study [192, 154, 155]. To do that, WSS topological skeleton features were obtained from personalized computational hemodynamics simulations, adopting the proposed Eulerian-based method, and compared to changes in WT over time, measured *in vivo*. The final aim is to probe whether fluid mechanic quantities giving a direct measure of the variability of the contraction/expansion action exerted by the blood flow on the endothelium are capable to account for longitudinal local WT changes, by virtue of the theoretically robustly link to those flow disturbances deemed responsible for atherosclerosis initiation and progression.

10.2 Materials and Methods

An overview of the methods is provided in Figure 10.1

10.2.1 Animal population and imaging

Adult familial hypercholesterolemia Bretoncelles Meishan mini-pigs (N=3) with a low-density lipoprotein receptor mutation were put on a high fat diet to trigger atherosclerosis development. The three main coronary arteries (Left Anterior Descending (LAD), Left Circumflex (LCX), and Right Coronary Artery (RCA)). CCTA and IVUS acquisitions were performed at 3 months (T1, considered as the baseline in this study), at an average of 8.6 months (T2, respectively 9.8, 8.3, and 7.8 months for pig A, B and C in Figure 10.2), and at an average of 10.6 months (T3, respectively 14, 9.4, and 8.5 months for pig A, B and C) after the start of the diet. Combowire Doppler (Volcano Corp., Rancho Cardova, CA, USA) flow velocity measurements were acquired in each artery at the inflow section and immediately upstream and downstream of each side branch, at T1 and T2, as reported in detail in previous studies [192, 154, 155]. The study, performed according to the National Institute of Health guide for the Care and Use of Laboratory animals [194], obtained the ethical approval from the local animal ethics committee of the Erasmus MC (EMC nr. 109-14-10).

10.2.2 Plaque growth measurements

Quantitative analysis of wall thickness (WT) was carried out using the QCU-CMS software (version 4.69, Leiden University Medical Centre, LKEB, Division of Image Processing). In detail, for each coronary vessel (3 LAD, 3 LCX and 3 RCA), maps of local WT were obtained on IVUS images at T1, T2, and T3 by using a semi-automatic method for the lumen and vessel wall contour detection [192, 155]. Technically, WT was locally measured by subtracting the distance value between lumen centroid and lumen contour to the distance value between lumen centroid and outer wall contour (Figure 10.1). WT measurements were averaged over 3mm/45 degrees sectors of the luminal surface, to analyse their possible relation with hemodynamics, according to previous studies [192, 155].

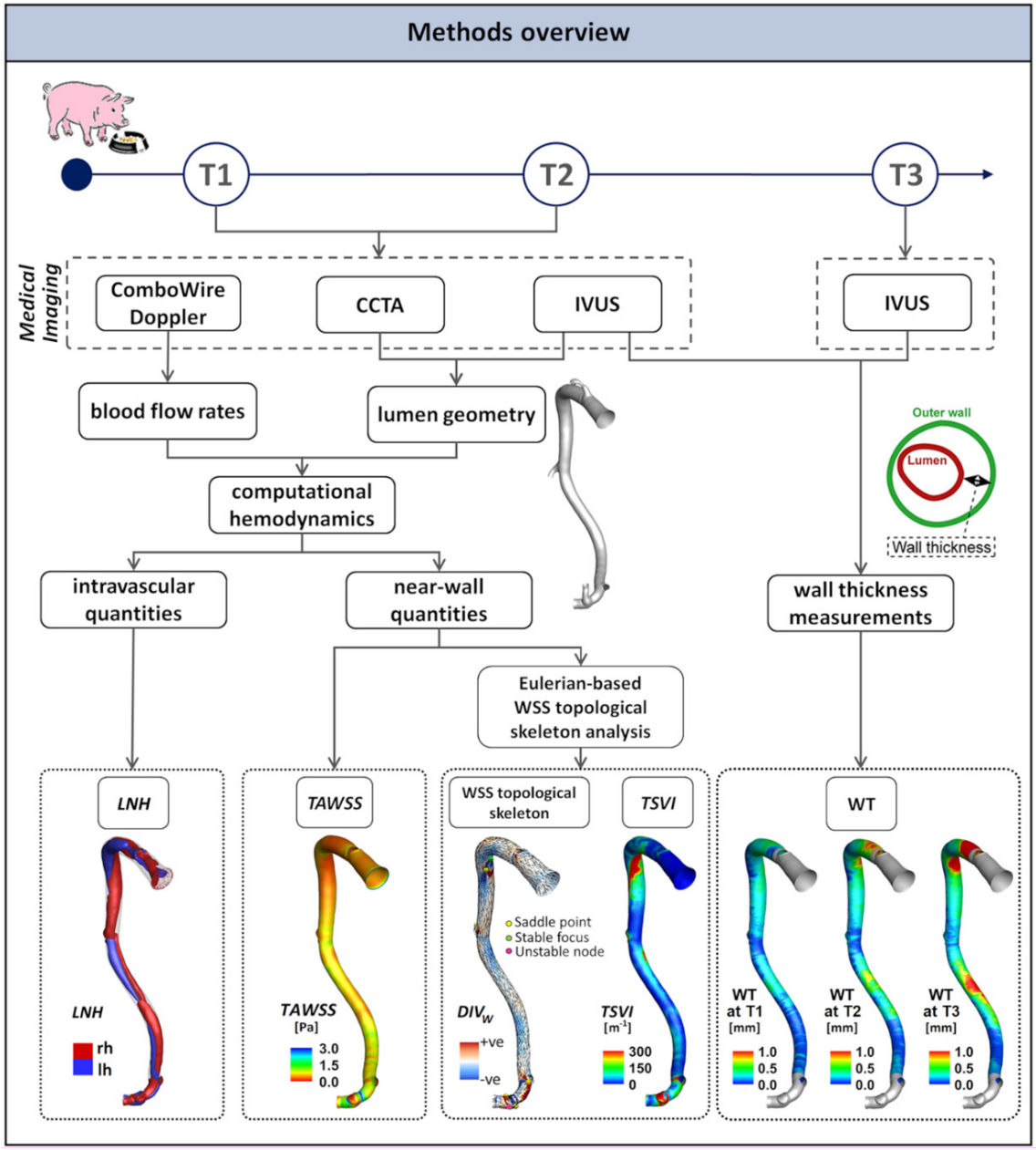

Figure 10.1: Schematic diagram of the study design, showing how imaging data contribute to define vessel geometry, hemodynamic variables, and wall thickness measurements. CCTA: coronary computed tomography angiography; IVUS: intravascular ultrasound; WT: wall thickness; LNH: local normalized helicity; rh: right-handed helical blood structure; lh: left-handed helical blood structure.

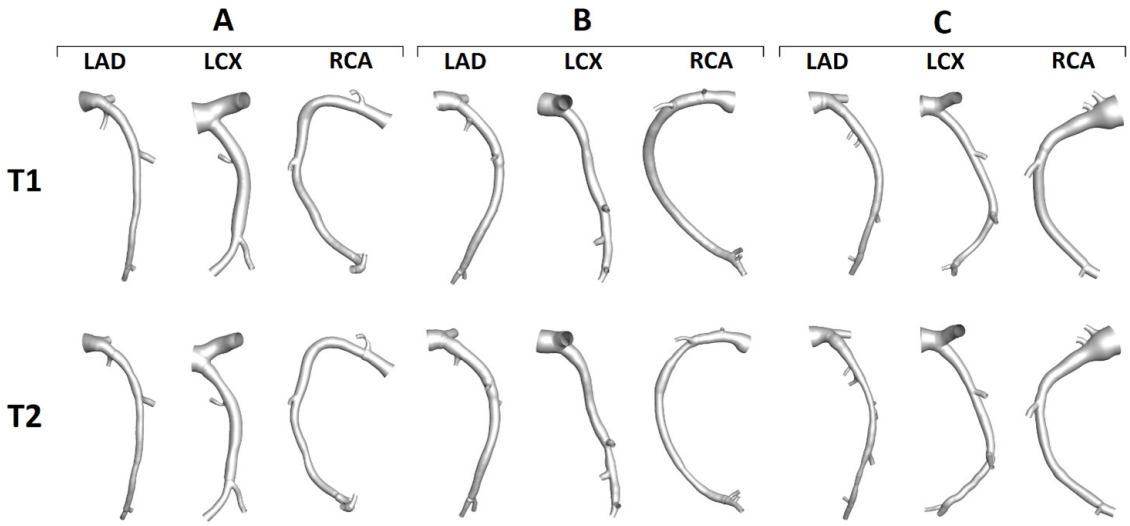

Figure 10.2: Geometry of the 9 swine coronary artery models at T1 and T2 of the follow-up time. Labels from A to C identify a single swine. For each swine, LAD, LCX and RCA geometries were reconstructed.

10.2.3 Computational hemodynamics

The 3D geometry of each coronary artery was reconstructed at T1 and T2 (N=18) by aligning the segmented (using Mevislab, Bremen, Germany) IVUS lumen contours along the centreline extracted from the corresponding 3D geometry reconstructed from CCTA. The resulting geometries are displayed in Figure 10.2. The three animals were named as pig A, B and C. Details on 3D geometry reconstruction are extensively reported elsewhere [154]. The reconstructed geometries were discretized, and unsteady-state CFD simulations were performed to characterize coronary hemodynamics (Figure 10.1). The governing equations of fluid motion were numerically solved by using the finite volume method. Blood was assumed as an incompressible, homogeneous, non-Newtonian fluid [195]. No-slip condition was assumed at the arterial wall. Individual in vivo ComboWire Doppler velocity measurements were used to derive personalized boundary conditions according to the following strategy: (1) the inlet flow rate was estimated from the most proximal Doppler velocity measurement, and prescribed as inlet boundary condition in terms of time-dependent flat velocity profile; (2) the perfusion of side branches was quantified as the difference between Doppler velocity-based flow rate measurements taken upstream and downstream of each side branch and applied as outflow condition in terms of measured flow ratio. If velocity-based flow measurements were

inaccurate or not available, a diameter-based scaling law [196] was applied to estimate the flow ratio at the outflow section [192, 154]. Descriptive notes on CFD settings are extensively detailed elsewhere [192, 155], are briefly reported in the Supplementary Materials.

10.2.4 WSS topological skeleton analysis and helical flow features

The WSS vector field ($\boldsymbol{\tau}$) at the luminal surface of each coronary model, obtained as an output of the CFD simulations, was analysed. In particular, the features of the WSS topological skeleton were investigated by applying the proposed Eulerian-based approach. We briefly remind that the WSS topological skeleton consists of fixed points, i.e., points where WSS is equal to zero, and stable/unstable manifolds linking fixed points. Translating the content of the dynamical systems theory to cardiovascular flows, stable/unstable manifolds identify patterns of the WSS vector field exerting an expansion/contraction action onto the luminal surface of the vessel. As described in Section 3.1, the WSS spatial contraction/expansion configuration patterns were here identified through the divergence of the normalized WSS vector, according to eq. (2.22). The Poincaré index was considered for WSS fixed points identification. Then, the eigenvalues of the Jacobian matrix were used to classify the fixed point as: (1) a sink, if it attracts nearby trajectories; (2) a source, if it repels nearby trajectories; (3) saddle point, if it attracts and repels nearby trajectories along different directions. In addition, based on the demonstrated physical meaning of eq. (2.22), the amount of variation in the WSS contraction and expansion action exerted on the endothelium along the cardiac cycle was here quantified by adopting the quantity Topological Shear Variation Index ($TSVI$), defined as the root mean square deviation of the divergence of the normalized WSS with respect to its average over the cardiac cycle, according to eq. (3.12).

To complement the analysis of the WSS topological skeleton, the luminal distribution of time-averaged wall shear stress (TAWSS) magnitude along the cardiac cycle was also evaluated (according to eq. (1.1)), as the exposure to low TAWSS values is widely recognized as a promoter of atherosclerotic disease [183]. In Figure 10.3 explanatory examples of different flow environments at the luminal surface of an artery are depicted aiming at highlighting differences between $TSVI$ and TAWSS

descriptors. In particular, the figure shows that: (1) the TAWSS value computed in a point at the luminal surface depends solely on the magnitude of the WSS vector applied to such point along the cardiac cycle; (2) the $TSVI$ value computed in a point depends on the instantaneous WSS vector field configuration in a neighbourhood of such point along the cardiac cycle. The WSS-based quantities were averaged over the same 3mm/45 degrees sectors at the luminal surface as the WT data.

Finally, as suggested by evidences on the atheroprotective role played by helical blood flow [154] and on its beneficial impact on atherosclerotic plaque development [197], a possible link between the WSS topological skeleton and helical flow features was qualitatively investigated. The intention was to clarify whether WSS topological skeleton features reflect the presence of intravascular flow patterns inversely associated with low WSS and WT in coronary arteries [154, 155]. To do that, the local normalized helicity (LNH) [198], given by:

$$\mathrm{LNH} = \frac{\boldsymbol{v} \cdot \boldsymbol{\omega}}{|\boldsymbol{v}| \cdot |\boldsymbol{\omega}|} = \cos\gamma, \tag{10.1}$$

where γ is the angle between local velocity $\boldsymbol{v}$ and vorticity $\boldsymbol{\omega}$ vectors, was used to visualize right- and left-handed helical blood flow patterns (positive and negative LNH values, respectively [197, 98]) inside the coronary artery models [60].

10.2.5 Statistical analysis

The existence of possible relations between near-wall hemodynamic features and measured WT data was investigated in terms of odds ratio, a statistical measure of the strength of the association between two events. More in detail, we classified as hemodynamically relevant the luminal surface sectors exposed to low or high values of the WSS-based hemodynamic descriptors, identifying, as artery-specific thresholds, the 20^{th} and the 80^{th} percentiles of the WSS-based descriptors distribution, respectively. The combination of WSS-based descriptors pairs was also investigated by considering the luminal surface sectors where both descriptors were classified as hemodynamically relevant. To determine the odds ratio, coronary artery WT values were divided into low, mid or high based on a vessel-specific tertile division [192, 154, 155]. Statistical significance was assumed for $p < 0.05$.

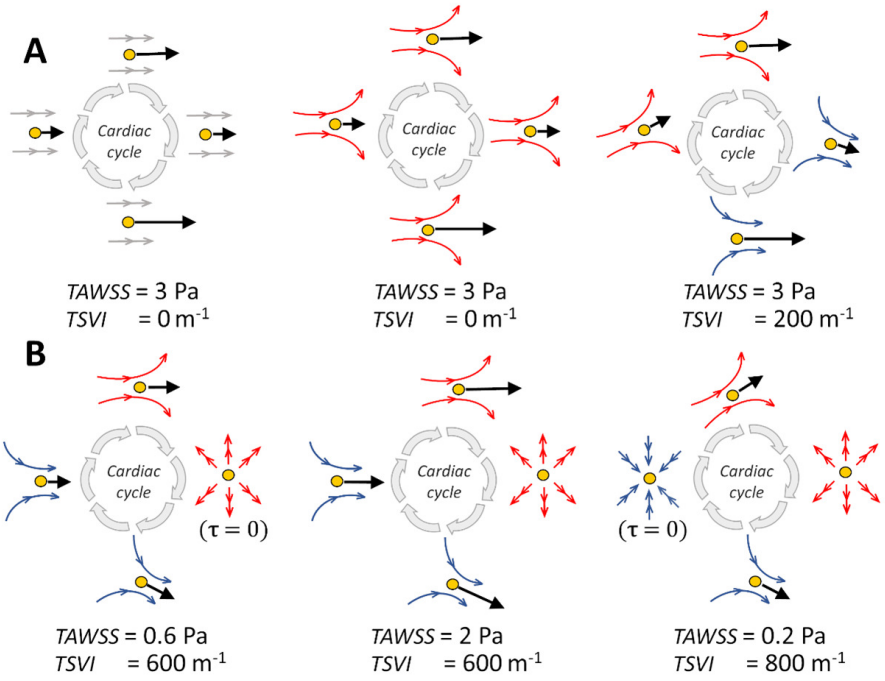

Figure 10.3: Six different flow environments to which an EC could be exposed. Black arrows represent instantaneous WSS vectors ($\boldsymbol{\tau}$) applied to a generic point (yellow circle) on the luminal surface at different time points (grey arrows) along the cardiac cycle, concurring to TAWSS determination in that point. Blue and red arrows indicate the WSS vector field instantaneous streamlines in the surroundings of the generic point (yellow circle) on the luminal surface at different time points along the cardiac cycle, concurring to TSVI determination in that point.

10.3 Results

The variation of the WSS contraction/expansion action along the cardiac cycle, expressed in terms of $TSVI$ luminal distribution at T1 and T2, is presented in Figure 10.4 for three explanatory coronary models (LAD, LCX, and RCA of pig A in Figure 10.2) together with the distribution of measured WT at time points T1, T2 and T3. It can be observed that in general: (1) luminal surface regions exposed to high $TSVI$ values co-located with high WT values; (2) luminal surface areas exposed to high $TSVI$ values at T1 co-locate with regions of WT progression in the time interval T2-T1 and T3-T1; (3) albeit moderately, luminal surface areas experiencing an increase in $TSVI$ from T1 to T2 co-locate with regions of WT growth over time (as can be seen along the LAD and RCA, and at the proximal part of LCX shown in Figure 10.4); (4) albeit moderately, luminal surface areas

experiencing a decrease in $TSVI$ from T1 to T2 co-locate with regions of WT regression in the time interval T3-T2 (see e.g., the distal part of LCX of pig A in Figure 10.4).
From a parallel analysis of TAWSS luminal distribution at T1 and T2 (Figure 10.4)), it can be observed that in general: (1) luminal surface regions exposed to low TAWSS values present with high WT values; (2) luminal surface areas experiencing low TAWSS values at T1 present with WT values at T2 and T3 higher than at T1; (3) luminal surface areas exposed to an increase in TAWSS from T1 to T2 only partially co-localize with regions of WT regression in the time interval T3-T2 (see e.g., the distal part of LCX of pig A in Figure 10.4)).
The analysis is presented in terms of odds ratio (Figure 10.5a) as well as in terms of percentage increase in the odds of the adverse outcome (Figure 10.5b). For this analysis, high WT (>66^{th} percentile) was considered as the adverse outcome. The exposure to high $TSVI$ (>80^{th} percentile) or to low TAWSS (<20^{th} percentile) largely predicted the same connections to adverse outcome. Looking at the data longitudinally first, both low TAWSS and high $TSVI$ at earlier time points were good predictors of later thickening. Specifically, low TAWSS was a slightly stronger predictor than high $TSVI$ (increase in the odds of later adverse outcome in the ranges of 88-325% and 99-206%, respectively), except at T2, where high $TSVI$ was stronger predictor of high WT at T3. The combination of low TAWSS and high $TSVI$ was an even stronger predictor of adverse outcome at T3 (174% increase in the odds) than low TAWSS or high $TSVI$ alone (88% and 118% increase in the odds, respectively, Figure 10.5). Now looking at the data transversally, both low TAWSS and high $TSVI$ at T1 and T2 also co-localized with high WT at their respective time points, with low TAWSS more strongly co-localized at T1 (256% vs. 163% of increase in the odds) and high $TSVI$ at T2 (99% vs. 34% of increase in the odds). Locations experiencing contemporaneous low TAWSS and high TSVI at T1 presented with increased odds of high WT at T1 (362%), markedly higher than single quantities (256% and 163% increase in the odds, respectively, Figure 10.5).
Mirroring the analysis for adverse outcome, here we applied the same approach to favourable outcome, here defined as low WT (<33^{rd} percentile). The exposure to low $TSVI$ (<20^{th} percentile) or to high TAWSS (>80^{th} percentile) and their association with low WT is presented in Figure 10.6. From the longitudinal analysis it emerged that high TAWSS at earlier time points was a stronger predictor

of favourable outcome than low $TSVI$ (increase in the odds of later favourable outcome in the ranges of 64-211% and 70-121%, respectively). To be noted, low $TSVI$ at T2 was not a strong predictor of low thickening at T3 (Figure 10.6). The combination of high TAWSS and low $TSVI$ at T1 was an even stronger predictor of favourable outcome (301% and 259% increase in the odds at T2 and T3, respectively) than high TAWSS or low $TSVI$ alone (Figure 10.6). The same combination at T2 was unable to predict low thickening at T3. Looking at the data transversally, only high TAWSS at T1 co-localized with low WT at the same time point (157% increase in the odds of favourable event, Figure 10.6). Locations experiencing contemporaneous high TAWSS and low TSVI at T1 presented with increased odds of low WT at the same time point (113%), but lower than single quantity high TAWSS (113% vs. 157% increase in the odds, respectively, Figure 10.6).
To clarify whether WSS topological skeleton features reflect intravascular helical flow patterns, which have an atheroprotective role in coronary arteries [154, 155], an explanatory coronary model (LAD of pig A) is presented in Figure 10.7. By visual inspection, it emerged that both at time T1 and T2 the luminal surface areas experiencing high variation in the WSS contraction/expansion action along the cardiac cycle (expressed in terms of $TSVI$) enclose the separation region between counter-rotating helical blood flow patterns (highlighted by red and blue cycle-average LNH isosurfaces in Figure 10.7). The latter is emphasized by displaying $TSVI$ and LNH (and, for sake of completeness, TAWSS) distributions at explanatory luminal cross-sections along both the proximal and distal arterial segments in Figure 10.6. In general, those observations are common to all the coronary models involved in the study.

10.4 Discussion

In previous studies, coronary atherosclerotic plaque development is linked to local time-varying hemodynamic features, such as the local WSS along the cardiac cycle, oscillatory changes in its direction and multidirectionality [75, 12, 183, 74, 108]. Currently, it is unclear which are the consequences of the spatial configuration of the shear forces acting in the neighbourhood of a given point, i.e., as opposed to local WSS features, in terms of atherosclerosis initiation/progression. The spatial configuration patterns can be interpreted as a contraction/expansion action exerted by of the shear forces acting on the endothelium and can be identified by the

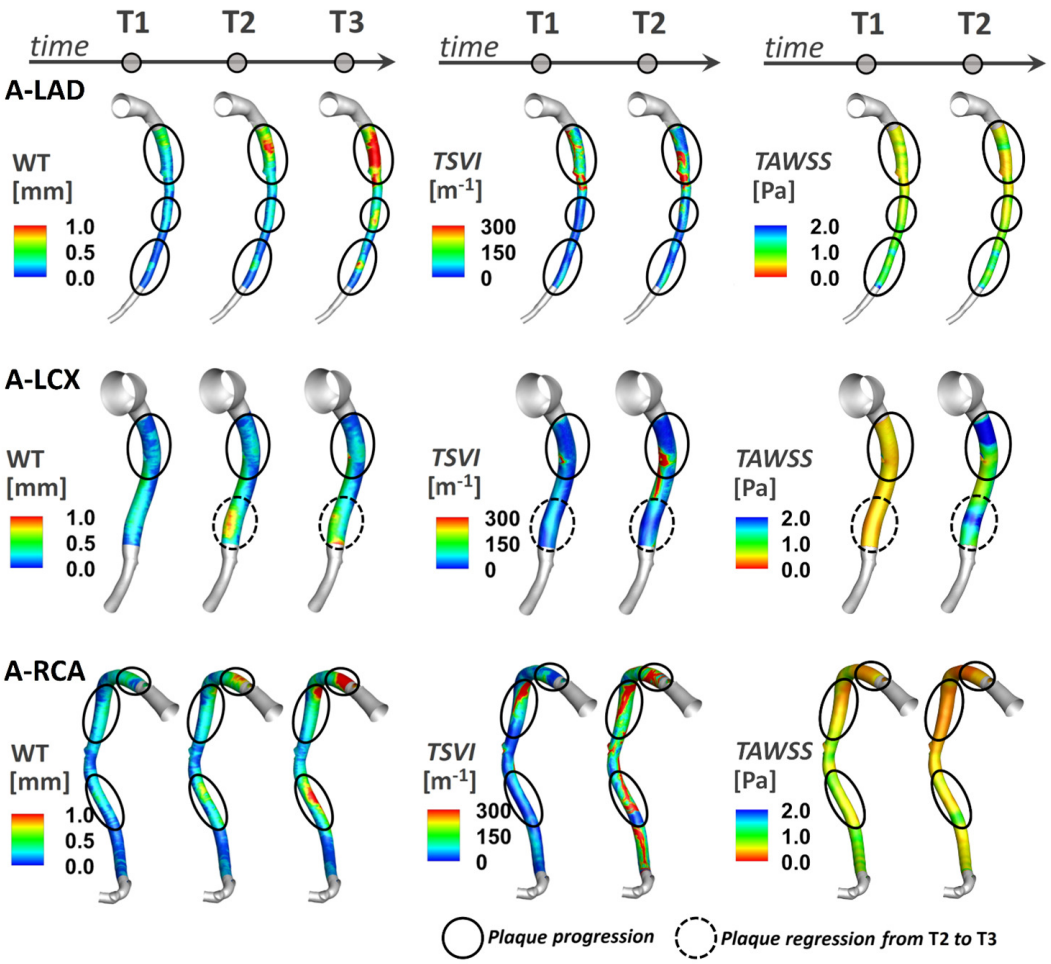

Figure 10.4: Luminal distributions of measured WT, $TSVI$ and TAWSS at several time points along the follow-up time for the coronary artery models of pig A. The distributions of WT, $TSVI$ and TAWSS are only shown along the IVUS segment of the main vessel. The side branches are not shown. The regions of interest identified along each vessel are emphasized by solid black circle if experiencing plaque progression over time or dashed black circle if experiencing plaque regression between T2 and T3.

WSS vector field divergence, which represents the rate of separation of close WSS trajectories. In terms of biomechanics, the contraction/expansion action exerted by shear forces on ECs is responsible for both intracellular and intercellular tension, which in turn may impact on e.g. shrinking/widening of cellular gaps, ultimately leading to wall thickening due to atherosclerosis [199, 200].

The most striking results to emerge from this study are that: both investigated

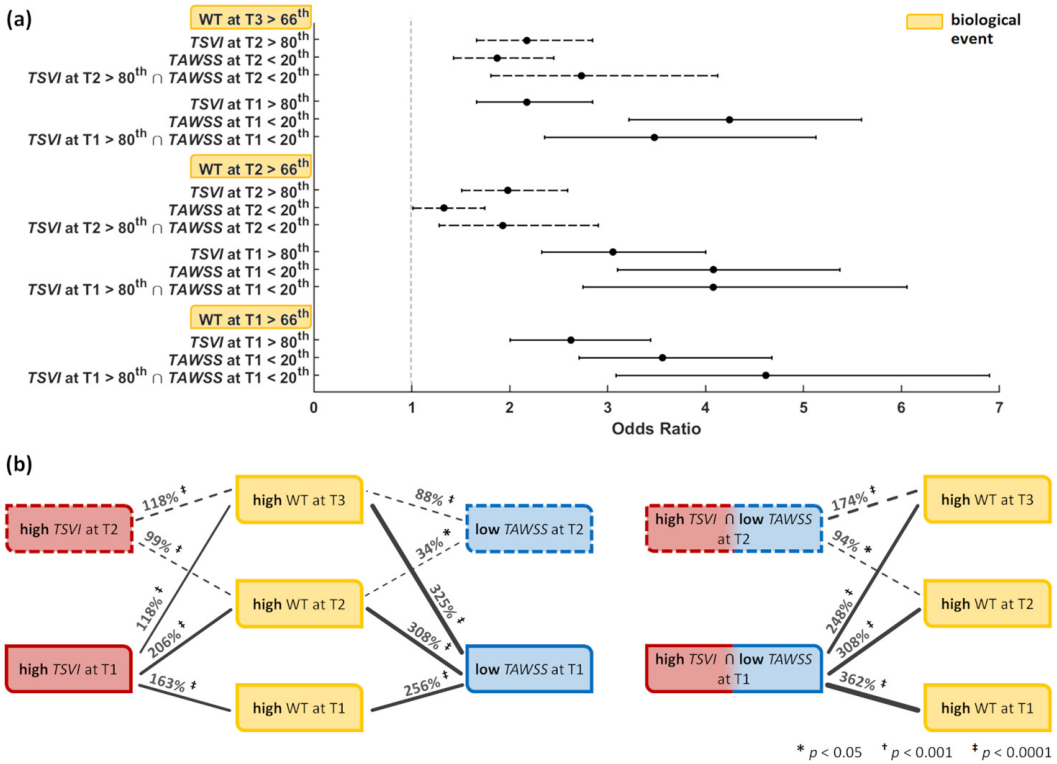

Figure 10.5: Predictive ability of hemodynamic descriptors for high WT. (a): Odds ratios with associated confidence interval for hemodynamic events *vs.* high WT at the various time points. (b): Graphical sketch of the identified significant associations between hemodynamic and biological events. The adverse (high WT) biological events are indicated in yellow. Red and blue indicate high $TSVI$ and low TAWSS, respectively. Associations are represented by black lines whose thickness is proportional to the indicated percent increase in odds of high WT (p-values also shown). Solid vs. dashed lines indicate associations for hemodynamic events at T1 *vs.*. T2, respectively.

hemodynamic stimuli at the endothelial level – high variations in the WSS contraction/expansion action on the endothelium along the cardiac cycle (quantified by $TSVI$) and low time-average WSS magnitude (quantified by TAWSS) – were associated with WT growth, accounting for different hemodynamic effects portending atherosclerosis; (2) $TSVI$ and TAWSS values in a physiological range appeared to play an atheroprotective role on ECs; (3) high variations in WSS manifolds dynamics along the cardiac cycle corresponded to intravascular regions of separation between left- and right-handed helical flow patterns.

Present findings expand the impact of local hemodynamics on the onset/development

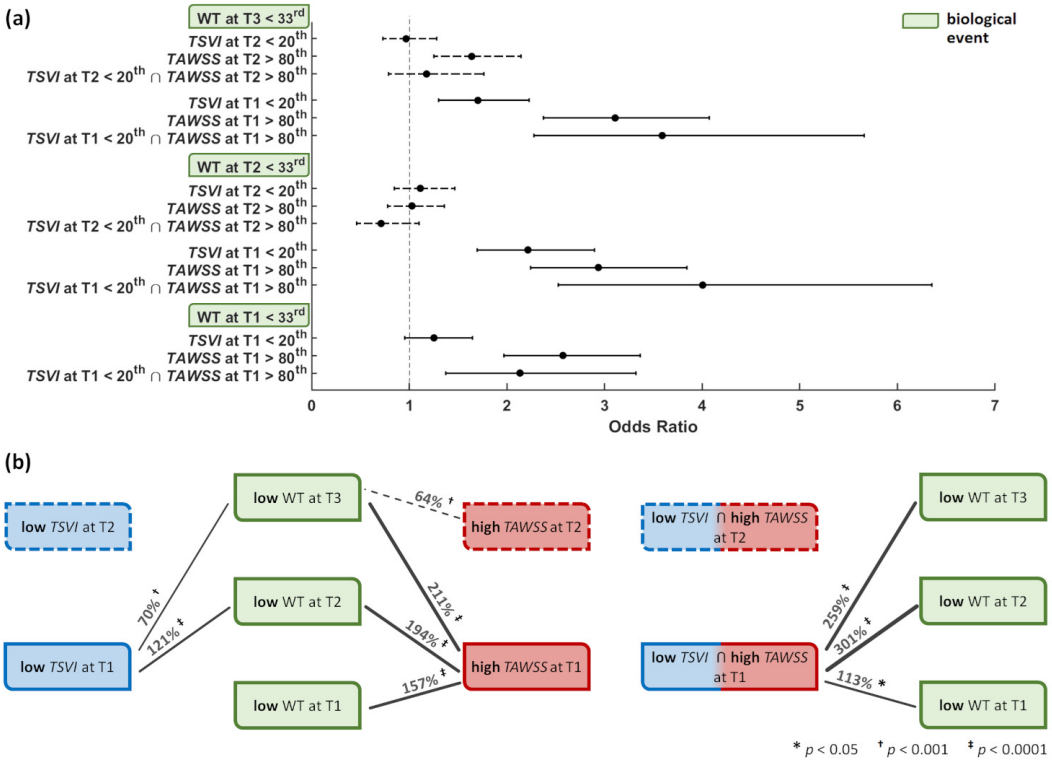

Figure 10.6: Predictive ability of hemodynamic descriptors for low WT. (a): Odds ratios with associated confidence interval for hemodynamic events *vs.* low WT at the various time points. (b): Graphical sketch of the identified significant associations between hemodynamic and biological events. The favourable (low WT) biological events are indicated in green. Blue and red now indicate low $TSVI$ and high TAWSS, respectively. Associations are represented by black lines whose thickness is proportional to the indicated percent increase in odds of high WT (p-values also shown). Solid *vs.* dashed lines indicate associations for hemodynamic events at T1 vs. T2, respectively.

of coronary atherosclerosis, suggesting that, in addition to low WSS [183, 201], also the high variability in the action exerted by the WSS vector field in the neighbourhood of a generic position at the luminal surface represents a relevant hemodynamic cue in coronary artery disease. Results from this study indicated that the WSS manifolds dynamics along the cardiac cycle (here quantified in terms of $TSVI$) is linked to WT in coronary arteries, with a relationship with future WT patterns. This relation is explained by the fact that WSS manifolds dynamics along the cardiac cycle markedly reflects those near-wall flow disturbances [21] which are known to condition the natural history of coronary atherosclerosis [12].

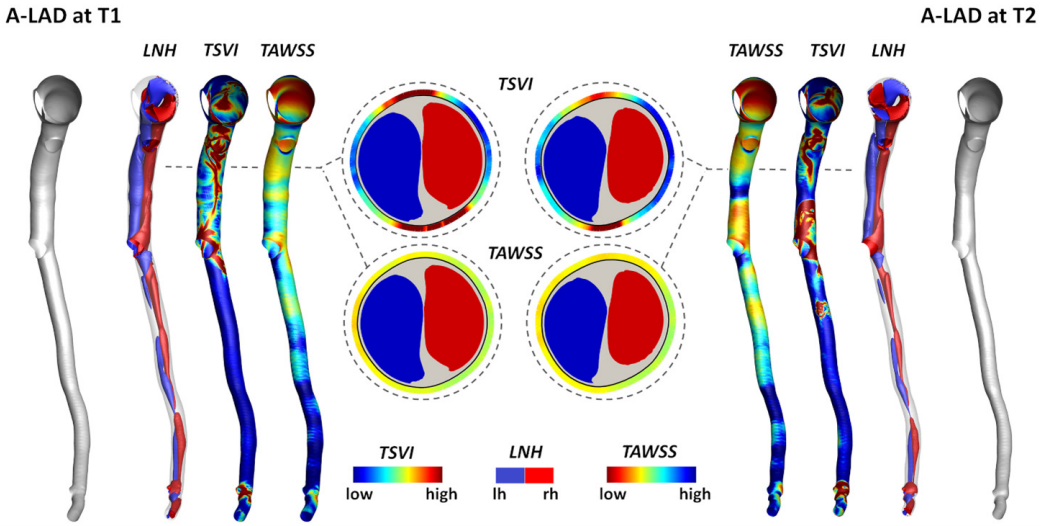

Figure 10.7: Distribution of intravascular helical blood flow features and $TSVI$ and TAWSS at the luminal surface of the LAD of pig A at T1 (left) and T2 (right) of the study. Right-handed (LNH>0) and left-handed (LNH<0) helical blood structures are displayed by red and blue, respectively. The luminal distributions of $TSVI$ and TAWSS are also shown. Only the main vessel is displayed; the side branches are not depicted. One explanatory luminal cross-section per model is reported. The lumen contour is markedly thick for a better visualization of $TSVI$ and TAWSS values at the luminal cross-section edge.

This study confirms the recently emerged evidence that WSS topological skeleton features influence vascular pathophysiology [21]. The main novelty of the study, i.e., the emerged association of $TSVI$ with WT, can be interpreted by linking biomechanics to possible biological mechanisms involved in atherosclerosis. In detail, on the one hand an ostensibly normal variability of the contraction/expansion action exerted by the WSS on the endothelium during the cardiac cycle is expected to maintain ECs in a quiescent state, with a fusiform shape and with stable intercellular junctions [202, 3] stimulating the expression of atheroprotective and antithrombogenic genes contributing to prevent atherosclerotic plaque initiation [3]. On the other hand, the luminal exposure to markedly variable WSS manifolds dynamics during the cardiac cycle may mechanically induce recurring variations in ECs intracellular as well as intercellular tensions (e.g. acting on cell junctions inclinations) [203, 181, 204], with consequent alteration of the mechanism of tension

propagation not only within the cell, but also from cell to cell. The latter may modulate ECs translation and transcription, thus affecting their pro-atherogenic susceptibility [205]. A plausible consequence for changes in directionality and magnitude of cellular tensions is, indeed, the shrinking/widening of ECs junctions, which influences the endothelium permeability to atherogenic species such as lipoproteins [3, 160], and/or promotes endothelium proinflammatory phenotype enhancing EC oxidative state [3, 206]. Moreover, it may impact ECs quiescence and obstruct physiological ECs fusiform shaping. On top of that, in turn, all these biological mechanisms are recognized to stimulate EC atherogenic genes expression as well, thus potentially promoting atherosclerosis initiation and faster progression [202, 3, 207, 160, 183]. Although the luminal exposure to high $TSVI$ may induce similar pro-atherogenic biological effects compared to low TAWSS, the two hemodynamic events are different from a mechanistic viewpoint.

The widely recognized role played by WSS magnitude (biomechanically described by the canonical indicator TAWSS) in coronary atherogenesis and development [183, 208, 1] was here confirmed: high WT was observed along the follow-up time at luminal sectors exposed to low TAWSS (Figure 10.5). However, according to previous studies revealing its weak-to-moderate ability to predict lesion localization and development [18, 201] or endothelial disfunction [19] at the early stage, our findings suggest that low TAWSS *per se* does not fully characterize the WSS features promoting coronary atherosclerosis onset/progression. A possible explanation for this evidence may have to do with the mechanistic meaning of TAWSS that, *stricto sensu*, measures the local cycle-average WSS magnitude and thus its low value reflects (1) a locally weak shear force on the endothelium and, in general, (2) a thickened diffusive boundary layer for blood-wall mass transfer. As expected by its definition, $TSVI$, reflecting the variability of the fluid forces generating endothelial intracellular and intercellular tensions, allows the identification of peculiar flow disturbances linked to biological events that cannot be captured by low TAWSS. A confirmation is given by the observation that, considering the luminal sectors where high $TSVI$ or low TAWSS co-localized with high WT, the co-localization of the two WSS-based metrics was observed in only the 14.2% of the sectors. Therefore, low TAWSS and high TSVI account for different hemodynamic effects, both linked to WT changes. In support of this, the explanatory examples presented in Figure 10.8 for two different vessels, where polar plots were used to analyze the cross-sectional distribution of WT, TAWSS and $TSVI$ as well as the observable co-localization for

those quantities. In detail, Figure 10.8 shows the cases when: (1) high $TSVI$ and low TAWSS co-localize with high WT (Figure 10.8, panels a, b); (2) low TAWSS only co-localizes with high WT (Figure 10.8, panel c); (3) high $TSVI$ only co-localizes with high WT (Figure 10.8, panel d). Therefore, the analysis in Figure 10.8 further supports the hypothesis that high $TSVI$ is to be intended as not in competition with low TAWSS, but as able to integrate the characterization of the WSS features involved in the onset/progression of coronary atherosclerosis.
Of note, the findings of this study also confirm the atheroprotective role of physiological WSS, while suggesting that also physiological values of $TSVI$ protect the coronary arteries from plaque progression.

Finally, the findings of this study highlight that a link exists between the luminal $TSVI$ distribution and intravascular helical flow patterns (Figure 10.7), since high $TSVI$ values were in general found in correspondence of the separation between counter-rotating helical structures. This recapitulates the known beneficial influence of helicity in suppressing flow disturbances in main arteries and, in particular, its atheroprotective role in the context of coronary atherosclerosis [155]. Furthermore, these findings enforce previous suggestions on the use of helical flow-based quantities as in *in vivo* surrogate marker of atherosclerotic plaque onset/progression in coronary arteries [155]. In the next future, the advances in phase-contrast magnetic resonance imaging are expected to make the *in vivo* quantification of arterial helical flow feasible also in small vessels [209, 210], as coronary arteries, allowing the non-invasive *in vivo* prediction of atherosclerosis progression based on helical flow descriptors.

This study faces some possible limitations. As main limitation of the numerical simulations, vascular walls were assumed to be rigid. However, it has been reported that the vascular wall motion does not markedly affect the distribution of canonical WSS-based quantities [211], and we expect a similar result for $TSVI$. In addition, the cardiac-induced motion of coronary arteries was neglected, based on previous findings demonstrating the moderate effect of myocardial motion on coronary flow and WSS distribution [212, 213]. Moreover, the generality of the presented study might be limited by the small number of coronary artery models used in the analysis (N=9). However, here we considered multiple sectors within each coronary artery and this allowed for statistically significant relations to emerge, revealing the existing links between local hemodynamics, WT, and WT progression. In addition, the different temporal extension of the time periods T2-T1 and T3-T2 may affect

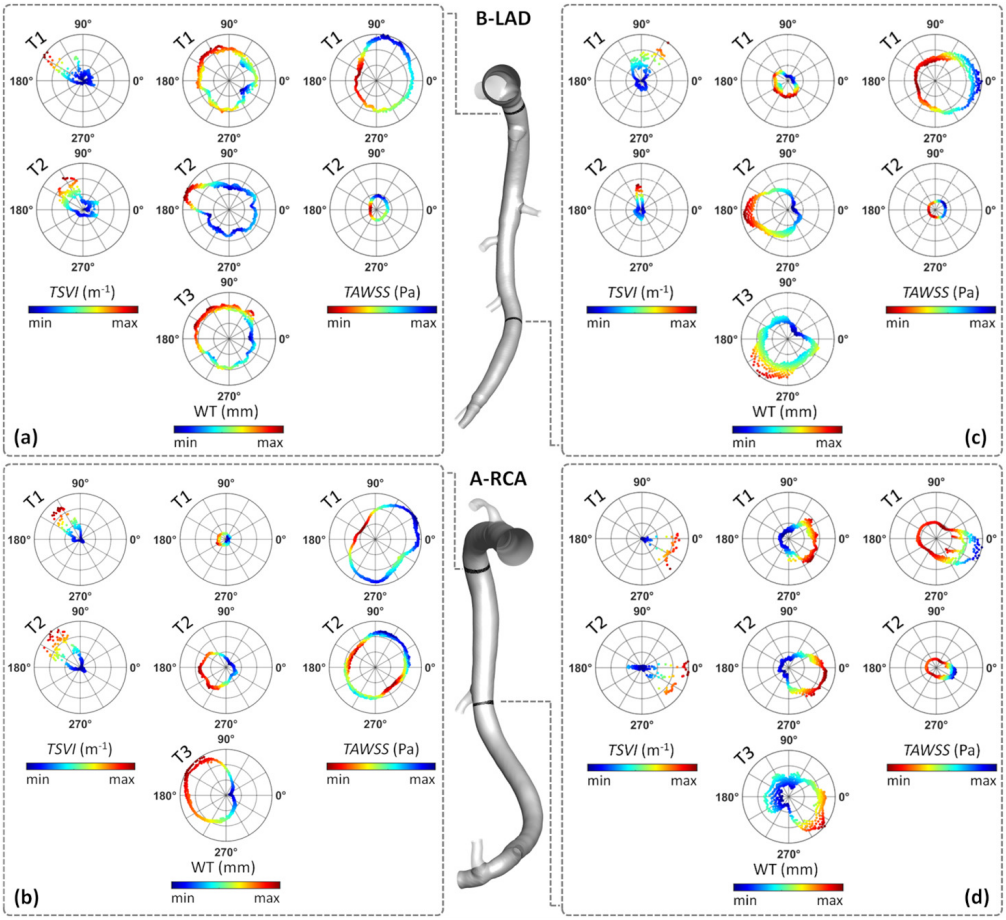

Figure 10.8: Polar plots showing $TSVI$, WT, and TAWSS cross-sectional distributions at several time points along the follow-up time for the LAD of pig B (top) and the RCA of pig A (bottom). The distributions of $TSVI$, WT and TAWSS over the follow-up time are shown at two explanatory cross-sections per vessel (coloured by black) along the IVUS-imaged segment. Colormaps are normalized by the maximum value of each descriptor.

findings on the relation between hemodynamics and WT progression. To limit its effect on the study we normalized measured WT growth with respect to follow-up time. Finally our findings are based on a pig model; however, such models, because of the similar anatomy with human coronary arteries, are widely used in studies of coronary artery diseases [214].

10.5 Supplementary Materials

10.5.1 Medical Imaging and Geometry Reconstruction

The three main coronary arteries (Left Anterior Descending (LAD), Left Circumflex (LCX), and Right (RCA), coronary artery) of each animal model were imaged by computed coronary tomography angiography (CCTA) and intravascular ultrasound (IVUS) at two time points in the follow-up study (baseline and T2). An in-house developed algorithm was uses to trigger offline IVUS images and to remove the heartbeat artefact. The CCTA images were triggered in diastole. Both IVUS and CCTA images were then used to reconstruct the pig-specific coronary artery geometries at T1 and T2. In details, at each time point IVUS images were segmented into lumen contours with QCU-CMS software (Leiden, The Netherlands), and then aligned along the 3D centerline extracted from CCTA images using the Mevislab software (Bremen, Germany). As previously reported [215], IVUS and CCTA images were matched using side branches as anatomical landmarks. The resulting geometries are displayed in Figure 10.2.

10.5.2 Numerical Settings

The finite volume method was applied to numerically solve the Navier-Stokes equations in their discrete form. To do that, the computational fluid dynamics (CFD) code Fluent (ANSYS Inc., USA) on fluid domains discretized in ICEM (ANSYS Inc., USA), by means of tetrahedrons and 5-layers prismatic boundary layer. Blood was modelled as a non-Newtonian fluid using the Carreau model with density ρ equal to 1060 kg/m^3 and dynamic viscosity defined as:

$$\mu_{app}(\dot{\gamma}) = \mu_\infty + (\mu_0 - \mu_\infty)(1 + (\lambda\dot{\gamma})^2)^{\frac{n-1}{2}}, \tag{10.2}$$

where, $\dot{\gamma}$ is the shear rate, and $\mu_\infty = 0.0035$ kg $m^{-1}s^{-1}$, μ_0=0.25 kg $m^{-1}s^{-1}$, λ=25 s, n=0.25 [195].

As for the applied boundary conditions (BCs), for each coronary model, the most proximal in vivo ComboWire Doppler measurement-based flow rate was applied in terms of time-dependent flat velocity profile at the inlet section. Based on Doppler measurements availability, measured or estimated flow ratio was prescribed at the outlet section of each side branch. Second order accuracy was set to solve both the

momentum equation and pressure with the COUPLED pressure-velocity scheme. A fixed time increment was set for time integration, by applying the backward Euler method. Each cardiac period consisted of 100 time-steps. Convergence was achieved for continuity and momentum residuals lower than 10^{-5}. All CFD setting (including mesh element size) were based on a sensitivity analysis, allowing only differences in terms of WSS lower than 1%.

Chapter 11

Conclusions and Future Works

11.1 Summary and conclusions

Understanding the nature of the blood flow behaviour in vessels is one of the important challenges in hemodynamics research. The need for the identification of unfavourable hemodynamic patterns in blood vessels is dictated by the so-called hemodynamic risk hypothesis, suggesting a key role of flow disturbances in vascular pathophysiology [12]. The action of blood flow forces on the endothelial mechanosensing and biochemical machinery has been historically explained in terms of WSS, massively involved in the development, growth, remodelling, and maintenance of the vascular system [1, 79]. However, only poor-to-moderate and sometimes contradictory links between vascular disease and WSS-based metrics have emerged until now [17, 18, 19], motivating a more in-depth analysis to close the gap of knowledge currently hampering the use of WSS as a biomarker for diagnostic and prognostic purpose [20]. In this regard, the ability of the WSS topological skeleton to capture flow features associated with adverse vascular response and reflecting cardiovascular flow complexity [21] has recently attracted a strong research interest. Besides, recent studies have demonstrated that the cycle-average WSS topological skeleton governs the near-wall biochemical transport in arteries [22, 23, 25, 24], which plays a fundamental role in e.g., endothelium-mediated vasoregulation, thrombosis, and atherosclerosis[11].

Previous studies addressing the WSS topological skeleton analysis in cardiovascular flows are mostly based on Lagrangian techniques [22, 23]. Although Lagrangian-based approaches are useful in the detection of topological structures in

complex and time-dependent flows, they require a high number of Lagrangian tracers to be seed in the domain of interest, the application of higher-order integration schemes, and generally a high computational effort [96, 38].

Stimulated from this scenario, the here proposed Eulerian method for WSS topological skeleton identification on 3D complex geometry has the potential of simplifying the WSS topological analysis in cardiovascular flows. Such presented methodology is intended to facilitate the reproducibility and comparability of results from WSS topological skeleton analysis among different studies, aiming at increasing the chance of elucidating the role that peculiar WSS features play in vascular pathophysiology. In fact, the described approach can be easily implemented: it requires only the single snapshots of the WSS vector field, e.g., as output from the CFD simulation, and the post-processing algorithms, based on a robust theory, are easy to be reproduced. This approach does not require the Lagrangian surface transport computation and numerical integration schemes, as needed for Lagrangian-based and integrated trajectory-based methods [96], thus reducing computational costs and time. In addition, it is physically intuitive and does not require a high level of experience or knowledge. Finally, it is characterized by modularity, in the sense that the method can be applied only for the purpose of fixed points identification and/or classification, or only for contraction/expansion regions identification.

The proposed Eulerian-based approach allowed the exploration of the possible involvement of WSS topological skeleton features in processes leading to vascular dysfunction, by applying the method on personalized computational hemodynamics models of healthy and pathologic cardiovascular districts. The findings of this work confirm what has been inferred in previous studies [22, 21] on the WSS topological skeleton: WSS topological skeleton features are associated to markers of vascular disease. In particular, findings of this thesis suggest a direct link between WSS topological skeleton features and e.g., late restenosis in endarterectomized carotid arteries, aortic wall stiffness, and atherosclerotic plaque onset and progression in coronary arteries.

In conclusion, the biomechanical analysis presented in this thesis and the findings from this work may increase the chance of clarifying the cause-effect relationships at the basis of the links between flow disturbance and clinical outcomes when applied to real-world clinical data.

The principal contributions from each chapter of this thesis are summarized in the following.

Chapter 1: Introduction

The introductory chapter reports a review of the physiological and hemodynamic background for motivating the work presented in this thesis.

Chapter 2: Theoretical concepts

Lagrangian-based methods for WSS topological skeleton identification currently adopted in the literature are presented and the theory supporting the here proposed Eulerian-based approach is provided.

Chapter 3: Eulerian-based Method for Wall Shear Stress Topological Skeleton Identification

In this chapter, algorithms for WSS topological skeleton features identification based on the here proposed approach are extensively described.

Chapter 4: Benchmarking

Results from this chapter confirm the ability of the here proposed method to correctly approximate Lagrangian structures and manifolds of the WSS vector field without restoring to numerical integration schemes, as required for Lagrangian-based approaches.

Chapter 5: Wall Shear Stress Divergence as a Template of Near-Wall Mass Transport in Aortic Flow

In this chapter, the ability of the proposed Eulerian method for WSS topological skeleton analysis to provide an affordable template of the LDL blood-wall transfer in patient-specific computational hemodynamic models of human aorta is tested. Findings from this chapter demonstrate that the Eulerian approach provides a close representation of the LDL wall uptake, with a significative reduction of computational costs with respect to classical mass transport simulations and Lagrangian-based techniques.

Chapter 6: Analysis of the Unsteady Nature of Wall Shear Stress Topological Skeleton Features

From the analysis of the time dependence of the WSS topological skeleton along the cardiac cycle in personalized computational hemodynamics models of one carotid bifurcation and one intracranial aneurysm, it emerged the importance of considering the unsteadiness of WSS fixed points and manifolds along the cardiac cycle, underlining the physical significance of WSS fixed points dynamics along the cardiac cycle.

Chapter 7: Wall Shear Stress Topological Skeleton Predicts long-term Restenosis Risk after Surgery in the Carotid Bifurcation

This study confirms that WSS topological skeleton features are direct associated to markers of vascular disease. High variability in the WSS contraction/expansion and high WSS fixed points weighted residence times at 1 month after CEA are correlated to IMT measurements at 60 months follow-up as markers of vascular disease at the carotid bifurcation. Moreover, the findings of this study may help in clarifying the role played by hemodynamics in the mechanisms underlying the development of long-term carotid restenosis after CEA (and, by extension, of atherosclerosis), demonstrating that WSS topological skeleton features might represent a different hemodynamic cue with respect to low WSS.

Chapter 8: Deciphering Ascending Thoracic Aortic Aneurysm Hemodynamics in Relation to Biomechanical Properties

In this study, the integration of computational hemodynamics, *in vivo* stiffness estimation and advanced fluid mechanics methods allowed to explore more in depth the existence of links between the altered hemodynamics in the ATAA and the wall biomechanical degradation. Despite the exploratory nature of the study, advanced methods of analysis of the aortic blood flow have shown their very strong potential to decipher the links between local hemodynamics and the degradation of the mechanical properties of the aortic wall. In this sense, findings of the study candidate WSS topological skeleton features as promising indicators of local wall degeneration.

Chapter 9: Wall Shear Stress Topological Skeleton Features in Image-Based Stented Coronary Bifurcation Models

With the intent to explore the involvement of WSS topological features in the processes leading to stent failure, findings from this analysis suggest that WSS topological skeleton features could represent a hemodynamic cue promoting coronary in-stent restenosis. The approach presented in this chapter might contribute to a deeper understanding of the hemodynamics-driven processes underlying in-stent restenosis in coronary arteries.

Chapter 10: The Variability of the Shear Stress Contraction/Expansion Action Contributes to Wall Thickness Change in Coronary Arteries

This chapter confirms the existence of links between WSS topological skeleton and markers of vascular disease in coronary arteries, contributing to the picture about the role of WSS in vascular pathophysiology. Through a mechanistic interpretation of the action exerted by the WSS vector field on the endothelium, this study may contribute to improve the current understanding of the impact of local hemodynamics on the onset and progression of coronary atherosclerosis. In general terms, the findings from this work suggest that the quantified variability in the contraction/expansion action exerted by the WSS on the endothelium along the cardiac cycle (1) is associated with the progression/regression of biologically relevant vascular events, and (2) represents a hemodynamic cue that well-established local WSS-based descriptors are unable to fully capture.

11.2 Future works

Based on the evidence emerged from this thesis about the physiological significance of WSS topological skeleton in cardiovascular flows, the application of the proposed Eulerian-based approach in future studies, including longitudinal data, biological mechanism and mechanobiology studies will be carried out.

Moreover, as a possible next step, future in-depth investigations could be carried out aiming at exploring the relationship (if any) between WSS topological skeleton features and atherosclerotic plaque morphology and composition. The rationale for this possible future line of research is that accurate information about

atherosclerotic plaque morphology and composition is necessary to identify the vulnerable plaques, which in turn could be useful to identify the vulnerable patient at risk for subsequent cardiovascular events. In this context, it has been shown that when atherosclerotic plaques start to intrude into the lumen, in regions surrounding plaque location the WSS changes substantially, increasing tensile stress at the plaque shoulders. The different actions exerted by the WSS on the luminal surface can lead to focal differences in plaque composition and to variations in the susceptibility to plaque rupture and atherosclerosis progression [216, 217]. Besides, several multidirectional WSS features have been recently found to contribute significantly to changes in coronary plaque composition [218]. This scenario leads to raising the hypothesis that WSS topological skeleton features could be involved in processes that govern atherosclerotic plaque morphology and composition.

Finally, a further line of research could consist in *ad hoc in vitro* studies aiming at analysing the WSS topological features biological effects. In particular, the exploration of the mechanical effect of marked variation in the contraction/expansion action exerted by the shear stress (biomechanically described by high $TSVI$) on an endothelial cells culture will be object of future studies.

Appendix A

List of Publications

A.1 Publications

- V. Mazzi, D. Gallo, K. Calò, M. Najafi, M. O. Khan, G. De Nisco, D. A. Steinman, U. Morbiducci; A Eulerian method to Analyze Wall Shear Stress Fixed Points and Manifolds in Cardiovascular Flows, Biomechanics and Modeling in Mechanobiology, 2020; 19:1403-1423. 10.1007/s10237-019-01278-3

- G. De Nisco, D. Gallo, K. Siciliano, P. Tasso, M. Lodi Rizzini, V. Mazzi, K. Calò, M. Antonucci, U. Morbiducci; Hemodialysis Arterio-venous Graft Design Reducing the Hemodynamic Risk of Vascular Access Dysfunction, Journal of Biomechanics, 2020; 10.1016/j.jbiomech.2019.109591

- K. Calò, D. Gallo, A. Steinman, V. Mazzi, S. Scarsoglio, L. Ridolfi, U. Mobiducci; Spatio-temporal Hemodynamic Complexity in Carotid Arteries: an Integrated Computational Hemodynamics & Complex Networks-Based Approach, IEEE Transactions on Biomedical Engineering, 2020; 67: 1841-1853. doi: 10.1109/TBME.2019.2949148

- G. De Nisco, P. Tasso, K. Calò, V. Mazzi, D. Gallo, F. Condemi, S. Farzaneh, S. Avril, U. Morbiducci; Deciphering ascending thoracic aortic aneurysm hemodynamics in relation to biomechanical properties, Medical Engineering & Physics, 2020; 82: 119-129. doi.org/10.1016/j.medengphy.2020.07.003

- U. Morbiducci*, V. Mazzi*, M. Domanin, G. De Nisco, C. Vergara, D. A.

Steinman, D. Gallo; Wall shear stress topological skeleton independently predicts long-term restenosis after carotid bifurcation endarterectomy, Annals of Biomedical Engineering, 2020; 48: 2936-2949. doi.org/10.1007/s10439-020-02607-9. * The two authors equally contributed.

- V. Mazzi, U. Morbiducci, K. Calò, G. De Nisco, M. Lodi Rizzini, E. Torta, G. C. A. Caridi, C. Chiastra, D. Gallo; Wall Shear Stress Topological Skeleton Analysis in Cardio-vascular Flows: Methods and Applications, Mathematics, 2021, 9(7), 720; https://doi.org/10.3390/math9070720

- A. Candreva, M. Pagnoni, M. Lodi Rizzini, T. Mizukami, E. Gallinoro, V. Mazzi, D. Gallo, D. Meier, T. Shinke, JP. Aben, S. Nagumo, J. Sonck, D. Munhoz, S. Fournier, E. Barbato, W. Heggermont, S. Cook, C. Chiastra, U. Morbiducci, B. De Bruyne, O. Muller, C. Collet; Risk of Myocardial Infarction based on Endothelial Shear Stress Analysis Using Coronary Angiography, Journal of the American College of Cardiology, *under review*

- V. Mazzi, G. De Nisco, A. Hoogendoorn, K. Calò, C. Chiastra, D. Gallo, D. A. Steinman, J. J. Wentzel, U. Mobiducci; Early atherosclerotic changes in coronary arteries are associated with endothelium shear stress contraction/expansion variability, Annals of Biomedical Engineering, *under review*

A.2 Conference Proceedings

- V. Mazzi, D. Gallo, K. Calò, M. O. Khan, D. A. Steinman, U. Morbiducci; Wall Shear Stress Topological Skeleton Identification in Cardiovascular Flows: a Practical Approach. 2019. Summer Biomechanics, Bioengineering, and Biotransport Conference, Seven Springs (PA), 25-28/06/2019.

- K. Calò, D. Gallo, V. Mazzi, S. Scarsoglio, M. O. Khan, A. Steinman, L. Ridolfi, U. Mobiducci; Computational hemodynamics & complex networks integrated platform to study intravascular flow in the carotid bifurcation. 2019. Summer Biomechanics, Bioengineering, and Biotransport Conference, Seven Springs (PA), 25-28/06/2019.

- V. Mazzi, D. Gallo, K. Calò, M. O. Khan, D. A. Steinman, U. Morbiducci;

A Practical Approach for wall shear stress topological skeleton analysis applied to intracranial aneurysm hemodynamics. 2019. Italian Chapter of the European Society of Biomechanics, Bologna (IT), 30/9-1/10/2019.

- G. De Nisco, K. Siciliano, P. Tasso, M. Lodi Rizzini, V. Mazzi, K. Calò, M. Antonucci, D. Gallo, U. Morbiducci; Exploring novel arteriovenous graft designs to reduce vascular access failure risk. 2019. Italian Chapter of the European Society of Biomechanics, Bologna (IT), 30/09-01/10/2019.
- V. Mazzi, D. Gallo, M. Domanin, K. Calò, D A. Steinman, C. Vergara, U. Morbiducci; Wall shear stress topological skeleton predicts long-term restenosis risk after surgery in the carotid bifurcation. 2020, Summer Biomechanics, Bioengineering, and Biotransport Conference, Virtual Conference, 17-20/06/2020.
- V. Mazzi, G. De Nisco, A. Hoogendoorn, C. Chiastra, D. Gallo, D. A. Steinman, J. J. Wentzel, U. Morbiducci; The wall shear stress topological skeleton predicts atherosclerotic plaque initiation and progression in coronary arteries. 2020, Summer Biomechanics, Bioengineering, and Biotransport Conference, Virtual Conference, 17-20/06/2020.
- K. Calò, G. De Nisco, D. Gallo, C. Chiastra, V. Mazzi, A. Hoogendoorn, S. Scarsoglio, D. A. Steinman, J. J. Wentzel, U. Mobiducci; Unveiling wall shear stress spatiotemporal heterogeneity in coronary arteries. 2020, Summer Biomechanics, Bioengineering, and Biotransport Conference, Virtual Conference, 17-20/06/2020.
- G. De Nisco, V. Mazzi, K. Calò, R. Ponzini, G. Rizzo, D. A. Steinman, D. Gallo, U. Morbiducci; Linking wall shear stress topological skeleton to near-wall transport in aortic flow. 2020, Virtual Physiological Human Conference, 24-28/10/2020.
- G. De Nisco, K. Siciliano, P. Tasso, M. Lodi Rizzini, V. Mazzi, K. Calò, M. Antonucci, D. Gallo, U. Morbiducci; An optimization study of hemodialysis arterio-venous grafts design to reduce vascular access risk of failure. 2020, SIMBIO-M Virtual Conference, 18-19/06/2020.
- G. De Nisco, V. Mazzi, A. Hoogendoorn, C. Chiastra, D. Gallo, D. A. Steinman, J. J. Wentzel, U. Morbiducci; The wall shear stress topological skeleton

is an independent predictor of atherosclerotic plaque development in coronary arteries. 2020, The 15^{th} International Symposium on Biomechanics in Vascular Biology and Cardiovascular Disease, Virtual conference

- G. De Nisco, V. Mazzi, K. Calò, R. Ponzini, G. Rizzo, D. A. Steinman, D. Gallo, U. Morbiducci; Eulerian-based wall shear stress topological skeleton analysis and near-wall transport in aortic flow. 2020, Congress of the National group of Bioengineering

- V. Mazzi, C. Chiastra, D. Gallo, U. Morbiducci; Wall Shear Stress Topological Skeleton Analysis In Image-based Stented Coronary Bifurcation Models. 2021, Summer Biomechanics, Bioengineering, and Biotransport Conference, Virtual Conference, 14-18/06/2021.

- G.De Nisco, V. Mazzi, K. Calò, M. Lodi Rizzini, C. Chiastra, J. J. Wentzel, D. A. Steinman, D. Gallo, U. Morbiducci; Exploring The Link Between Wall Shear StressTopological Skeleton and Near-Wall Mass Transport in Cardiovascular Flows Using aEulerian-Based Method. 2021, Summer Biomechanics, Bioengineering, and Biotransport Conference, Virtual Conference, 14-18/06/2021.

- V. Mazzi, C. Chiastra, D. Gallo, U. Morbiducci; Wall Shear Stress Topological Skeleton Features in Hemodynamic Models of Stented Coronary Arteries. 26^{th} Congress of the European society of Biomechanics, Virtual conference, 11-14/07/2021.

- G.De Nisco, V. Mazzi, K. Calò, M. Lodi Rizzini, C. Chiastra, J. J. Wentzel, D. A. Steinman, D. Gallo, U. Morbiducci; Eulerian-based Wall Shear Stress TopologicalSkeleton as a template of near-wall mass Transport in Arteries. 26^{th} Congress of the European society of Biomechanics, Virtual conference, 11-14/07/2021.

Bibliography

[1] Adel M Malek, Seth L Alper, and Seigo Izumo. "Hemodynamic shear stress and its role in atherosclerosis". In: *J. Am. Med. Assoc.* 282.21 (Dec. 1999), pp. 2035–2042. ISSN: 00987484. DOI: 10.1001/jama.282.21.2035.

[2] Siyuan Zha et al. "PJ34, a PARP1 inhibitor, promotes endothelial repair in a rabbit model of high fat diet-induced atherosclerosis." eng. In: *Cell Cycle* 18.17 (Sept. 2019), pp. 2099–2109. ISSN: 1551-4005 (Electronic). DOI: 10.1080/15384101.2019.1640008.

[3] Jeng Jiann Chiu and Shu Chien. *Effects of disturbed flow on vascular endothelium: Pathophysiological basis and clinical perspectives*. eng. Jan. 2011. DOI: 10.1152/physrev.00047.2009.

[4] D M Wootton and D N Ku. "Fluid mechanics of vascular systems, diseases, and thrombosis." eng. In: *Annu. Rev. Biomed. Eng.* 1 (1999), pp. 299–329. ISSN: 1523-9829 (Print). DOI: 10.1146/annurev.bioeng.1.1.299.

[5] Zekun Peng et al. "Endothelial Response to Pathophysiological Stress." eng. In: *Arterioscler. Thromb. Vasc. Biol.* 39.11 (Nov. 2019), e233–e243. ISSN: 1524-4636 (Electronic). DOI: 10.1161/ATVBAHA.119.312580.

[6] J S Mondy et al. "Platelet-derived growth factor ligand and receptor expression in response to altered blood flow in vivo." eng. In: *Circ. Res.* 81.3 (Sept. 1997), pp. 320–327. ISSN: 0009-7330 (Print). DOI: 10.1161/01.res.81.3.320.

[7] M Uematsu et al. "Regulation of endothelial cell nitric oxide synthase mRNA expression by shear stress." eng. In: *Am. J. Physiol.* 269.6 Pt 1 (Dec. 1995), pp. C1371–8. ISSN: 0002-9513 (Print). DOI: 10.1152/ajpcell.1995.269.6.C1371.

[8] C G Galbraith, R Skalak, and S Chien. "Shear stress induces spatial reorganization of the endothelial cell cytoskeleton." eng. In: *Cell Motil. Cytoskeleton* 40.4 (1998), pp. 317–330. ISSN: 0886-1544 (Print). DOI: 10.1002/(SICI)1097-0169(1998)40:4<317::AID-CM1>3.0.CO;2-8.

[9] Rosalind E Mott and Brian P Helmke. "Mapping the dynamics of shear stress-induced structural changes in endothelial cells." eng. In: *Am. J. Physiol. Cell Physiol.* 293.5 (Nov. 2007), pp. C1616–26. ISSN: 0363-6143 (Print). DOI: 10.1152/ajpcell.00457.2006.

[10] Amanda M D Malone et al. "The role of actin cytoskeleton in oscillatory fluid flow-induced signaling in MC3T3-E1 osteoblasts." eng. In: *Am. J. Physiol. Cell Physiol.* 292.5 (May 2007), pp. C1830–6. ISSN: 0363-6143 (Print). DOI: 10.1152/ajpcell.00352.2005.

[11] C Ross Ethier. "Computational modeling of mass transfer and links to atherosclerosis." eng. In: *Ann. Biomed. Eng.* 30.4 (Apr. 2002), pp. 461–471. ISSN: 0090-6964 (Print).

[12] Umberto Morbiducci et al. "Atherosclerosis at arterial bifurcations: Evidence for the role of haemodynamics and geometry". In: *Thromb. Haemost.* 115.3 (2016), pp. 484–492. ISSN: 03406245. DOI: 10.1160/TH15-07-0597.

[13] L Goubergrits et al. "Atherosclerosis and flow in carotid arteries with authentic geometries." eng. In: *Biorheology* 39.3-4 (2002), pp. 519–524. ISSN: 0006-355X (Print).

[14] R S Keynton et al. "Intimal hyperplasia and wall shear in arterial bypass graft distal anastomoses: an in vivo model study." eng. In: *J. Biomech. Eng.* 123.5 (Oct. 2001), pp. 464–473. ISSN: 0148-0731 (Print). DOI: 10.1115/1.1389461.

[15] Heather A Himburg et al. "Spatial comparison between wall shear stress measures and porcine arterial endothelial permeability." eng. In: *Am. J. Physiol. Heart Circ. Physiol.* 286.5 (May 2004), H1916–22. ISSN: 0363-6135 (Print). DOI: 10.1152/ajpheart.00897.2003.

[16] Veronique Peiffer, Spencer J Sherwin, and Peter D Weinberg. "Computation in the rabbit aorta of a new metric - the transverse wall shear stress - to quantify the multidirectional character of disturbed blood flow." eng. In: *J.*

Biomech. 46.15 (Oct. 2013), pp. 2651–2658. ISSN: 1873-2380 (Electronic). DOI: 10.1016/j.jbiomech.2013.08.003.

[17] Chong Wang et al. "Endothelial cell sensing of flow direction". eng. In: *Arterioscler. Thromb. Vasc. Biol.* 33.9 (Sept. 2013), pp. 2130–2136. ISSN: 10795642. DOI: 10.1161/ATVBAHA.113.301826.

[18] Veronique Peiffer, Spencer J Sherwin, and Peter D Weinberg. "Does low and oscillatory wall shear stress correlate spatially with early atherosclerosis? A systematic review." eng. In: *Cardiovasc. Res.* 99.2 (July 2013), pp. 242–250. ISSN: 1755-3245 (Electronic). DOI: 10.1093/cvr/cvt044.

[19] Diego Gallo et al. "Segment-specific associations between local haemodynamic and imaging markers of early atherosclerosis at the carotid artery: an in vivo human study." eng. In: *J. R. Soc. Interface* 15.147 (Oct. 2018). ISSN: 1742-5662 (Electronic). DOI: 10.1098/rsif.2018.0352.

[20] Diego Gallo, David A Steinman, and Umberto Morbiducci. "Insights into the co-localization of magnitude-based versus direction-based indicators of disturbed shear at the carotid bifurcation." eng. In: *J. Biomech.* 49.12 (Aug. 2016), pp. 2413–2419. ISSN: 1873-2380 (Electronic). DOI: 10.1016/j.jbiomech.2016.02.010.

[21] Amirhossein Arzani and Shawn C. Shadden. "Wall shear stress fixed points in cardiovascular fluid mechanics". In: *J. Biomech.* 73 (2018), pp. 145–152. ISSN: 18732380. DOI: 10.1016/j.jbiomech.2018.03.034. URL: https://doi.org/10.1016/j.jbiomech.2018.03.034.

[22] Amirhossein Arzani et al. "Wall shear stress exposure time: a Lagrangian measure of near-wall stagnation and concentration in cardiovascular flows." eng. In: *Biomech. Model. Mechanobiol.* 16.3 (June 2017), pp. 787–803. ISSN: 1617-7940 (Electronic). DOI: 10.1007/s10237-016-0853-7.

[23] Amirhossein Arzani et al. "Lagrangian wall shear stress structures and near-wall transport in high-Schmidt-number aneurysmal flows". In: *J. Fluid Mech.* 790 (2016), pp. 158–172. ISSN: 0022-1120. DOI: 10.1017/jfm.2016.6.

[24] Ali Farghadan and Amirhossein Arzani. "The combined effect of wall shear stress topology and magnitude on cardiovascular mass transport". In: *Int. J. Heat Mass Transf.* 131 (2019), pp. 252–260. ISSN: 0017-9310. DOI: https:

//doi.org/10.1016/j.ijheatmasstransfer.2018.11.051. URL: http://www.sciencedirect.com/science/article/pii/S0017931018335415.

[25] Mostafa Mahmoudi et al. "The Story of Wall Shear Stress in Coronary Artery Atherosclerosis: Biochemical Transport and Mechanotransduction". In: *J. Biomech. Eng.* (2020). ISSN: 0148-0731. DOI: 10.1115/1.4049026. URL: https://doi.org/10.1115/1.4049026.

[26] John M Tarbell. "Mass transport in arteries and the localization of atherosclerosis." eng. In: *Annu. Rev. Biomed. Eng.* 5 (2003), pp. 79–118. ISSN: 1523-9829 (Print). DOI: 10.1146/annurev.bioeng.5.040202.121529.

[27] C Ethier et al. "Steady flow separation patterns in a 45 degree junction". In: *J. Fluid Mech. (2000), 411, pp. 1-38.* 411 (2000). DOI: 10.1017/S0022112099008022.

[28] Aichi Chien et al. "Patient-specific flow analysis of brain aneurysms at a single location: comparison of hemodynamic characteristics in small aneurysms." eng. In: *Med. Biol. Eng. Comput.* 46.11 (Nov. 2008), pp. 1113–1120. ISSN: 1741-0444 (Electronic). DOI: 10.1007/s11517-008-0400-5.

[29] H Baek et al. "Flow instability and wall shear stress variation in intracranial aneurysms." eng. In: *J. R. Soc. Interface* 7.47 (June 2010), pp. 967–988. ISSN: 1742-5662 (Electronic). DOI: 10.1098/rsif.2009.0476.

[30] L. Goubergrits et al. "Statistical wall shear stress maps of ruptured and unruptured middle cerebral artery aneurysms". In: *J. R. Soc. Interface* 9.69 (2012), pp. 677–688. ISSN: 17425662. DOI: 10.1098/rsif.2011.0490.

[31] A M Gambaruto and A J João. "Computers & Fluids Flow structures in cerebral aneurysms". In: *Comput. Fluids* 65 (2012), pp. 56–65. ISSN: 0045-7930. DOI: 10.1016/j.compfluid.2012.02.020. URL: http://dx.doi.org/10.1016/j.compfluid.2012.02.020.

[32] L Goubergrits et al. "In vitro study of near-wall flow in a cerebral aneurysm model with and without coils." eng. In: *AJNR. Am. J. Neuroradiol.* 31.8 (Sept. 2010), pp. 1521–1528. ISSN: 1936-959X (Electronic). DOI: 10.3174/ajnr.A2121.

[33] Magnus Andersson et al. “Multidirectional WSS disturbances in stenotic turbulent flows: A pre- and post-intervention study in an aortic coarctation”. In: *J. Biomech.* 51 (2017), pp. 8–16. ISSN: 18732380. DOI: 10.1016/j.jbiomech.2016.11.064. URL: http://dx.doi.org/10.1016/j.jbiomech.2016.11.064.

[34] Yasutaka Tobe et al. “Relationship between Pathology and Hemodynamics of Human Unruptured Cerebral Aneurysms”. In: *15th Int. Conf. Biomed. Eng.* Ed. by James Goh. Cham: Springer International Publishing, 2014, pp. 44–47. ISBN: 978-3-319-02913-9.

[35] Daichi Suzuki et al. “Investigation of characteristic hemodynamic parameters indicating thinning and thickening sites of cerebral aneurysms”. In: *J. Biomech. Sci. Eng.* 10.1 (2015), pp. 1–10. ISSN: 18809863. DOI: 10.1299/jbse.14-00265.

[36] Liang Ge and Fotis Sotiropoulos. “Direction and magnitude of blood flow shear stresses on the leaflets of aortic valves: is there a link with valve calcification?” eng. In: *J. Biomech. Eng.* 132.1 (Jan. 2010), p. 14505. ISSN: 1528-8951 (Electronic). DOI: 10.1115/1.4000162.

[37] Ali Farghadan and Amirhossein Arzani. “The combined effect of wall shear stress topology and magnitude on cardiovascular mass transport”. In: *Int. J. Heat Mass Transf.* 131 (2019), pp. 252–260. ISSN: 00179310. DOI: 10.1016/j.ijheatmasstransfer.2018.11.051. URL: https://doi.org/10.1016/j.ijheatmasstransfer.2018.11.051.

[38] Peter J. Nolan, Mattia Serra, and Shane D. Ross. “Finite-time Lyapunov exponents in the instantaneous limit and material transport”. In: *Nonlinear Dyn.* 100.4 (2020), pp. 3825–3852. ISSN: 1573269X. DOI: 10.1007/s11071-020-05713-4. arXiv: 1904.06817. URL: https://doi.org/10.1007/s11071-020-05713-4.

[39] John H. Argyris et al. *An Exploration of Dynamical Systems and Chaos*. 2015. ISBN: 9783662460412. DOI: 10.1007/978-3-662-46042-9.

[40] C Garth, X Tricoche, and G Scheuermann. “Tracking of vector field singularities in unstructured 3D time-dependent datasets”. In: *IEEE Vis. 2004.* 2004, pp. 329–336. ISBN: VO -. DOI: 10.1109/VISUAL.2004.107.

[41] Shawn C. Shadden, Francois Lekien, and Jerrold E. Marsden. "Definition and properties of Lagrangian coherent structures from finite-time Lyapunov exponents in two-dimensional aperiodic flows". In: *Phys. D Nonlinear Phenom.* 212.3-4 (2005), pp. 271–304. ISSN: 01672789. DOI: 10.1016/j.physd.2005.10.007.

[42] G. Haller. "Distinguished material surfaces and coherent structures in three-dimensional fluid flows". In: *Phys. D Nonlinear Phenom.* 149.4 (2001), pp. 248–277. ISSN: 01672789. DOI: 10.1016/S0167-2789(00)00199-8.

[43] George Haller. "Lagrangian coherent structures". In: *Annu. Rev. Fluid Mech.* 47 (2015), pp. 137–162. ISSN: 00664189. DOI: 10.1146/annurev-fluid-010313-141322.

[44] Francois Lekien, Shawn C. Shadden, and Jerrold E. Marsden. "Lagrangian coherent structures in n-dimensional systems". In: *J. Math. Phys.* 48.6 (2007), pp. 1–19. ISSN: 00222488. DOI: 10.1063/1.2740025.

[45] Shawn C Shadden and Amirhossein Arzani. "Lagrangian postprocessing of computational hemodynamics." eng. In: *Ann. Biomed. Eng.* 43.1 (Jan. 2015), pp. 41–58. ISSN: 1573-9686 (Electronic). DOI: 10.1007/s10439-014-1070-0.

[46] Shawn C. Shadden and Charles A. Taylor. "Characterization of coherent structures in the cardiovascular system". In: *Ann. Biomed. Eng.* 36.7 (2008), pp. 1152–1162. ISSN: 00906964. DOI: 10.1007/s10439-008-9502-3.

[47] M. A. Green, C. W. Rowley, and G. Haller. "Detection of Lagrangian coherent structures in three-dimensional turbulence". In: *J. Fluid Mech.* 572 (2007), pp. 111–120. ISSN: 00221120. DOI: 10.1017/S0022112006003648.

[48] Thomas Peacock and George Haller. "Lagrangian coherent structures: The hidden skeleton of fluid flows". In: *Phys. Today* 66.2 (2013), pp. 41–47. ISSN: 00319228. DOI: 10.1063/PT.3.1886.

[49] L W Ehrlich and M H Friedman. "Particle paths and stasis in unsteady flow through a bifurcation." eng. In: *J. Biomech.* 10.9 (1977), pp. 561–568. ISSN: 0021-9290 (Print). DOI: 10.1016/0021-9290(77)90036-7.

[50] Karl Perktold. "On the paths of fluid particles in an axisymmetrical aneurysm". In: *J. Biomech.* 20.3 (1987), pp. 311–317. ISSN: 0021-9290. DOI: https://doi.org/10.1016/0021-9290(87)90297-1. URL: http://www.sciencedirect.com/science/article/pii/0021929087902971.

[51] K Perktold, R Peter, and M Resch. "Pulsatile non-Newtonian blood flow simulation through a bifurcation with an aneurysm." eng. In: *Biorheology* 26.6 (1989), pp. 1011–1030. ISSN: 0006-355X (Print). DOI: 10.3233/bir-1989-26605.

[52] K Perktold and D Hilbert. "Numerical simulation of pulsatile flow in a carotid bifurcation model". In: *J. Biomed. Eng.* 8.3 (1986), pp. 193–199. ISSN: 0141-5425. DOI: https://doi.org/10.1016/0141-5425(86)90083-X. URL: http://www.sciencedirect.com/science/article/pii/014154258690083X.

[53] D A Steinman. "Simulated pathline visualization of computed periodic blood flow patterns." eng. In: *J. Biomech.* 33.5 (May 2000), pp. 623–628. ISSN: 0021-9290 (Print). DOI: 10.1016/s0021-9290(99)00205-5.

[54] Mauro Tambasco and David A Steinman. "On assessing the quality of particle tracking through computational fluid dynamic models." eng. In: *J. Biomech. Eng.* 124.2 (Apr. 2002), pp. 166–175. ISSN: 0148-0731 (Print). DOI: 10.1115/1.1449489.

[55] Mauro Tambasco and David A Steinman. "Path-dependent hemodynamics of the stenosed carotid bifurcation." eng. In: *Ann. Biomed. Eng.* 31.9 (Oct. 2003), pp. 1054–1065. ISSN: 0090-6964 (Print). DOI: 10.1114/1.1603257.

[56] Weiguang Yang et al. "Optimization of a Y-graft design for improved hepatic flow distribution in the fontan circulation." eng. In: *J. Biomech. Eng.* 135.1 (Jan. 2013), p. 11002. ISSN: 1528-8951 (Electronic). DOI: 10.1115/1.4023089.

[57] Weiguang Yang et al. "Hepatic blood flow distribution and performance in conventional and novel Y-graft Fontan geometries: a case series computational fluid dynamics study." eng. In: *J. Thorac. Cardiovasc. Surg.* 143.5 (May 2012), pp. 1086–1097. ISSN: 1097-685X (Electronic). DOI: 10.1016/j.jtcvs.2011.06.042.

[58] Omid Amili, Robroy MacIver, and Filippo Coletti. "Magnetic Resonance Imaging Based Flow Field and Lagrangian Particle Tracking From a Left Ventricular Assist Device". In: *J. Biomech. Eng.* 142.2 (Oct. 2019). ISSN: 0148-0731. DOI: 10.1115/1.4043939. URL: https://doi.org/10.1115/1.4043939.

[59] Debanjan Mukherjee, Jose Padilla, and Shawn C. Shadden. "Numerical investigation of fluid–particle interactions for embolic stroke". In: *Theor. Comput. Fluid Dyn.* 30.1-2 (2016), pp. 23–39. ISSN: 14322250. DOI: 10.1007/s00162-015-0359-4.

[60] Umberto Morbiducci et al. "In vivo quantification of helical blood flow in human aorta by time-resolved three-dimensional cine phase contrast magnetic resonance imaging." eng. In: *Ann. Biomed. Eng.* 37.3 (Mar. 2009), pp. 516–531. ISSN: 1573-9686 (Electronic). DOI: 10.1007/s10439-008-9609-6.

[61] Umberto Morbiducci et al. "Mechanistic insight into the physiological relevance of helical blood flow in the human aorta: an in vivo study." eng. In: *Biomech. Model. Mechanobiol.* 10.3 (June 2011), pp. 339–355. ISSN: 1617-7940 (Electronic). DOI: 10.1007/s10237-010-0238-2.

[62] Amirhossein Arzani and Shawn C Shadden. "Characterization of the transport topology in patient-specific abdominal aortic aneurysm models." eng. In: *Phys. Fluids (1994).* 24.8 (Aug. 2012), p. 81901. ISSN: 1070-6631 (Print). DOI: 10.1063/1.4744984.

[63] Amirhossein Arzani et al. "Effect of exercise on patient specific abdominal aortic aneurysm flow topology and mixing." eng. In: *Int. j. numer. method. biomed. eng.* 30.2 (Feb. 2014), pp. 280–295. ISSN: 2040-7947 (Electronic). DOI: 10.1002/cnm.2601.

[64] Morteza Gharib et al. "Optimal vortex formation as an index of cardiac health." eng. In: *Proc. Natl. Acad. Sci. U. S. A.* 103.16 (Apr. 2006), pp. 6305–6308. ISSN: 0027-8424 (Print). DOI: 10.1073/pnas.0600520103.

[65] John J Charonko et al. "Vortices formed on the mitral valve tips aid normal left ventricular filling." eng. In: *Ann. Biomed. Eng.* 41.5 (May 2013), pp. 1049–1061. ISSN: 1573-9686 (Electronic). DOI: 10.1007/s10439-013-0755-0.

[66] Johannes Töger et al. "Vortex ring formation in the left ventricle of the heart: analysis by 4D flow MRI and Lagrangian coherent structures." eng. In: *Ann. Biomed. Eng.* 40.12 (Dec. 2012), pp. 2652–2662. ISSN: 1573-9686 (Electronic). DOI: 10.1007/s10439-012-0615-3.

[67] Sahar Hendabadi et al. "Topology of blood transport in the human left ventricle by novel processing of Doppler echocardiography." eng. In: *Ann. Biomed. Eng.* 41.12 (Dec. 2013), pp. 2603–2616. ISSN: 1573-9686 (Electronic). DOI: 10.1007/s10439-013-0853-z.

[68] Matteo Astorino et al. "A robust and efficient valve model based on resistive immersed surfaces." eng. In: *Int. j. numer. method. biomed. eng.* 28.9 (Sept. 2012), pp. 937–959. ISSN: 2040-7947 (Electronic). DOI: 10.1002/cnm.2474.

[69] Shawn C Shadden, Matteo Astorino, and Jean-Frédéric Gerbeau. "Computational analysis of an aortic valve jet with Lagrangian coherent structures." eng. In: *Chaos* 20.1 (Mar. 2010), p. 17512. ISSN: 1089-7682 (Electronic). DOI: 10.1063/1.3272780.

[70] Mohammadreza Soltany Sadrabadi et al. "Fluid-structure coupled biotransport processes in aortic valve disease". In: *J. Biomech.* (2021), p. 110239. ISSN: 0021-9290. DOI: https://doi.org/10.1016/j.jbiomech.2021.110239. URL: http://www.sciencedirect.com/science/article/pii/S0021929021000191.

[71] Z Xu et al. "Study of blood flow impact on growth of thrombi using a multiscale model". In: *Soft Matter* 5 (2009), pp. 769–779.

[72] Onur Mutlu et al. "Evaluating the Effectiveness of 2 Different Flow Diverter Stents Based on the Stagnation Region Formation in an Aneurysm Sac Using Lagrangian Coherent Structure." eng. In: *World Neurosurg.* 127 (July 2019), e727–e737. ISSN: 1878-8769 (Electronic). DOI: 10.1016/j.wneu.2019.03.255.

[73] Onur Mutlu et al. "Evaluating the Effect of the Number of Wire of Flow Diverter Stents on the Nonstagnated Region Formation in an Aneurysm Sac Using Lagrangian Coherent Structure and Hyperbolic Time Analysis." eng. In: *World Neurosurg.* 133 (Jan. 2020), e666–e682. ISSN: 1878-8769 (Electronic). DOI: 10.1016/j.wneu.2019.09.116.

[74] C G Caro, J M Fitz-Gerald, and R C Schroter. "Atheroma and arterial wall shear. Observation, correlation and proposal of a shear dependent mass transfer mechanism for atherogenesis." eng. In: *Proc. R. Soc. London. Ser. B, Biol. Sci.* 177.1046 (Feb. 1971), pp. 109–159. ISSN: 0950-1193 (Print). DOI: 10.1098/rspb.1971.0019.

[75] Brenda R Kwak et al. “Biomechanical factors in atherosclerosis: mechanisms and clinical implications”. eng. In: *Eur. Heart J.* 35.43 (Nov. 2014), pp. 3013–3020d. ISSN: 1522-9645. DOI: 10.1093/eurheartj/ehu353.

[76] A M Gambaruto, D J Doorly, and T Yamaguchi. “Wall shear stress and near-wall convective transport: Comparisons with vascular remodelling in a peripheral graft anastomosis”. In: *J. Comput. Phys.* 229.14 (2010), pp. 5339–5356. ISSN: 00219991. DOI: 10.1016/j.jcp.2010.03.029. URL: http://dx.doi.org/10.1016/j.jcp.2010.03.029.

[77] Umberto Morbiducci et al. “Wall Shear Stress Topological Skeleton Independently Predicts Long-Term Restenosis After Carotid Bifurcation Endarterectomy”. In: *Ann. Biomed. Eng.* 48.12 (2020), pp. 2936–2949. ISSN: 15739686. DOI: 10.1007/s10439-020-02607-9.

[78] Karol Calo et al. “Spatiotemporal Hemodynamic Complexity in Carotid Arteries: An Integrated Computational Hemodynamics and Complex Networks-Based Approach.” eng. In: *IEEE Trans. Biomed. Eng.* 67.7 (July 2020), pp. 1841–1853. ISSN: 1558-2531 (Electronic). DOI: 10.1109/TBME.2019.2949148.

[79] C K Zarins et al. “Carotid bifurcation atherosclerosis. Quantitative correlation of plaque localization with flow velocity profiles and wall shear stress.” eng. In: *Circ. Res.* 53.4 (Oct. 1983), pp. 502–514. ISSN: 0009-7330 (Print).

[80] Shigeru Tada. “Numerical study of oxygen transport in a carotid bifurcation.” eng. In: *Phys. Med. Biol.* 55.14 (July 2010), pp. 3993–4010. ISSN: 1361-6560 (Electronic). DOI: 10.1088/0031-9155/55/14/004.

[81] Giuseppe De Nisco et al. “What is needed to make low-density lipoprotein transport in human aorta computational models suitable to explore links to atherosclerosis? Impact of initial and inflow boundary conditions.” eng. In: *J. Biomech.* 68 (Feb. 2018), pp. 33–42. ISSN: 1873-2380 (Electronic). DOI: 10.1016/j.jbiomech.2017.12.009.

[82] Luca Formaggia, Karl Perktold, and Alfio Quarteroni. “Basic mathematical models and motivations”. In: *Cardiovasc. Math. Model. Simul. Circ. Syst.* Ed. by Luca Formaggia, Alfio Quarteroni, and Alessandro Veneziani. Milano: Springer Milan, 2009, pp. 47–75. ISBN: 978-88-470-1152-6. DOI: 10.1007/

978-88-470-1152-6_2. URL: https://doi.org/10.1007/978-88-470-1152-6%7B%5C_%7D2.

[83] Roger Temam. *Navier–Stokes Equations and Nonlinear Functional Analysis*. Society for Industrial and Applied Mathematics, 1995. DOI: 10.1137/1.9781611970050. URL: https://epubs.siam.org/doi/abs/10.1137/1.9781611970050.

[84] F D Goes, Mathieu Desbrun, and Y Tong. "Vector field processing on triangle meshes". In: *SIGGRAPH '16*. 2016.

[85] Harsh Bhatia et al. "Topological Methods in Data Analysis and Visualization III". In: (2014), pp. 3–18. DOI: 10.1007/978-3-319-04099-8. URL: http://link.springer.com/10.1007/978-3-319-04099-8.

[86] X Tricoche et al. "Topology tracking for the visualization of time-dependent two-dimensional flows". In: *Comput. Graph.* 26.2 (2002), pp. 249–257. ISSN: 00978493. DOI: 10.1016/S0097-8493(02)00056-0.

[87] Wentao Wang, Wenke Wang, and Sikun Li. "Detection and classification of critical points in piecewise linear vector fields". In: *J. Vis.* 21.1 (Feb. 2018), pp. 147–161. ISSN: 1875-8975. DOI: 10.1007/s12650-017-0438-2. URL: https://doi.org/10.1007/s12650-017-0438-2.

[88] G Nave and S Ross. "Trajectory-free calculation of attracting and repelling manifolds". In: 2017.

[89] Yiemeng Hoi et al. "Effect of common carotid artery inlet length on normal carotid bifurcation hemodynamics." eng. In: *J. Biomech. Eng.* 132.12 (Dec. 2010), p. 121008. ISSN: 1528-8951 (Electronic). DOI: 10.1115/1.4002800.

[90] Diego Gallo, David A Steinman, and Umberto Morbiducci. "An insight into the mechanistic role of the common carotid artery on the hemodynamics at the carotid bifurcation." eng. In: *Ann. Biomed. Eng.* 43.1 (Jan. 2015), pp. 68–81. ISSN: 1573-9686 (Electronic). DOI: 10.1007/s10439-014-1119-0.

[91] Lars Bo Nielsen. "Transfer of low density lipoprotein into the arterial wall and risk of atherosclerosis". In: *Atherosclerosis* 123.1 (1996), pp. 1–15. ISSN: 0021-9150. DOI: https://doi.org/10.1016/0021-9150(96)05802-9. URL: http://www.sciencedirect.com/science/article/pii/0021915096058029.

[92] P. E. Vincent and P. D. Weinberg. "Flow-dependent concentration polarization and the endothelial glycocalyx layer: Multi-scale aspects of arterial mass transport and their implications for atherosclerosis". In: *Biomech. Model. Mechanobiol.* 13.2 (2014), pp. 313–326. ISSN: 16177940. DOI: 10.1007/s10237-013-0512-1.

[93] Jonas Lantz and Matts Karlsson. "Large eddy simulation of LDL surface concentration in a subject specific human aorta." eng. In: *J. Biomech.* 45.3 (Feb. 2012), pp. 537–542. ISSN: 1873-2380 (Electronic). DOI: 10.1016/j.jbiomech.2011.11.039.

[94] Xiaoyin Li et al. "Numerical simulation of haemodynamics and low-density lipoprotein transport in the rabbit aorta and their correlation with atherosclerotic plaque thickness." eng. In: *J. R. Soc. Interface* 14.129 (Apr. 2017). ISSN: 1742-5662 (Electronic). DOI: 10.1098/rsif.2017.0140.

[95] Xiao Liu et al. "A numerical study on the flow of blood and the transport of LDL in the human aorta: the physiological significance of the helical flow in the aortic arch." eng. In: *Am. J. Physiol. Heart Circ. Physiol.* 297.1 (July 2009), H163–70. ISSN: 1522-1539 (Electronic). DOI: 10.1152/ajpheart.00266.2009.

[96] Mirza Md Symon Reza and Amirhossein Arzani. "A critical comparison of different residence time measures in aneurysms." eng. In: *J. Biomech.* (Mar. 2019). ISSN: 1873-2380 (Electronic). DOI: 10.1016/j.jbiomech.2019.03.028.

[97] D Gallo et al. "On the use of in vivo measured flow rates as boundary conditions for image-based hemodynamic models of the human aorta: implications for indicators of abnormal flow." eng. In: *Ann. Biomed. Eng.* 40.3 (Mar. 2012), pp. 729–741. ISSN: 1573-9686 (Electronic). DOI: 10.1007/s10439-011-0431-1.

[98] Umberto Morbiducci et al. "Inflow boundary conditions for image-based computational hemodynamics: impact of idealized versus measured velocity profiles in the human aorta." eng. In: *J. Biomech.* 46.1 (Jan. 2013), pp. 102–109. ISSN: 1873-2380 (Electronic). DOI: 10.1016/j.jbiomech.2012.10.012.

[99] Ning Yang and Kambiz Vafai. "Modeling of low-density lipoprotein (LDL) transport in the artery—effects of hypertension". In: *Int. J. Heat Mass Transf.* 49.5 (2006), pp. 850–867. ISSN: 0017-9310. DOI: https://doi.org/10.1016/j.ijheatmasstransfer.2005.09.019. URL: http://www.sciencedirect.com/science/article/pii/S0017931005005958.

[100] Amirhossein Arzani and Shawn C Shadden. "Characterizations and Correlations of Wall Shear Stress in Aneurysmal Flow." eng. In: *J. Biomech. Eng.* 138.1 (Jan. 2016). ISSN: 1528-8951 (Electronic). DOI: 10.1115/1.4032056.

[101] P.D. Minev and C. Ross Ethier. "A characteristic/finite element algorithm for the 3-D Navier–Stokes equations using unstructured grids". In: *Comput. Methods Appl. Mech. Eng.* 178.1-2 (1999), pp. 39–50. ISSN: 00457825. DOI: 10.1016/s0045-7825(99)00003-1.

[102] C Chnafa et al. "Errors in power-law estimations of inflow rates for intracranial aneurysm CFD." In: *J. Biomech.* 80 (2018), pp. 159–165. ISSN: 1873-2380. DOI: 10.1016/j.jbiomech.2018.09.006. URL: http://www.ncbi.nlm.nih.gov/pubmed/30243498.

[103] Mikael Mortensen and Kristian Valen-Sendstad. "Oasis: A high-level/high-performance open source Navier–Stokes solver". In: *Comput. Phys. Commun.* 188 (2015). DOI: 10.1016/j.cpc.2014.10.026.

[104] K Valen-Sendstad and D A Steinman. "Mind the gap: impact of computational fluid dynamics solution strategy on prediction of intracranial aneurysm hemodynamics and rupture status indicators." eng. In: *AJNR. Am. J. Neuroradiol.* 35.3 (Mar. 2014), pp. 536–543. ISSN: 1936-959X (Electronic). DOI: 10.3174/ajnr.A3793.

[105] X He and D N Ku. "Pulsatile flow in the human left coronary artery bifurcation: average conditions." eng. In: *J. Biomech. Eng.* 118.1 (Feb. 1996), pp. 74–82. ISSN: 0148-0731 (Print).

[106] Steffen Oeltze-Jafra et al. "Cluster Analysis of Vortical Flow in Simulations of Cerebral Aneurysm Hemodynamics." eng. In: *IEEE Trans. Vis. Comput. Graph.* 22.1 (Jan. 2016), pp. 757–766. ISSN: 1941-0506 (Electronic). DOI: 10.1109/TVCG.2015.2467203.

[107] Liang Der Jou et al. “Wall shear stress on ruptured and unruptured intracranial aneurysms at the internal carotid artery”. In: *Am. J. Neuroradiol.* 29.9 (2008), pp. 1761–1767. ISSN: 01956108. DOI: 10.3174/ajnr.A1180.

[108] D N Ku et al. “Pulsatile flow and atherosclerosis in the human carotid bifurcation. Positive correlation between plaque location and low oscillating shear stress.” eng. In: *Arteriosclerosis* 5.3 (1985), pp. 293–302. ISSN: 0276-5047 (Print). DOI: 10.1161/01.atv.5.3.293.

[109] A R Naylor et al. “Editor’s Choice - Management of Atherosclerotic Carotid and Vertebral Artery Disease: 2017 Clinical Practice Guidelines of the European Society for Vascular Surgery (ESVS).” eng. In: *Eur. J. Vasc. Endovasc. Surg. Off. J. Eur. Soc. Vasc. Surg.* 55.1 (Jan. 2018), pp. 3–81. ISSN: 1532-2165 (Electronic). DOI: 10.1016/j.ejvs.2017.06.021.

[110] Willem E. Hellings et al. “Histological characterization of restenotic carotid plaques in relation to recurrence interval and clinical presentation: A cohort study”. In: *Stroke* 39.3 (2008), pp. 1029–1032. ISSN: 00392499. DOI: 10.1161/STROKEAHA.107.496703.

[111] H. Frericks et al. “Carotid recurrent stenosis and risk of ipsilateral stroke: A systematic review of the literature”. In: *Stroke* 29.1 (1998), pp. 244–250. ISSN: 00392499. DOI: 10.1161/01.STR.29.1.244.

[112] Charles A. Taylor and David A. Steinman. “Image-based modeling of blood flow and vessel wall dynamics: Applications, methods and future directions: Sixth international bio-fluid mechanics symposium and workshop, March 28-30, 2008 Pasadena, California”. In: *Ann. Biomed. Eng.* 38.3 (2010), pp. 1188–1203. ISSN: 00906964. DOI: 10.1007/s10439-010-9901-0.

[113] Maurizio Domanin et al. “Prediction of Long Term Restenosis Risk After Surgery in the Carotid Bifurcation by Hemodynamic and Geometric Analysis”. In: *Ann. Biomed. Eng.* 47.4 (2019), pp. 1129–1140. ISSN: 15739686. DOI: 10.1007/s10439-019-02201-8.

[114] Maurizio Domanin et al. “Computational fluid dynamic comparison between patch-based and primary closure techniques after carotid endarterectomy”. In: *J. Vasc. Surg.* 67.3 (2018), pp. 887–897. ISSN: 10976809. DOI: 10.1016/j.jvs.2017.08.094. URL: https://doi.org/10.1016/j.jvs.2017.08.094.

[115] Maurizio Domanin et al. "Computational Fluid-Dynamic Analysis after Carotid Endarterectomy: Patch Graft versus Direct Suture Closure". In: *Ann. Vasc. Surg.* 44 (2017), pp. 325–335. ISSN: 0890-5096. DOI: https://doi.org/10.1016/j.avsg.2017.04.016. URL: http://www.sciencedirect.com/science/article/pii/S0890509616308998.

[116] Ali F. AbuRahma et al. "Proposed duplex velocity criteria for carotid restenosis following carotid endarterectomy with patch closure". In: *J. Vasc. Surg.* 50.2 (2009), 286–291.e2. ISSN: 07415214. DOI: 10.1016/j.jvs.2009.01.065. URL: http://dx.doi.org/10.1016/j.jvs.2009.01.065.

[117] Bruno Guerciotti et al. "Computational study of the fluid-dynamics in carotids before and after endarterectomy". In: *J. Biomech.* 49.1 (2016), pp. 26–38. ISSN: 0021-9290. DOI: https://doi.org/10.1016/j.jbiomech.2015.11.009. URL: http://www.sciencedirect.com/science/article/pii/S0021929015006399.

[118] Sang Wook Lee and David A. Steinman. "On the relative importance of rheology for image-based CFD models of the carotid bifurcation". In: *J. Biomech. Eng.* (2007). ISSN: 01480731. DOI: 10.1115/1.2540836.

[119] Umberto Morbiducci et al. "On the importance of blood rheology for bulk flow in hemodynamic models of the carotid bifurcation". In: *J. Biomech.* 44.13 (2011), pp. 2427–2438. ISSN: 0021-9290. DOI: https://doi.org/10.1016/j.jbiomech.2011.06.028. URL: http://www.sciencedirect.com/science/article/pii/S0021929011004787.

[120] David A. Steinman et al. "Reconstruction of carotid bifurcation hemodynamics and wall thickness using computational fluid dynamics and MRI". In: *Magn. Reson. Med.* 47.1 (2002), pp. 149–159. ISSN: 07403194. DOI: 10.1002/mrm.10025.

[121] Luca Antiga et al. "An image-based modeling framework for patient-specific computational hemodynamics". In: *Med. Biol. Eng. Comput.* 46.11 (2008), pp. 1097–1112. ISSN: 01400118. DOI: 10.1007/s11517-008-0420-1.

[122] Sang Wook Lee et al. "Geometry of the carotid bifurcation predicts its exposure to disturbed flow". In: *Stroke* 39.8 (2008), pp. 2341–2347. ISSN: 00392499. DOI: 10.1161/STROKEAHA.107.510644.

[123] Sang Wook Lee and David A. Steinman. "On the relative importance of rheology for image-based CFD models of the carotid bifurcation". In: *J. Biomech. Eng.* 129.2 (2007), pp. 273–278. ISSN: 01480731. DOI: 10.1115/1.2540836.

[124] Payam B Bijari et al. "Improved prediction of disturbed flow via hemodynamically-inspired geometric variables." eng. In: *J. Biomech.* 45.9 (June 2012), pp. 1632–1637. ISSN: 1873-2380 (Electronic). DOI: 10.1016/j.jbiomech.2012.03.030.

[125] Jordi Martorell et al. "Extent of flow recirculation governs expression of atherosclerotic and thrombotic biomarkers in arterial bifurcations". In: *Cardiovasc. Res.* 103.1 (2014), pp. 37–46. ISSN: 17553245. DOI: 10.1093/cvr/cvu124.

[126] Rocco Michele Lancellotti et al. "Large eddy simulations for blood dynamics in realistic stenotic carotids." eng. In: *Int. j. numer. method. biomed. eng.* 33.11 (Nov. 2017). ISSN: 2040-7947 (Electronic). DOI: 10.1002/cnm.2868.

[127] Eric M Isselbacher. "Thoracic and abdominal aortic aneurysms." eng. In: *Circulation* 111.6 (Feb. 2005), pp. 816–828. ISSN: 1524-4539 (Electronic). DOI: 10.1161/01.CIR.0000154569.08857.7A.

[128] Raimund Erbel et al. "2014 ESC guidelines on the diagnosis and treatment of aortic diseases". In: *Eur. Heart J.* 35.41 (2014), pp. 2873–2926. ISSN: 15229645. DOI: 10.1093/eurheartj/ehu281.

[129] M. A. Coady et al. "Surgical intervention criteria for thoracic aortic aneurysms: A study of growth rates and complications". In: *Ann. Thorac. Surg.* 67.6 (1999), pp. 1922–1926. ISSN: 00034975. DOI: 10.1016/S0003-4975(99)00431-2.

[130] Gunnar Johansson, Ulf Markström, and Jesper Swedenborg. "Ruptured thoracic aortic aneurysms: A study of incidence and mortality rates". In: *J. Vasc. Surg.* 21.6 (1995), pp. 985–988. ISSN: 07415214. DOI: 10.1016/S0741-5214(95)70227-X.

[131] Linda A Pape et al. "Aortic diameter >or = 5.5 cm is not a good predictor of type A aortic dissection: observations from the International Registry of Acute Aortic Dissection (IRAD)." eng. In: *Circulation* 116.10 (Sept. 2007),

pp. 1120–1127. ISSN: 1524-4539 (Electronic). DOI: 10.1161/CIRCULATIONAHA.107.702720.

[132] Katherine H Chau and John A Elefteriades. "Natural history of thoracic aortic aneurysms: size matters, plus moving beyond size." eng. In: *Prog. Cardiovasc. Dis.* 56.1 (2013), pp. 74–80. ISSN: 1873-1740 (Electronic). DOI: 10.1016/j.pcad.2013.05.007.

[133] John A Elefteriades and Emily A Farkas. "Thoracic aortic aneurysm clinically pertinent controversies and uncertainties." eng. In: *J. Am. Coll. Cardiol.* 55.9 (Mar. 2010), pp. 841–857. ISSN: 1558-3597 (Electronic). DOI: 10.1016/j.jacc.2009.08.084.

[134] Michael P Poullis et al. "Ascending aortic curvature as an independent risk factor for type A dissection, and ascending aortic aneurysm formation: a mathematical model." eng. In: *Eur. J. Cardiothorac. Surg.* 33.6 (June 2008), pp. 995–1001. ISSN: 1010-7940 (Print). DOI: 10.1016/j.ejcts.2008.02.029.

[135] Alessia Gallo et al. "On the prospect of serum exosomal miRNA profiling and protein biomarkers for the diagnosis of ascending aortic dilatation in patients with bicuspid and tricuspid aortic valve." eng. In: *Int. J. Cardiol.* 273 (Dec. 2018), pp. 230–236. ISSN: 1874-1754 (Electronic). DOI: 10.1016/j.ijcard.2018.10.005.

[136] Valentina Agnese et al. "Patterns of ascending aortic dilatation and predictors of surgical replacement of the aorta: A comparison of bicuspid and tricuspid aortic valve patients over eight years of follow-up." eng. In: *J. Mol. Cell. Cardiol.* 135 (Oct. 2019), pp. 31–39. ISSN: 1095-8584 (Electronic). DOI: 10.1016/j.yjmcc.2019.07.010.

[137] Salvatore Pasta et al. "In Vivo Strain Analysis of Dilated Ascending Thoracic Aorta by ECG-Gated CT Angiographic Imaging". In: *Ann. Biomed. Eng.* 45.12 (2017), pp. 2911–2920. ISSN: 15739686. DOI: 10.1007/s10439-017-1915-4.

[138] Jessica E Wagenseil. "Bio-chemo-mechanics of thoracic aortic aneurysms". In: *Curr. Opin. Biomed. Eng.* 5 (2018), pp. 50–57. ISSN: 2468-4511. DOI: https://doi.org/10.1016/j.cobme.2018.01.002. URL: http://www.sciencedirect.com/science/article/pii/S2468451117300764.

[139] Claudie Petit, S Jamaleddin Mousavi, and Stéphane Avril. "Chapter 6 - Review of the Essential Roles of SMCs in ATAA Biomechanics". In: *Adv. Biomech. Tissue Regen.* Ed. by Mohamed H Doweidar. Academic Press, 2019, pp. 95–114. ISBN: 978-0-12-816390-0. DOI: https://doi.org/10.1016/B978-0-12-816390-0.00006-6. URL: http://www.sciencedirect.com/science/article/pii/B9780128163900000066.

[140] Emilie Bollache et al. "Aortic valve-mediated wall shear stress is heterogeneous and predicts regional aortic elastic fiber thinning in bicuspid aortic valve-associated aortopathy". In: *J. Thorac. Cardiovasc. Surg.* 156.6 (2018), 2112–2120.e2. ISSN: 1097685X. DOI: 10.1016/j.jtcvs.2018.05.095. URL: https://doi.org/10.1016/j.jtcvs.2018.05.095.

[141] Kenichiro Suwa et al. "Effect of Aortic Valve Disease on 3D Hemodynamics in Patients With Aortic Dilation and Trileaflet Aortic Valve Morphology." eng. In: *J. Magn. Reson. Imaging* 51.2 (Feb. 2020), pp. 481–491. ISSN: 1522-2586 (Electronic). DOI: 10.1002/jmri.26804.

[142] Lydia Dux-Santoy et al. "Increased rotational flow in the proximal aortic arch is associated with its dilation in bicuspid aortic valve disease." eng. In: *Eur. Heart J. Cardiovasc. Imaging* 20.12 (Dec. 2019), pp. 1407–1417. ISSN: 2047-2412 (Electronic). DOI: 10.1093/ehjci/jez046.

[143] José Fernando Rodríguez-Palomares et al. "Aortic flow patterns and wall shear stress maps by 4D-flow cardiovascular magnetic resonance in the assessment of aortic dilatation in bicuspid aortic valve disease". In: *J. Cardiovasc. Magn. Reson.* 20.1 (2018), p. 28. ISSN: 1532429X. DOI: 10.1186/s12968-018-0451-1.

[144] Pouya Youssefi et al. "Impact of Patient-Specific Inflow Velocity Profile on Hemodynamics of the Thoracic Aorta." eng. In: *J. Biomech. Eng.* 140.1 (Jan. 2018). ISSN: 1528-8951 (Electronic). DOI: 10.1115/1.4037857.

[145] S. Pasta et al. "In Silico Shear and Intramural Stresses are Linked to Aortic Valve Morphology in Dilated Ascending Aorta". In: *Eur. J. Vasc. Endovasc. Surg.* 54.2 (2017), pp. 254–263. ISSN: 15322165. DOI: 10.1016/j.ejvs.2017.05.016. URL: http://dx.doi.org/10.1016/j.ejvs.2017.05.016.

[146] Vincent Mendez, Marzio Di Giuseppe, and Salvatore Pasta. "Comparison of hemodynamic and structural indices of ascending thoracic aortic aneurysm as predicted by 2-way FSI, CFD rigid wall simulation and patient-specific displacement-based FEA". In: *Comput. Biol. Med.* 100 (2018), pp. 221–229. ISSN: 0010-4825. DOI: https://doi.org/10.1016/j.compbiomed.2018.07.013. URL: http://www.sciencedirect.com/science/article/pii/S001048251830204X.

[147] Francesca Condemi et al. "Ascending thoracic aorta aneurysm repair induces positive hemodynamic outcomes in a patient with unchanged bicuspid aortic valve." eng. In: *J. Biomech.* 81 (Nov. 2018), pp. 145–148. ISSN: 1873-2380 (Electronic). DOI: 10.1016/j.jbiomech.2018.09.022.

[148] F. Condemi et al. "Fluid- and Biomechanical Analysis of Ascending Thoracic Aorta Aneurysm with Concomitant Aortic Insufficiency". In: *Ann. Biomed. Eng.* 45.12 (2017), pp. 2921–2932. ISSN: 15739686. DOI: 10.1007/s10439-017-1913-6.

[149] Jonas Burk et al. "Evaluation of 3D blood flow patterns and wall shear stress in the normal and dilated thoracic aorta using flow-sensitive 4D CMR." eng. In: *J. Cardiovasc. Magn. Reson.* 14 (Dec. 2012), p. 84. ISSN: 1532-429X (Electronic). DOI: 10.1186/1532-429X-14-84.

[150] David G Guzzardi et al. "Valve-Related Hemodynamics Mediate Human Bicuspid Aortopathy: Insights From Wall Shear Stress Mapping". In: *J. Am. Coll. Cardiol.* 66.8 (2015), pp. 892–900. ISSN: 0735-1097. DOI: https://doi.org/10.1016/j.jacc.2015.06.1310. URL: http://www.sciencedirect.com/science/article/pii/S0735109715042230.

[151] Solmaz Farzaneh, Olfa Trabelsi, and Stephane Avril. "Inverse identification of local stiffness across ascending thoracic aortic aneurysms." eng. In: *Biomech. Model. Mechanobiol.* 18.1 (Feb. 2019), pp. 137–153. ISSN: 1617-7940 (Electronic). DOI: 10.1007/s10237-018-1073-0.

[152] Desmond Dillon-Murphy et al. "Multi-modality image-based computational analysis of haemodynamics in aortic dissection." eng. In: *Biomech. Model. Mechanobiol.* 15.4 (Aug. 2016), pp. 857–876. ISSN: 1617-7940 (Electronic). DOI: 10.1007/s10237-015-0729-2.

[153] Adam Updegrove et al. "SimVascular: An Open Source Pipeline for Cardiovascular Simulation." eng. In: *Ann. Biomed. Eng.* 45.3 (Mar. 2017), pp. 525–541. ISSN: 1573-9686 (Electronic). DOI: 10.1007/s10439-016-1762-8.

[154] Giuseppe De Nisco et al. "The Atheroprotective Nature of Helical Flow in Coronary Arteries." eng. In: *Ann. Biomed. Eng.* 47.2 (Feb. 2019), pp. 425–438. ISSN: 1573-9686 (Electronic). DOI: 10.1007/s10439-018-02169-x.

[155] Giuseppe De Nisco et al. "The impact of helical flow on coronary atherosclerotic plaque development". In: *Atherosclerosis* (Feb. 2020). ISSN: 0021-9150. DOI: 10.1016/J.ATHEROSCLEROSIS.2020.01.027.

[156] Nusrat Choudhury et al. "Local mechanical and structural properties of healthy and diseased human ascending aorta tissue". In: *Cardiovasc. Pathol.* 18.2 (2009), pp. 83–91. ISSN: 1054-8807. DOI: https://doi.org/10.1016/j.carpath.2008.01.001. URL: http://www.sciencedirect.com/science/article/pii/S1054880708000100.

[157] Jean Baptiste Michel, Guillaume Jondeau, and DIanna M. Milewicz. "From genetics to response to injury: Vascular smooth muscle cells in aneurysms and dissections of the ascending aorta". In: *Cardiovasc. Res.* 114.4 (2018), pp. 578–589. ISSN: 17553245. DOI: 10.1093/cvr/cvy006.

[158] A M Shaaban and A J Duerinckx. "Wall shear stress and early atherosclerosis: a review." eng. In: *AJR. Am. J. Roentgenol.* 174.6 (June 2000), pp. 1657–1665. ISSN: 0361-803X (Print). DOI: 10.2214/ajr.174.6.1741657.

[159] Naoya Sakamoto et al. "Effect of spatial gradient in fluid shear stress on morphological changes in endothelial cells in response to flow." eng. In: *Biochem. Biophys. Res. Commun.* 395.2 (Apr. 2010), pp. 264–269. ISSN: 1090-2104 (Electronic). DOI: 10.1016/j.bbrc.2010.04.002.

[160] John M Tarbell. "Shear stress and the endothelial transport barrier." eng. In: *Cardiovasc. Res.* 87.2 (July 2010), pp. 320–330. ISSN: 1755-3245 (Electronic). DOI: 10.1093/cvr/cvq146.

[161] Francesca Condemi et al. "Relationship between Ascending Thoracic Aortic Aneurysms Hemodynamics and Biomechanical Properties". In: *IEEE Trans. Biomed. Eng.* 67.4 (2020), pp. 949–956. ISSN: 15582531. DOI: 10.1109/TBME.2019.2924955.

[162] Antonino Rinaudo and Salvatore Pasta. "Regional variation of wall shear stress in ascending thoracic aortic aneurysms." eng. In: *Proc. Inst. Mech. Eng. Part H, J. Eng. Med.* 228.6 (June 2014), pp. 627–638. ISSN: 2041-3033 (Electronic). DOI: 10.1177/0954411914540877.

[163] Salvatore Pasta et al. "Shear Stress and Aortic Strain Associations With Biomarkers of Ascending Thoracic Aortic Aneurysm." eng. In: *Ann. Thorac. Surg.* 110.5 (Nov. 2020), pp. 1595–1604. ISSN: 1552-6259 (Electronic). DOI: 10.1016/j.athoracsur.2020.03.017.

[164] Yi Liu et al. "Surrounding tissues affect the passive mechanics of the vessel wall: Theory and experiment". In: *Am. J. Physiol. - Hear. Circ. Physiol.* 293.6 (2007), pp. 3290–3300. ISSN: 03636135. DOI: 10.1152/ajpheart.00666.2007.

[165] O Trabelsi et al. "A non-invasive methodology for ATAA rupture risk estimation." eng. In: *J. Biomech.* 66 (Jan. 2018), pp. 119–126. ISSN: 1873-2380 (Electronic). DOI: 10.1016/j.jbiomech.2017.11.012.

[166] A Franquet et al. "A New Method for the In Vivo Identification of Mechanical Properties in Arteries From Cine MRI Images: Theoretical Framework and Validation". In: *IEEE Trans. Med. Imaging* 32.8 (2013), pp. 1448–1461. ISSN: 1558-254X. DOI: 10.1109/TMI.2013.2257828.

[167] Solmaz Farzaneh et al. "Identifying Local Arterial Stiffness to Assess the Risk of Rupture of Ascending Thoracic Aortic Aneurysms". In: *Ann. Biomed. Eng.* 47.4 (2019), pp. 1038–1050. ISSN: 15739686. DOI: 10.1007/s10439-019-02204-5.

[168] Andreas Wittek et al. "Cyclic three-dimensional wall motion of the human ascending and abdominal aorta characterized by time-resolved three-dimensional ultrasound speckle tracking". In: *Biomech. Model. Mechanobiol.* 15.5 (2016), pp. 1375–1388. ISSN: 16177940. DOI: 10.1007/s10237-016-0769-2.

[169] Arvin Arani et al. "Cardiac MR elastography for quantitative assessment of elevated myocardial stiffness in cardiac amyloidosis". In: *J. Magn. Reson. Imaging* 46.5 (2017), pp. 1361–1367. ISSN: 15222586. DOI: 10.1002/jmri.25678.

[170] Alex Frydrychowicz et al. "Interdependencies of aortic arch secondary flow patterns, geometry, and age analysed by 4-dimensional phase contrast magnetic resonance imaging at 3 Tesla". In: *Eur. Radiol.* 22.5 (2012), pp. 1122–1130. ISSN: 09387994. DOI: 10.1007/s00330-011-2353-6.

[171] Diego Gallo et al. "Analysis of thoracic aorta hemodynamics using 3D particle tracking velocimetry and computational fluid dynamics". In: *J. Biomech.* 47.12 (2014), pp. 3149–3155. ISSN: 0021-9290. DOI: https://doi.org/10.1016/j.jbiomech.2014.06.017. URL: http://www.sciencedirect.com/science/article/pii/S002192901400356X.

[172] U Gülan et al. "Experimental Investigation of the Influence of the Aortic Stiffness on Hemodynamics in the Ascending Aorta". In: *IEEE J. Biomed. Heal. Informatics* 18.6 (Nov. 2014), pp. 1775–1780. ISSN: 2168-2208. DOI: 10.1109/JBHI.2014.2322934.

[173] Jaryl Ng et al. "Local Hemodynamic Forces After Stenting: Implications on Restenosis and Thrombosis." eng. In: *Arterioscler. Thromb. Vasc. Biol.* 37.12 (Dec. 2017), pp. 2231–2242. ISSN: 1524-4636 (Electronic). DOI: 10.1161/ATVBAHA.117.309728.

[174] Claudio Chiastra et al. "Computational fluid dynamic simulations of image-based stented coronary bifurcation models". In: *J. R. Soc. Interface* 10.84 (2013). ISSN: 17425662. DOI: 10.1098/rsif.2013.0193.

[175] Jolanda J Wentzel et al. "The influence of shear stress on in-stent restenosis and thrombosis." eng. In: *EuroIntervention J. Eur. Collab. with Work. Gr. Interv. Cardiol. Eur. Soc. Cardiol.* 4 Suppl C (Aug. 2008), pp. C27–32. ISSN: 1774-024X (Print).

[176] Kim Van der Heiden et al. "The effects of stenting on shear stress: relevance to endothelial injury and repair." eng. In: *Cardiovasc. Res.* 99.2 (July 2013), pp. 269–275. ISSN: 1755-3245 (Electronic). DOI: 10.1093/cvr/cvt090.

[177] Jonathan Murphy and Fergal Boyle. "Predicting neointimal hyperplasia in stented arteries using time-dependant computational fluid dynamics: a review." eng. In: *Comput. Biol. Med.* 40.4 (Apr. 2010), pp. 408–418. ISSN: 1879-0534 (Electronic). DOI: 10.1016/j.compbiomed.2010.02.005.

[178] Nicolas Foin et al. "Incomplete stent apposition causes high shear flow disturbances and delay in neointimal coverage as a function of strut to wall detachment distance: implications for the management of incomplete stent apposition." eng. In: *Circ. Cardiovasc. Interv.* 7.2 (Apr. 2014), pp. 180–189. ISSN: 1941-7632 (Electronic). DOI: 10.1161/CIRCINTERVENTIONS.113.000931.

[179] Anne Cornelissen et al. "Histopathologic and physiologic effect of bifurcation stenting: current status and future prospects." eng. In: *Expert Rev. Med. Devices* 17.3 (Mar. 2020), pp. 189–200. ISSN: 1745-2422 (Electronic). DOI: 10.1080/17434440.2020.1733410.

[180] P W Longest and C Kleinstreuer. "Computational haemodynamics analysis and comparison study of arterio-venous grafts." eng. In: *J. Med. Eng. Technol.* 24.3 (2000), pp. 102–110. ISSN: 0309-1902 (Print). DOI: 10.1080/03091900050135013.

[181] Benoît Melchior and John A Frangos. "Shear-induced endothelial cell-cell junction inclination." eng. In: *Am. J. Physiol. Cell Physiol.* 299.3 (Sept. 2010), pp. C621–9. ISSN: 1522-1563 (Electronic). DOI: 10.1152/ajpcell.00156.2010.

[182] Sarah T Hsiao et al. "Endothelial repair in stented arteries is accelerated by inhibition of Rho-associated protein kinase." eng. In: *Cardiovasc. Res.* 112.3 (Dec. 2016), pp. 689–701. ISSN: 1755-3245 (Electronic). DOI: 10.1093/cvr/cvw210.

[183] Jolanda J Wentzel et al. "Endothelial shear stress in the evolution of coronary atherosclerotic plaque and vascular remodelling: current understanding and remaining questions". In: *Cardiovasc. Res.* 96.2 (Nov. 2012), pp. 234–243. ISSN: 0008-6363. DOI: 10.1093/cvr/cvs217.

[184] C L Feldman and P H Stone. "Intravascular hemodynamic factors responsible for progression of coronary atherosclerosis and development of vulnerable plaque." eng. In: *Curr. Opin. Cardiol.* 15.6 (Nov. 2000), pp. 430–440. ISSN: 0268-4705 (Print). DOI: 10.1097/00001573-200011000-00010.

[185] Adam J Brown et al. *Role of biomechanical forces in the natural history of coronary atherosclerosis*. eng. England, Apr. 2016. DOI: 10.1038/nrcardio.2015.203.

[186] Habib Samady et al. "Coronary artery wall shear stress is associated with progression and transformation of atherosclerotic plaque and arterial remodeling in patients with coronary artery disease." eng. In: *Circulation* 124.7 (Aug. 2011), pp. 779–788. ISSN: 1524-4539 (Electronic). DOI: 10.1161/CIRCULATIONAHA.111.021824.

[187] Farhad Rikhtegar et al. "Choosing the optimal wall shear parameter for the prediction of plaque location-A patient-specific computational study in human left coronary arteries." eng. In: *Atherosclerosis* 221.2 (Apr. 2012), pp. 432–437. ISSN: 1879-1484 (Electronic). DOI: 10.1016/j.atherosclerosis.2012.01.018.

[188] Lucas H Timmins et al. "Oscillatory wall shear stress is a dominant flow characteristic affecting lesion progression patterns and plaque vulnerability in patients with coronary artery disease." eng. In: *J. R. Soc. Interface* 14.127 (Feb. 2017). ISSN: 1742-5662 (Electronic). DOI: 10.1098/rsif.2016.0972.

[189] Y Qiu and J M Tarbell. "Numerical simulation of oxygen mass transfer in a compliant curved tube model of a coronary artery." eng. In: *Ann. Biomed. Eng.* 28.1 (Jan. 2000), pp. 26–38. ISSN: 0090-6964 (Print). DOI: 10.1114/1.251.

[190] M R Kaazempur-Mofrad and C R Ethier. "Mass transport in an anatomically realistic human right coronary artery." eng. In: *Ann. Biomed. Eng.* 29.2 (Feb. 2001), pp. 121–127. ISSN: 0090-6964 (Print). DOI: 10.1114/1.1349704.

[191] Annette M. Kok et al. "The influence of multidirectional shear stress on plaque progression and composition changes in human coronary arteries". In: *EuroIntervention* 15.8 (2019), pp. 692–699. ISSN: 1774-024X. DOI: 10.4244/eij-d-18-00529.

[192] Ayla Hoogendoorn et al. "Multidirectional wall shear stress promotes advanced coronary plaque development: comparing five shear stress metrics". In: *Cardiovasc. Res.* 116.6 (2020), pp. 1136–1146. ISSN: 17553245. DOI: 10.1093/cvr/cvz212.

[193] Karol Calò et al. "Exploring wall shear stress spatiotemporal heterogeneity in coronary arteries combining correlation-based analysis and complex networks with computational hemodynamics". In: *Proc. Inst. Mech. Eng.*

Part H J. Eng. Med. 234.11 (2020), pp. 1209–1222. ISSN: 20413033. DOI: 10.1177/0954411920923253.

[194] National Research Council. *Guide for the Care and Use of Laboratory Animals: Eighth Edition*. English. Washington: The National Academies Press, 2011. ISBN: 978-0-309-15400-0. DOI: 10.17226/12910.

[195] Claudio Chiastra et al. "Healthy and diseased coronary bifurcation geometries influence near-wall and intravascular flow: A computational exploration of the hemodynamic risk". In: *J. Biomech.* 58 (2017), pp. 79–88. ISSN: 0021-9290. DOI: https://doi.org/10.1016/j.jbiomech.2017.04.016.

[196] Yunlong Huo and Ghassan S Kassab. "Intraspecific scaling laws of vascular trees". eng. In: *J. R. Soc. Interface* 9.66 (Jan. 2012), pp. 190–200. ISSN: 1742-5662. DOI: 10.1098/rsif.2011.0270.

[197] Diego Gallo et al. "Helical flow in carotid bifurcation as surrogate marker of exposure to disturbed shear." eng. In: *J. Biomech.* 45.14 (Sept. 2012), pp. 2398–2404. ISSN: 1873-2380 (Electronic). DOI: 10.1016/j.jbiomech.2012.07.007.

[198] Umberto Morbiducci et al. "Helical flow as fluid dynamic signature for atherogenesis risk in aortocoronary bypass. A numeric study." eng. In: *J. Biomech.* 40.3 (2007), pp. 519–534. ISSN: 0021-9290 (Print). DOI: 10.1016/j.jbiomech.2006.02.017.

[199] M Lei, C Kleinstreuer, and G A Truskey. "A focal stress gradient-dependent mass transfer mechanism for atherogenesis in branching arteries." eng. In: *Med. Eng. Phys.* 18.4 (June 1996), pp. 326–332. ISSN: 1350-4533 (Print). DOI: 10.1016/1350-4533(95)00045-3.

[200] C Kleinstreuer et al. "Hemodynamic parameters and early intimal thickening in branching blood vessels." eng. In: *Crit. Rev. Biomed. Eng.* 29.1 (2001), pp. 1–64. ISSN: 0278-940X (Print). DOI: 10.1615/critrevbiomedeng.v29.i1.10.

[201] Konstantinos C Koskinas et al. "Thin-capped atheromata with reduced collagen content in pigs develop in coronary arterial regions exposed to persistently low endothelial shear stress." eng. In: *Arterioscler. Thromb. Vasc. Biol.* 33.7 (July 2013), pp. 1494–1504. ISSN: 1524-4636 (Electronic). DOI: 10.1161/ATVBAHA.112.300827.

[202] Yiannis S Chatzizisis et al. "Role of endothelial shear stress in the natural history of coronary atherosclerosis and vascular remodeling: molecular, cellular, and vascular behavior." eng. In: *J. Am. Coll. Cardiol.* 49.25 (June 2007), pp. 2379–2393. ISSN: 1558-3597 (Electronic). DOI: 10.1016/j.jacc.2007.02.059.

[203] Mahsa Dabagh et al. "Shear-induced force transmission in a multicomponent, multicell model of the endothelium." eng. In: *J. R. Soc. Interface* 11.98 (Sept. 2014), p. 20140431. ISSN: 1742-5662 (Electronic). DOI: 10.1098/rsif.2014.0431.

[204] K Naruse and M Sokabe. "Involvement of stretch-activated ion channels in Ca2+ mobilization to mechanical stretch in endothelial cells." eng. In: *Am. J. Physiol.* 264.4 Pt 1 (Apr. 1993), pp. C1037–44. ISSN: 0002-9513 (Print). DOI: 10.1152/ajpcell.1993.264.4.C1037.

[205] Sung Sik Hur et al. "Roles of cell confluency and fluid shear in 3-dimensional intracellular forces in endothelial cells". In: *Proc. Natl. Acad. Sci.* 109.28 (2012), pp. 11110–11115. ISSN: 0027-8424. DOI: 10.1073/pnas.1207326109. URL: https://www.pnas.org/content/109/28/11110.

[206] Cornelia Hahn and Martin A Schwartz. "Mechanotransduction in vascular physiology and atherogenesis." eng. In: *Nat. Rev. Mol. Cell Biol.* 10.1 (Jan. 2009), pp. 53–62. ISSN: 1471-0080 (Electronic). DOI: 10.1038/nrm2596.

[207] Michael A Jr Gimbrone and Guillermo García-Cardeña. "Endothelial Cell Dysfunction and the Pathobiology of Atherosclerosis." eng. In: *Circ. Res.* 118.4 (Feb. 2016), pp. 620–636. ISSN: 1524-4571 (Electronic). DOI: 10.1161/CIRCRESAHA.115.306301.

[208] Peter H Stone et al. "Prediction of progression of coronary artery disease and clinical outcomes using vascular profiling of endothelial shear stress and arterial plaque characteristics: The PREDICTION study". eng. In: *Circulation* 126.2 (July 2012), pp. 172–181. ISSN: 00097322. DOI: 10.1161/CIRCULATIONAHA.112.096438.

[209] Kevin Johnson, Puneet Sharma, and John Oshinski. "Coronary artery flow measurement using navigator echo gated phase contrast magnetic resonance velocity mapping at 3.0 T." eng. In: *J. Biomech.* 41.3 (2008), pp. 595–602. ISSN: 0021-9290 (Print). DOI: 10.1016/j.jbiomech.2007.10.010.

[210] M Markl et al. "Advanced flow MRI: emerging techniques and applications." eng. In: *Clin. Radiol.* 71.8 (Aug. 2016), pp. 779–795. ISSN: 1365-229X (Electronic). DOI: 10.1016/j.crad.2016.01.011.

[211] M Malvè et al. "Unsteady blood flow and mass transfer of a human left coronary artery bifurcation: FSI vs. CFD". In: *Int. Commun. Heat Mass Transf.* 39.6 (2012), pp. 745–751. ISSN: 0735-1933. DOI: https://doi.org/10.1016/j.icheatmasstransfer.2012.04.009.

[212] Dehong Zeng et al. "Effects of cardiac motion on right coronary artery hemodynamics." eng. In: *Ann. Biomed. Eng.* 31.4 (Apr. 2003), pp. 420–429. ISSN: 0090-6964 (Print). DOI: 10.1114/1.1560631.

[213] A Theodorakakos et al. "Simulation of cardiac motion on non-Newtonian, pulsating flow development in the human left anterior descending coronary artery". eng. In: *Phys. Med. Biol.* 53.18 (Sept. 2008), pp. 4875–4892. ISSN: 00319155. DOI: 10.1088/0031-9155/53/18/002.

[214] Leah C Winkel et al. "Animal models of surgically manipulated flow velocities to study shear stress-induced atherosclerosis." eng. In: *Atherosclerosis* 241.1 (July 2015), pp. 100–110. ISSN: 1879-1484 (Electronic). DOI: 10.1016/j.atherosclerosis.2015.04.796.

[215] Alina G van der Giessen et al. "3D fusion of intravascular ultrasound and coronary computed tomography for in-vivo wall shear stress analysis: a feasibility study." eng. In: *Int. J. Cardiovasc. Imaging* 26.7 (Oct. 2010), pp. 781–796. ISSN: 1875-8312 (Electronic). DOI: 10.1007/s10554-009-9546-y.

[216] Frank J H Gijsen et al. "Strain distribution over plaques in human coronary arteries relates to shear stress." eng. In: *Am. J. Physiol. Heart Circ. Physiol.* 295.4 (Oct. 2008), H1608–14. ISSN: 0363-6135 (Print). DOI: 10.1152/ajpheart.01081.2007.

[217] C J Slager et al. "The role of shear stress in the destabilization of vulnerable plaques and related therapeutic implications." eng. In: *Nat. Clin. Pract. Cardiovasc. Med.* 2.9 (Sept. 2005), pp. 456–464. ISSN: 1743-4297 (Print). DOI: 10.1038/ncpcardio0298.

[218] Annette M Kok et al. “The influence of multidirectional shear stress on plaque progression and composition changes in human coronary arteries.” eng. In: *EuroIntervention J. Eur. Collab. with Work. Gr. Interv. Cardiol. Eur. Soc. Cardiol.* 15.8 (Oct. 2019), pp. 692–699. ISSN: 1969-6213 (Electronic). DOI: 10.4244/EIJ-D-18-00529.

This Ph.D. thesis has been typeset by means of the TEX-system facilities. The typesetting engine was pdfLATEX. The document class was `toptesi`, by Claudio Beccari, with option `tipotesi=scudo`. This class is available in every up-to-date and complete TEX-system installation.